Analysis of Flapping Propulsion: Comparison, Characterization, and Optimization

Thesis by
Nathan Koon-Hung Martin

In Partial Fulfillment of the Requirements for the
Degree of
Doctor of Philosophy

CALIFORNIA INSTITUTE OF TECHNOLOGY
Pasadena, California

2018
Defended May 29th, 2018

Nathan Koon-Hung Martin
ORCID: 0000-0001-6038-6177

ACKNOWLEDGEMENTS

I would like to thank my advisor, Mory Gharib, for allowing me the freedom to work on projects that I was interested in, the flexibility to work at my own pace, and for providing valuable insights when I hit many roadblocks throughout my studies. My progress would not have been possible without his guidance and support.

I would like to thank my thesis committee members Professors Michael Dickinson, Anthony Leonard, and Beverley McKeon for their valuable insights and guidance which has helped greatly enhance the quality of my work.

I would like to thank all of the Caltech and GALCIT staff for helping me throughout my visit. Especially, Martha Salcedo, who helped me track down Mory and streamlined my research by taking care of all of the logistics; Christine Ramirez, who introduced me to Caltech and helped throughout with organizational issues; Joseph Haggerty and Ali Kiani in the GALCIT machine shop, who helped manufacture the necessary parts for my work in a timely manner and with great precision; John Van Deusen in the Caltech student machine shop, who taught me the basics of machining and enthusiastically helped me whenever I needed assistance machining parts; and Christine Ngo at the TechLab in SFL, who introduced me to 3D printing techniques which greatly streamlined prototyping parts for my research.

I would like to thank my group for supporting me throughout my time here. Especially, Chris Roh, Morgane Grivel, and Cong Wang for lifting my spirits, providing valuable insights through many discussions, and teaching me much of what I know now; I would like to thank my friends and family for providing emotional support throughout my studies and making my time at Caltech more enjoyable; and I would like to thank my experimental setups for surprisingly working as well as they did.

This work was supported by the Charyk Bio-inspired Laboratory at the California Institute of Technology. Nathan Martin was supported by the National Science Foundation Graduate Research Fellowship under Grant No. DGE-1144469. Chris Roh and Suhail Idrees, who helped me with the project involving the comparison between flapping and clapping propulsions, were supported by the National Science Foundation Graduate Research Fellowship under grant No. DGE-1144469 and the Caltech SURF program, respectively. Parts in chapter 3 were fabricated at the Caltech Library TechLab 3D Printing Facility, which was created and is sustained by funding from both the Caltech Moore-Hufstedler Fund and the Caltech Library.

ABSTRACT

In recent decades, the development of autonomous underwater vehicles (AUVs) has rapidly increased and inspiration for novel designs has recently come from nature, primarily based on the fast, efficient, and maneuverable flapping motion of fish. Due to its potential, flapping propulsion is investigated through three studies.

The first study involves the comparison between swimming by flapping and by periodic contractions. A direct comparison is made between the two propulsion mechanisms by simplifying the motions, utilizing a machine that can operate in either mode of propulsion, and evaluating the average thrust generated and the average input power required per cycle between the two mechanisms when the overall kinematics are identical. The two propulsion mechanisms are tested using a variety of overall kinematics, flexible plates, and modified duty cycles, all of which suggest that flapping propulsion is the more efficient; however, periodic contractions with a modified duty cycle are shown to generate more thrust per cycle.

The second study involves the characterization of the impact of chord-wise curvature on the hydrodynamic forces and torques, motivated by the dorso-ventral bending of a fish's caudal fin during locomotion. The impact of curvature is shown to depend on the planform area of the flapping plate. Plates with a smaller or an identical planform area compared with a baseline rigid flat rectangular plate either decrease or increase the generated thrust, respectively. These phenomena are utilized to develop an actuated plate for velocity modulation and a snap-buckling plate to provide a greater thrust and efficiency compared with a rigid plate propulsor.

The third study involves the development and demonstration of a method to experimentally optimize an arbitrary three-dimensional trajectory for a flapping propulsor. The trajectory is parameterized by variables inspired by birds and fish, executed by a mechanism that can actuate an arbitrary motion in a hemisphere, and optimized using an adaptive evolutionary strategy. The trajectories are scored based upon their difference from a desired force set-point and their efficiency. All trajectory searches demonstrate good convergence properties and match the desired force set-point almost immediately. Additional generations primarily improve the efficiency. This novel approach finds optimal trajectories for generating side-forces, similar to how a fish's pectoral fin or a bird's wing functions, and for generating thrust, similar to how a fish's caudal fin operates.

PUBLISHED CONTENT AND CONTRIBUTIONS

Martin, N. K. and Gharib, M. (2018). "On the role of tip curvature on flapping plates". In: *Bioinspiration and Biomimetics* 13. DOI: 10.1088/1748-3190/aaa1c0.
N.K.M. participated in the conception of the project, designed and manufactured the experimental setup, acquired and analyzed the data, and composed the manuscript.

Martin, N. K., Roh. C., Idrees, S., and Gharib, M. (2017). "To flap or not to flap: comparison between flapping and clapping propulsions". In: *Journal of Fluid Mechanics* 822. DOI: 10.1017/jfm.2017.252.
N.K.M. participated in the conception of the project, the design, and the construction of the experimental setup, acquired and analyzed the data, and composed the manuscript.

TABLE OF CONTENTS

LIST OF ILLUSTRATIONS

LIST OF TABLES

Chapter 1

INTRODUCTION

The growth and development of underwater vehicles has increased significantly in recent decades. Remotely operated vehicles (ROVs) [1] have predominantly replaced manned underwater vehicles [2] due to the increased safety, reduced deployment costs, and extended mission duration of ROVs. However, humans control these vehicles, which limits the duration of the mission due to operator fatigue. Control of these machines occurs through either a long tether, which has a maximum practical length, or through radio waves, which introduce a latency due to their travel time in water. The development of autonomous underwater vehicles (AUVs) aims to eliminate these drawbacks by removing the necessity of constant human operation and control. Current AUV designs [3] and control mechanisms [4] continue to push the limit of how fast, efficient, and maneuverable AUVs can be. Commercially available AUVs predominately use a propeller as their main method of propulsion, but propellers have a few drawbacks. First, propellers can typically only generate thrust in a single direction, which limits the maneuverability of the vehicle. (It should be noted that progress has been made on propellers where the pitch of each blade can be individually actuated during rotation to generate side-forces for turning [5–7].) Second, propellers generate a significant acoustic signature due to cavitation which corresponds to additional operating costs needed to repair damaged blades over time. Inspiration for novel designs to improve the efficiency and the maneuverability of autonomous underwater vehicles has recently come from nature [8] where there are many examples of animals that have a superior efficiency and maneuverability compared to existing vehicles. Studies comparing the efficiency of animals to that of propellers have shown that while propellers typically operate with 70% efficiency, animals are capable of operating above 80% efficiency. Furthermore, biomimetic fish can turn at a maximum rate of $75^\circ/\text{s}$ compared to standard rigid-bodied vehicles and submarines which can only turn at approximately $3 - 5^\circ/\text{s}$ [9]. Nevertheless, progress still must be made to achieve the potential efficiencies achieved by animals because a direct comparison between current off-the-shelf propellers and different bio-inspired designs has shown that existing propellers are more efficient [10].

The first step towards a better bio-inspired underwater vehicle lies in understanding how fish swim. Fish primarily propel themselves using either their body and/or

caudal fin (BCF locomotion) or their median and paired fins (MPF locomotion) [11]. BCF locomotion is typically considered to be the more efficient mechanism of propulsion, allowing for a larger maximum velocity at the cost of maneuverability, exhibited for example by fish that need to travel for long distances. MPF locomotion is typically considered to allow for improved maneuverability at the cost of a lower maximum velocity, exhibited for example by coral reef fish [12]. The category of BCF locomotion is divided into four modes of propulsion: anguilliform, subcarangiform, carangiform, and thunniform. These undulatory modes correspond to both the underlying propulsion mechanisms as well as the extent of the body involved in large amplitude lateral motion. The anguilliform, subarangiform, and carangiform modes use an added mass method of propulsion while the thunniform mode uses a vortex-based method of propulsion, known to be the most efficient of the four modes. Furthermore, in the order the modes were listed, the lateral motion decreases from involving the entirety of the body to primarily only the caudal fin. It should be noted that while BCF locomotion is not considered to be the most maneuverable, many fish employ a c-start motion to improve their maneuverability by first rapidly pitching their body and then their caudal fin for spontaneous acceleration and direction change [13].

BCF locomotion, involving an undulating or flapping motion used by fish, is commonly studied, due to its superior efficiency, by simplifying the motion. The flapping motion is often approximated as a plate pitching [14], heaving [15], or pitching and heaving simultaneously [16]. For pitching plates, work has been conducted to investigate the effect of the kinematics or the flexibility on the wake or the generated forces. Schnipper et al. [17] mapped the phase diagram of the vortex street behind a symmetric airfoil as a function of the stroke angle and the Strouhal number $St = fh/U_\infty$. Here, f is the frequency of oscillation, h is the maximum thickness of the airfoil, and U_∞ is the freestream velocity. Buchholz and Smits [18, 19] used dye visualization [20] to determine the wake behind a low aspect ratio pitching plate and measured the thrust and the efficiency as a function of Strouhal number. Kim and Gharib [21] used defocused digital particle image velocimetry (DDPIV) [22], a quantitative three-dimensional flow visualization technique, to examine the vortex structures formed behind pitching flat plates during their initial stroke. They found that the flow rolls up on the suction side of the plate forming a horseshoe-shaped vortex composed of two edge vortices connected by a tip vortex. This vortex structure remains attached and follows the trajectory of the plate with minimal outwards motion from the plate. Dai et al. [23] showed that flexible plates with a reduced

stiffness $K = EI/(\rho U_\infty^2 s^3 c)$ of 5 are the most efficient; reduced stiffness can be considered as a ratio of a material's resistance to bending over the bending moment applied by the fluid. Here, E is the elastic modulus of the plate, $I = ch^3/12$ is the second moment of area of the plate, c is the chord length of the plate, ρ is the density of the fluid, and s is the span of the plate. Yeh and Alexeev [24] showed that smaller aspect ratio plates can travel greater distances for less power. Lu et al. [25] studied large amplitude motions and found that increasing either the amplitude or the reduced frequency $k = 2\pi f c/U_\infty$ generates a greater thrust and requires more power but simultaneously increasing both the amplitude and the reduced frequency decreases the efficiency. A review of the theoretical work on flapping propulsion was conducted by Wu [26]. These works have highlighted the importance of stroke angle, frequency, and flexibility.

Underwater locomotion does not only occur through undulations, as there are many animals which use lift-based propulsion mechanisms such as sea turtles [27] and penguins [28]. These animals generate thrust, a force in the direction of forward motion, by creating a force in a plane parallel to that of the pitching motion. This in-plane force is approximately perpendicular to the path traversed by the fin. Lift-based propulsion is contrasted with undulations which generate thrust by creating a force orthogonal to the plane of the pitching motion. Generation of a force nearly perpendicular to the wing path also typically occurs in flying birds; therefore the design of a propulsor can benefit from an understanding of the complex aerodynamics of flight [29] and the wing trajectories typically used by birds. The wing trajectory of a bird can be implemented on an underwater vehicle by rotating the trajectory by 90° so that the traditional lift force a bird generates is aligned with the desired direction of motion. (It should be noted though, that the benefit of using lift-based propulsion underwater is that most underwater animals are neutrally buoyant. This means that while birds need to generate lift during flight to balance their body weight, lift generation is unnecessary for many underwater animals.) Wingtip trajectories are well documented for hummingbirds [30] and many other flying animals such as the albatross, pigeon, horseshoe bat, blowfly, locust, june beetle, and fruit fly [31]. These trajectories typically exhibit either a figure-eight or an elliptical shape with an overall camber and various rotation angles and wing flip timings. Studies of sinusoidal wing rotation velocity profile timings have shown that advanced rotation, where the wing's trailing edge starts to rotate towards the direction the wing is moving in, is the most efficient [32] and helps to stabilize the attached leading edge vortex, allowing for enhanced lift [33]. Non-sinusoidal wing

rotation velocity profiles, which allow for varying rotational accelerations, have been shown, in general, to increase the generated lift but reduce the overall efficiency [25]. These profiles take the form of $\alpha(t) = \theta \ \tanh[K_v \sin(2\pi f t)] \ / \ \tanh(K_v)$, where α is the angle of attack of the wing, θ is the amplitude of the rotation oscillation, t is the instantaneous time, and K_v is an adjustable parameter. These works have highlighted the prevalence of a figure-eight and an elliptical wing trajectory as well as the importance of the amplitude, phase, and acceleration of the the wing's rotation for lift generation.

Other forms of propulsion used by some swimming animals include drag-based propulsion, exhibited by turtles ands ducks, and jet-based propulsion, exhibited by jellyfish and squid. Drag-based propulsion, similar to lift based propulsion, generates thrust by creating a force in a plane parallel to that of the pitching motion; however, the fin creates an in-plane force along the path traversed by the fin instead of nearly perpendicular to the path traversed by the fin. This propulsion mechanism, typically composed of a 'power stoke' used to generate thrust and a 'recovery stroke' where little to no thrust is generated, sees its greatest efficiency at low speeds and is typically employed from rest [34]. Similar to drag-based propulsion, jet-propulsion only generates thrust for a portion of the cycle. During the opening motion, when the bell expands, two strong vortices are created at the tips, generating negative thrust, while during the closing motion, when the bell contracts, fluid is expelled creating a jet that generates positive thrust. The periodic contraction motion of a jellyfish is often simplified to that of clapping plates. For this motion, two plates, either attached at the leading edge or separated by a small gap, pitch symmetrically in opposite directions about the centerline which is similar to portions of the clap-and-fling mechanism [35, 36]. The closing motion is similar to the clap phase of the clap-and-fling mechanism in which the two wings have come together at an edge and pitch symmetrically towards the centerline, while the opening motion is similar to the beginning of the fling phase where the two wings pitch about an edge symmetrically away from the centerline. Early experimental work on the clap-and-fling mechanism was conducted by Spedding and Maxworthy [37], who obtained flow visualization and the aerodynamic forces during the fling phase, and by Ellington et al. [38], who obtained flow visualization of hawk moths using the clap-and-fling mechanism. Recent work on clapping plates found that low-aspect-ratio plates generate the strongest tip vortices, probably accounting for their greater thrust coefficients [39]. A review of the progress on the clap-and-fling mechanism was conducted by Sane [40].

Inspired by the propulsion mechanisms of fish and the lift generating mechanisms of birds, many bio-inspired AUVs [8] and micro air vehicles (MAVs) [41] have been developed using many different materials. A few examples in robotics utilize an assembly of strings and pulleys [42], macro fibre composites [43], ionic polymer-metal composites [44], or shape memory alloys [45] to mimic the antero-posterior bending of the fish's caudal fin during locomotion. A review of the commonly used actuation mechanisms was conducted by Karpelson et al. [46]. Generation of complex three-dimensional motions for MAVs typically use single or double cranks, single or double pulley systems, piezoelectric materials, or coil actuators [41]. Another mechanism that can be used to execute complex three-dimensional trajectories is a spherical parallel manipulator (SPM) [47, 48]. The advantage of this mechanism is that an arbitrary trajectory contained within a hemisphere can be executed with large torques because three actuators control the motion about a single fixed point. (This is in contrast to a serial manipulator where one actuator controls one degree of freedom.) There are many variations of this system defined by where the three joints are fixed, but the RRR system design, where the three joints are fixed to the same location, uniquely allows for infinite rotation [49, 50]. When using this mechanism, the complex three-dimensional wing trajectories of birds can be actuated and modified as desired.

Trajectory selection of a fin or a wing for either thrust or lift for AUV or MAV control can occur by either mimicking the trajectory of a selected animal, characterizing a simplified version of a trajectory inspired by animals, or searching for an optimal trajectory. There has been a considerable amount of work in regards to finding and studying optimal trajectories. Sane and Dickinson [51] systematically searched for an optimal trajectory that would maximize lift production starting from six variables. In general, four variables were fixed while two were varied. After mapping the parameter space of the two free variables, the optimal values were selected and then held fixed. This process was repeated to find all six optimal values. The result of the study found that a large stroke angle and a fast wing flip maximized lift production. Stroke deviation, in the form of a figure-eight or an elliptical trajectory, was investigated and shown to primarily decrease efficiency. Berman and Wang [52] computationally sought to optimize a trajectory that would most efficiently generate enough lift to support the body weight of an animal. The trajectory was parameterized with 11 variables and the optimum found by approximating the force and the power consumption using a quasi-steady model. The optimal trajectories were all figure-eight shaped and generated just enough

lift to support the body weight of the animal. Generating lift in excess of the body weight of the animal only decreased the efficiency. Thomson et al. [53] experimentally optimized a trajectory parameterized by 12 variables to maximize the generated lift. They used an optimization algorithm that incorporated the Box-Behnken sampling approach, ridge regression, and two gradient-based optimization formulations. Rakotomamonjy et al. [54] computationally optimized a trajectory to generate the maximum mean lift. The trajectory was parameterized by six variables and the forces were estimated using OSCAB, a flapping wing concept simulation tool that divided the wing into 2D slices. Neural networks were then used to reproduce the effects of the kinematics to estimate the forces and finally a genetic algorithm was used to find the optimum. Tuncer and Kaya [55] computationally optimized a 2D trajectory of pitching and plunging airfoils parameterized by three variables to generate thrust. The forces were estimated using a Reynolds-averaged Navier-Stokes equations solver. De Margerie et al. [56] computationally optimized a wing's size, shape, and motion parameterized by 12 variables to simultaneously minimize the average power consumed during a simulated flight and the distance deviated from a perfect horizontal flight trajectory. The flight trajectory of the vehicle was simulated using FMFAW (flight mechanics for flapping articulated wings) which uses a semi-empirical quasi-steady aerodynamics model that divides the wing into a number of rigid flat quadrangular wing elements. Optimization was conducted using epsilon-MOEA, a multi-objective algorithm which behaves similarly to a genetic algorithm. From the multitude of studies on the experimental or the computational optimization of trajectories for both lift and thrust, the set-points were typically a maximum force or a maximum efficiency where the force is allowed to vary. These studies highlighted different optimization schemes, although many additional options exist such as evolutionary algorithms [57]. Evolutionary strategy algorithms are real-valued and deterministic, evolutionary programming algorithms are real-valued and probablistic, and genetic algorithms are binary-valued and probablistic. Many of the base algorithms have been modified and refined over time such as the covariance matrix adaptive evolutionary strategy (CMA-ES) [58, 59] which has exhibited good convergence properties against common benchmarking functions [60, 61].

The flapping motion is used throughout nature and has inspired many novel vehicle designs; however, there is still much learn. Due to its potential as a viable propulsion mechanism and the richness of the subject, this thesis aims to further explore flapping propulsion to provide additional insights into its underlying mechanisms

and to reveal potential applications by taking advantage of newfound mechanisms. Flapping propulsion is explored through three studies. The first study in chapter 2 details the direct comparison of flapping propulsion to another common underwater propulsion mechanism. The second study in chapter 3 details the characterization of the impact of a novel geometry inspired from fish on the hydrodynamic forces and torques of a flapping propulsor. The third study in chapter 4 details the development and the demonstration of a method to experimentally optimize an arbitrary three-dimensional trajectory for a flapping propulsor. These studies provide additional insights into the underlying mechanisms of flapping propulsion and evidence for potential applications to either improve the maneuverability or the efficiency of AUVs.

Chapter 2

COMPARING FLAPPING AND CLAPPING PROPULSIONS

Martin, N. K., Roh. C., Idrees, S., and Gharib, M. (2017). "To flap or not to flap: comparison between flapping and clapping propulsions". In: *Journal of Fluid Mechanics* 822. DOI: 10.1017/jfm.2017.252.

2.1 Opening remarks

The purpose of this study is to investigate whether swimming by flapping or by periodic contractions is the more effective motion for underwater locomotion. Here, the most effective propulsion mechanism is that which generates the greatest thrust per cycle for the least power. For this comparison, the assumption is that a hypothetical animal desires the most effective mechanism and has two posterior fins at its disposal. The research question then becomes whether the animal should put both of its fins together and pitch them in the same direction (i.e. to utilize a flapping motion) or keep its fins apart and pitch them in opposite directions (i.e. to utilize a clapping motion). It should be noted that in this scenario, the bending rigidity, which is proportional to the thickness cubed, for flapping is only twice that used during periodic contractions instead of eight times larger as the plates are not fused together. For simplicity and for a straightforward comparison between the two mechanisms, propulsion by flapping is approximated as a plate pitching about its leading edge while propulsion by periodic contractions is approximated as clapping plates which fully open and close. The propulsion mechanisms are evaluated by constructing a machine that can operate in either mode of propulsion and comparing the thrust generated and the power required per cycle between trials of equivalent kinematics, namely total sweep angle ϕ and total sweep time t_s. For example, if the plates undergoing flapping sweep out 40° in 2 s, the two plates undergoing clapping would each sweep out 20° in 2 s. The plates are manufactured with a similar height to that of the test section (i.e. to have zero aspect ratio) for the greatest performance [24] and to generate approximately two-dimensional flow for a more direct comparison. Most tests are conducted without an imposed freestream to investigate the infinite-Strouhal-number limit and started from quiescent flow.

The machine operates between Reynolds numbers ($Re = Us/\nu$) of 1880 and 11 260, further discussed in section 2.2. Here, U is the average tip velocity of the plate, s is

the span of the plate, and ν is the kinematic viscosity of the fluid. An analogous *Re* for fish can be defined based on the average tip velocity and the length of the caudal fin while that for jellyfish can be defined based on the average tip velocity and the radius of the bell. Examples of fish that swim within this range are the *Leiostomus xanthurus* ($Re \sim 10\,500$), the *Brevoortia tyrannus* ($Re \sim 10\,500$), and the *Clupea harengus* ($Re \sim 3140$). This was determined by assuming that the typical caudal fin has a length that is 20% the standard length of a fish, a sweep angle of 60° [62], and an oscillation frequency between 2 and 15 Hz [63]. These values give a range of *Re* only as a function of the frequency and the standard length of a fish, many of which are documented by Sambilay Jr. [64]. (The specific *Re* for each fish is computed using the slower oscillation frequency for the *Brevoortia tyrannus* and the *Clupea harengus* and the higher oscillation frequency for the *Clupea harengus*.) Examples of jellyfish that swim within this range are the *Chrysaora lactea* ($Re \sim 3140$), the *Aurelia aurita* ($Re \sim 6280$), and the *Chrysaora colorata* ($Re \sim 11\,300$). This was determined by assuming that the typical bell has a total sweep angle of 20°, calculated by investigating the change in the angle between fully contracted and relaxed states using line segments connecting the apex to the bottom of the bell from images in Colin et al. [65], and a contraction frequency between 0.2 and 2 Hz [66]. Again, these values give a range of *Re* only as a function of the frequency and the bell radius of a jellyfish which are documented for the specific species [67–69]. (The specific *Re* for each jellyfish is computed assuming contraction rates of approximately 4, 2, and 0.4 Hz, respectively, and bell radii of approximately 5, 10, and 30 cm, respectively.)

2.2 Experimental setup and methods

The experiments are conducted using a single machine that can operate in either flapping or clapping mode for direct comparison (figure 2.1a). The design is based around two co-axial shafts, each with one attached plate; the inner shaft is directly connected to a stepper motor, while the outer shaft is allowed to rotate freely. In the clapping mode, a gearbox is enabled which drives the outer shaft in the opposite direction to the inner shaft, causing the two plates to pitch symmetrically about the centerline. In the flapping mode, the gearbox is disabled and the two plates are fixed to one another so that the outer shaft is driven with the same motion as the inner shaft. The span s and chord length c of all rectangular plates are kept constant at 0.127 m and 0.457 m respectively (figure 2.1b). The thickness h is 0.9525 mm for the baseline rigid aluminum plate and 1.016, 0.508, and 0.381 mm for the flexible polycarbonate

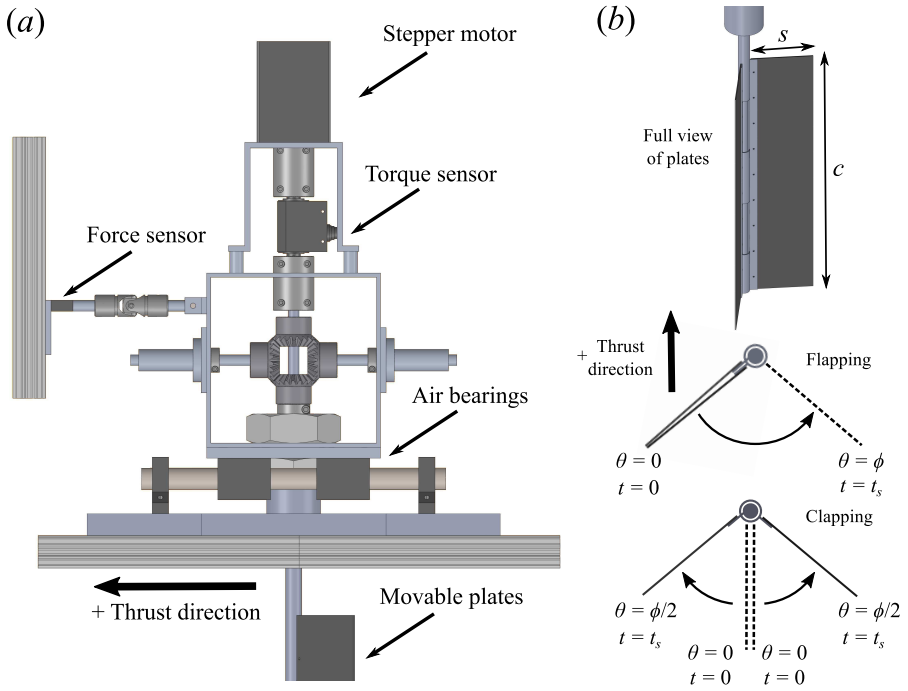

Figure 2.1: (a) Side-view of the machine. (b) Definition of chord c, span s, sweep angle ϕ and sweep time t_s. In the flapping configuration, where both plates are together, the dashed line denotes where the plates end after the first half of a cycle. In the clapping configuration, where both plates are separated, the dashed lines denote where the plates begin the first half of the cycle. In both configurations the arrows denote the direction of motion during the first half of the cycle but during the second half of the cycle, the motion is reversed.

plates; the dimensional flexural rigidities of the plates $D = Eh^3/(12(1-\nu_p^2))$, where E is the elastic modulus of the plate and ν_p is the Poisson's ratio for the plate, are 5.58, 0.247, 0.031, and 0.013 Pa m^3 respectively. Another measure of flexibility is the non-dimensional reduced stiffness $K = EI/(\rho U^2 s^3 c)$. This definition is similar to that used in Dai et al. [23], except that, here, U is the average speed of the trailing edge, defined as $(\phi/t_s)s$, and the second moment of area I is calculated as $ch^3/12$. The machine is driven with a sinusoidal velocity profile by an NEMA 34 single-shaft stepper motor with a 8.474 N m holding torque controlled by a GeckoDrive 213 V at 0.18 deg pulse^{-1}. The pulse train is generated using a National Instruments USB-6211 DAQ board. The machine is mounted on NewWay linear air bearings to isolate the force in the thrust direction (figure 2.1a). Forces are measured using a uni-axial Interface MB-5 Mini Beam Load Cell sampled at 4 kHz with a maximum capacity of 22.24 N, non-linearity of 6.672 mN, and hysteresis of 4.448 mN. The load cell is connected to the front of the mechanism via a universal joint to nullify the effects of

any generated moments. Torques are measured using a FUTEK rotary torque sensor sampled at 4 kHz with a maximum capacity of 20 N m, non-linearity of 0.04 N m, and hysteresis of 0.02 N m. The torque sensor is mounted between the stepper motor and the driven shaft. The plates are fully submerged in a free-surface water tunnel with a test section area that is 1.01 m wide and 1.83 m long with a maximum fill depth of 0.6 m. Free-surface effects are diminished by placing a Styrofoam sheet at the free surface near the top of the test plates.

By placing a Styrofoam sheet on the free surface and the bottom of the test plates close to the floor of the test section, three-dimensional effects are minimized. Three-dimensional effects are most prominent near the gap between the pitching plates and the test section wall; however, due to the small aspect ratio of the test plates, the region where three-dimensionality plays a role should be small compared to the total area of the plate. It is worth noting that three-dimensional effects are more prominent for the flexible clapping plates. This is evident because during the opening motion, the flexible clapping plates separate near the pitching axis, allowing flow in the chord-wise direction which is impossible if the flow is two-dimensional, instead of opening near the tips.

Digital particle image velocimetry (DPIV) [70] is used to investigate the flow field generated by the rigid baseline flapping and clapping plates. The flow is seeded with Potters Industries silver-coated hollow ceramic spheres (mean density 0.9 g cc^{-1} and diameter 100 µm), illuminated by an Opto Engine LLC 3 W continuous laser, creating a laser sheet along the mid-plane of the plates, and recorded using a Dantec Dynamics Nanosense MK-III at 100 frames per second. The vorticity field is computed from a phase average of three trials and used to estimate the generated thrust ($F = -F_v$) through

$$F_v = -\rho \frac{d\alpha}{dt} + \rho \sum_{j=1}^{N} \frac{d}{dt} \int_{R_j} v \, dR \tag{2.1}$$

for two-dimensional flow reproduced from Wu [71]; the flow is assumed to be two-dimensional due to the small aspect ratio of the plates. The first term is the change in the first moment of the vorticity field $\alpha \equiv \int_{R_\infty} r \times \Omega \, dR$, where R_∞ is an infinite domain, r is the distance from the origin, and Ω is the vorticity; this term simplifies to $\int_{R_\infty} y\omega_z \, dR$ as the only force of interest, the thrust, is in the x-direction. Calculation of α requires knowledge of all vortices ever created; therefore, analysis of the vorticity field is limited to the initial cycle when all vortices are within the field of view of the camera. It should be noted that $\frac{d\alpha}{dt}$ can be rewritten as

$\int_{R_\infty} \omega_z \frac{dy}{dt} + y\frac{d\omega_z}{dt}\, dR$ because the control volume does not change. The second term in (2.1) is the change of the velocity v inside the control volume R_j enclosing N solid bodies which is assumed to be negligible as the plates are thin. Vortex tracking provides insight into the contribution of each vortex to the overall force.

Direct comparison between the propulsion mechanisms is restricted to cases where both the total sweep time and the total sweep angle are identical. The total sweep times t_s of interest are 3, 2, and 1 s, while the total sweep angles ϕ of interest are 40°, 60°, and 80° (figure 2.1b). For the sweep time of 1 s, the only sweep angle tested is 40°, as greater accelerations are beyond the capability of the machine. These kinematics give a range of Reynolds numbers, based on the average tip velocity and span of the plate, $Re = Us/\nu$, between 1880 and 11 260. Here, U is the average tip velocity of the plate, s is the span of the plate, and ν is the kinematic viscosity of the fluid. Force and torque data are obtained for all combinations of sweep times and sweep angles where each combination has at least eight trials, each with at least 10 cycles. Average forces $\overline{F}$ and torques $\overline{T}$ per cycle for a single kinematic combination are obtained by averaging the mean force and mean torque per cycle over all trials; only cycles after the flow has reached steady state are used. The average thrust, torque, and power coefficients are calculated respectively as follows:

$$\overline{C}_T = \frac{\overline{F}}{\frac{1}{2}\rho U^2 A} \tag{2.2}$$

$$\overline{C}_\tau = \frac{\overline{T}}{\frac{1}{2}\rho U^2 A s} \tag{2.3}$$

$$\overline{C}_{po} = \frac{\overline{T}\,\overline{\omega}}{\frac{1}{2}\rho U^2 A s/t_s} \tag{2.4}$$

Here, $\overline{\omega} = \phi/t_s$ is the average angular velocity of the plate and $A = cs$ is the area of the plate. It should be noted that, for this choice of non-dimensionalization, $\overline{F}$ and $\overline{T}$ from flapping and clapping are divided by the same value if they share the same overall kinematics. The error bars are the standard deviations of the mean C_T and C_{po} recorded per cycle and although they are only plotted in one direction, they are symmetric.

The uncertainty of $\overline{F}$ and $\overline{T}$, due to the resolution of the force and torque transducers

are computed as follows:

$$\overline{F} = \frac{\sum_{i=1}^{N} F_i}{N} \tag{2.5a}$$

$$\Delta\overline{F}^2 = \sum_{i=1}^{N} \left(\frac{\partial \overline{F}}{\partial F_i}\right)^2 (\Delta F_i)^2 \tag{2.5b}$$

$$\Delta\overline{F} = \frac{\Delta F}{\sqrt{N}} \sim O(10^{-5}) \tag{2.5c}$$

$$\overline{T} = \frac{\sum_{i=1}^{N} T_i}{N} \tag{2.6a}$$

$$\Delta\overline{T} = \frac{\Delta T}{\sqrt{N}} \sim O(10^{-4}) \tag{2.6b}$$

Here, F_i and T_i are the instantaneous force and torque measurements during a cycle and N is the number of points averaged over a cycle. The maximum value for the resolution of the force transducer is 6.74 mN and the minimum value for the number of points averaged per cycle is 8000. The maximum value for the resolution of the torque transducer is 0.04 Nm and the minimum value for the number of points averaged per cycle is 8000. The uncertainty of $\overline{F}$ and $\overline{T}$ due to the resolution of the transducers are $O(10^{-5})$ N and $O(10^{-4})$ N m. This corresponds to an error in $\overline{C}_T$ and $\overline{C}_{po}$ of $O(10^{-3})$ and $O(10^{-1})$. These values are small compared to the standard deviation of the recorded forces and torques between trials in section 2.3 and are therefore not included in the error bars.

2.3 Results and discussion

The effect of kinematics

The effect of kinematics is investigated by varying ϕ and t_s on flapping and clapping rigid 0.9525 mm thick aluminum plates. The average thrust coefficient $\overline{C}_T$ and the average power coefficient $\overline{C}_{po}$ are shown in figures 2.2(a) and 2.2(b) respectively; the phase average of C_T and C_τ as a function of the non-dimensional time $t^* = t/2t_s$ during the initial cycle from three trials for $\phi = 60°$ and $t_s = 2$ s is shown in figure 2.3, illustrating the typical behavior and for comparison with DPIV results in a later section. The opening phase of clapping propulsion corresponds to the first half of the cycle while the closing phase corresponds to the second half of the cycle. The minimum reduced stiffness K of a single plate is 308.1 at a 40° sweep angle and a 1 s sweep time, meaning that the plates are effectively rigid with respect to the flow for all kinematic sets. Comparison of $\overline{C}_{po}$ between flapping

and clapping propulsions, denoted by the black and gray bars respectively, for all kinematic sets shows that clapping propulsion requires on average 3.87 times the power required for flapping propulsion. This can be understood conceptually by considering the volumetric flow rate through a plane bounded by and moving with the trailing edge of each clapping plate. Near the end of the closing phase, the area approaches zero so the velocity must approach infinity; however, during the beginning of the opening phase, the area starts from zero, so the velocity must start from negative infinity. The required flow reversal from positive to negative infinity requires a large pressure gradient which leads to an initially large torque and negative thrust seen during the first half of the cycle in the figure 2.3. Comparison of $\overline{C}_T$ between the mechanisms for each kinematic set shows that the difference in the average thrust per cycle is small compared with the difference in the average power per cycle. It should be noted that, despite their seemingly different methods of generating thrust, the average thrust generated per cycle is remarkably similar; flapping generates a predominately positive thrust during a cycle from a vortex street while clapping generates a positive thrust during its closing phase by creating a jet to push out fluid and a negative thrust during its opening phase by creating a low-pressure region to draw in fluid. Comparison between different kinematic sets shows that neither propulsion mechanism consistently generates more thrust. These results suggest that because the difference in $\overline{C}_T$ is small compared with the difference in $\overline{C}_{po}$ between the two mechanisms, and because flapping propulsion requires significantly less power than clapping propulsion, flapping propulsion is the more effective propulsion mechanism.

Flow field investigation with DPIV

Snapshots of the non-dimensional vorticity, $\omega_z^* = \omega_z/\overline{\omega}$, as a function of the non-dimensional position, $x^* = x/s$ and $y^* = y/L$, where $L = 2s\ sin(\phi/2)$ is the excursion length of the trailing edge, at different non-dimensional times t^* are shown in figure 2.4 for a 60° sweep angle and a 2 s sweep time; the corresponding force and torque data are shown in figure 2.3. The same behavior is exhibited for all other kinematic combinations. During each half of the cycle, the flapping plates generate a single vortex while the clapping plates generate two vortices, each which typically contains half of the circulation of a single vortex generated from flapping. Tracking of these vortices in time allows insight into their impact on the net thrust generated (figure 2.5) through (2.1). Here, the non-dimensional moment of vorticity, $\alpha^* = (\alpha\ t_s)/(1/2\ U^2 A)$, and the non-dimensional time derivative of α,

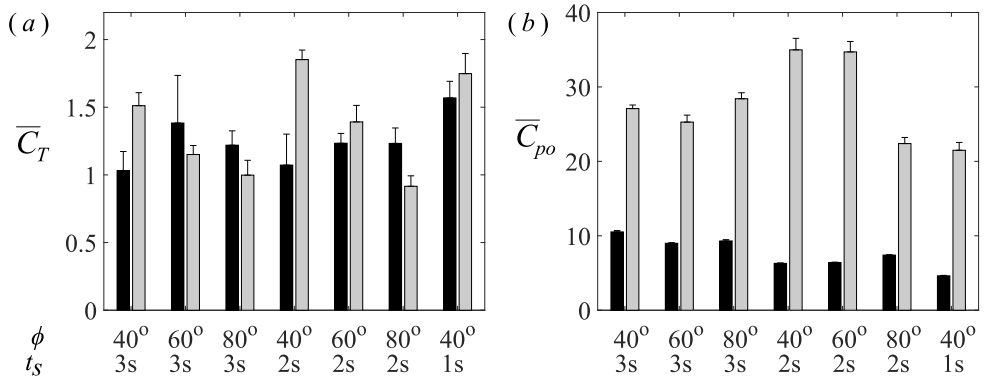

Figure 2.2: Average thrust coefficient $\overline{C}_T$ (a) and power coefficient $\overline{C}_{po}$ (b) for the baseline rigid aluminum plates as a function of plate kinematics. Sweep angle ϕ is given in degrees on the top row and sweep time t_s in seconds is given on the bottom row of the x-axis. Black bars denote the flapping configuration while gray bars denote the clapping configuration.

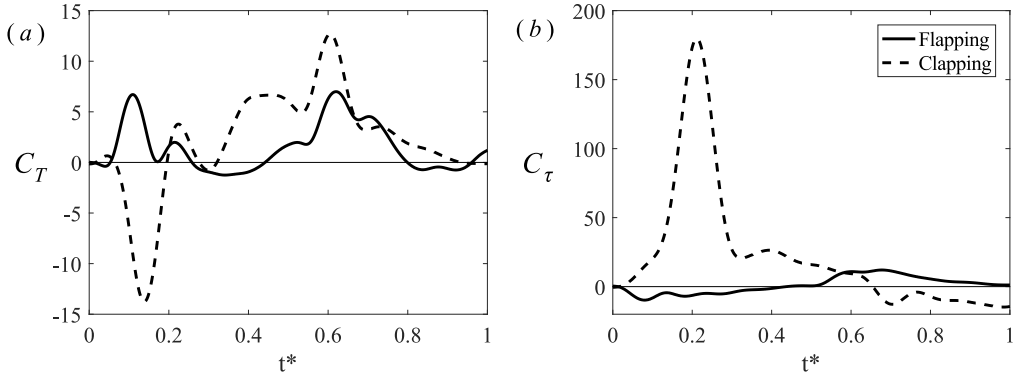

Figure 2.3: Phase averaged instantaneous C_T (a) and C_τ (b) from three trials with $\phi = 60°$ and $t_s = 2$ s. The solid black line corresponds to flapping while the dashed black line corresponds to clapping. The first half of the cycle corresponds to the opening phase of clapping while the second half of the cycle corresponds to the closing phase of clapping.

$\frac{d\alpha^*}{dt} = \frac{d\alpha}{dt}/(1/2\ U^2 A)$, which is used to estimate the thrust coefficient as $C_T = \frac{d\alpha^*}{dt}$, are shown as a function of t^*, allowing a straightforward comparison with the instantaneous thrust shown in figure 2.3. In figure 2.5, the solid black line denotes the sum of the contributions from all vortices, and the dotted black line, shown only for $\frac{d\alpha^*}{dt}$, denotes the mean value over the displayed time span. Data from $t^* = 0.875$ to 1 are not shown as the vortices become difficult to track. Vortices shed during the first half of the cycle are labeled '1' while vortices shed during the second half of the cycle are labeled '2'; if two vortices are shed during a cycle, the positive and negative vortices are labeled A and B respectively.

For flapping, during the first quarter of the cycle when the plates are accelerating, the circulation of vortex 1 increases, giving a positive contribution to the thrust. However, during the second quarter of the cycle when the plates are decelerating, the growth rate has stagnated and combined with the net drift downwards in y, noticeable by comparing the locations of vortex 1 at $t^* = 0.3$ and 0.75 in figure 2.4; vortex 1 gives a negative contribution to the thrust. This drift in y continues at later t^*, giving a negative contribution to the thrust during the second half of the cycle which nearly cancels the earlier positive contribution. For clapping, during the first quarter of the cycle when the plates are accelerating, the growth rates of vortices 1A and 1B increase, but here the vortices contribute negatively to the thrust because the growth rates of the vortices and their positions have opposite signs. This contribution is largely canceled by the positive impact on the thrust generated during the second quarter of the cycle as the vortices reduce in strength and drift towards the centerline. These results imply that the main contribution to the net thrust lies in the vortex moment from the vortices generated during the second half of the cycle which figure 2.5 shows to be nearly identical between the two propulsion modes. This provides an explanation for the similar thrusts seen in figure 2.2, as $\overline{C}_T$ predicted through vortex tracking using (2.1), $\overline{C}_T = \overline{\frac{d\alpha^*}{dt}}$, is 1.25 and 1.50 for flapping and clapping respectively, which is in reasonable agreement with the $\overline{C}_T$ of 1.44 and 2.01 for flapping and clapping respectively computed from figure 2.3. The discrepancy between the values is probably due to possible three-dimensionality of the flow as well as the difficulty in tracking the shed vortices as they begin to break up and diffuse; therefore, some vorticity may not be accounted for. Furthermore, (2.1) requires knowledge of the vorticity in the boundary layer of the plate, which is difficult to obtain through DPIV, and is the most significant during the starting motion. This likely accounts for the lower than expected peak in figure 2.4 during the starting motions. The similarity in the net thrusts is reasonable, as the magnitudes

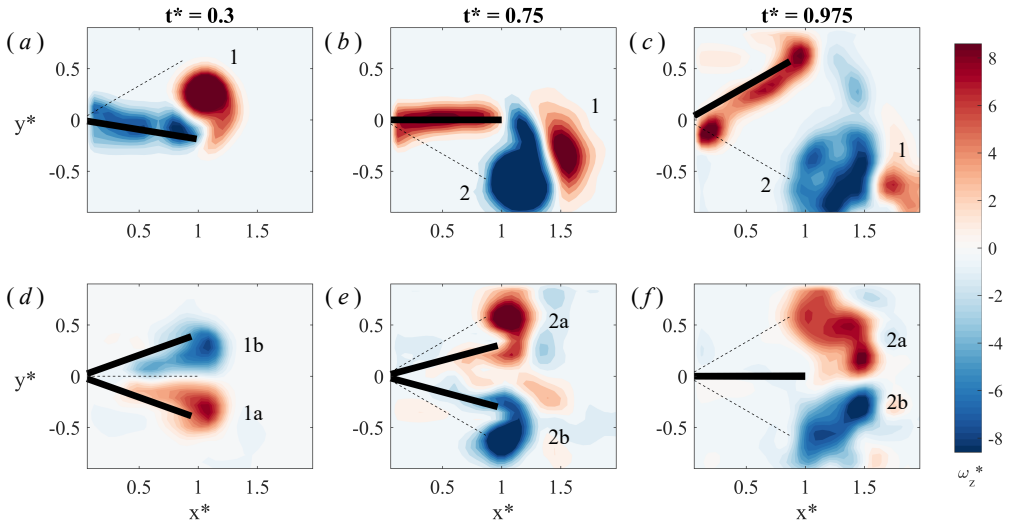

Figure 2.4: Non-dimensional vorticity contours $\omega_z^* = \omega_z/\overline{\omega}$ as a function of non-dimensional position $x^* = x/s$ and $y^* = y/L$ from PIV snapshots of flapping and clapping propulsions shown in (a,b,c) and (d,e,f) respectively for a 60° sweep angle and a 2 s sweep time. Each column corresponds to a snapshot taken at the same non-dimensional time $t^* = t/(2\ t_s)$. From $0 < t^* < 0.5$ the flapping plates sweep from top to bottom while the clapping plates open outwards. From $0.5 < t^* < 1$, the flapping plates sweep from bottom to top while the clapping plates close inwards. The thick black lines correspond to the location of the plates while the thin dashed lines correspond to the original location of the plates at the start of the half cycle.

and growth rates of the generated vortices are directly proportional to the velocity and acceleration of the plates, which are identical when comparing cases with the same overall ϕ and t_s. From the DPIV data, the circulation of a single vortex from flapping is typically twice that of a single vortex from clapping, meaning that the total circulation from the vortices are nearly identical. Furthermore, the excursions of the the plates are identical when comparing cases with identical kinematics, so the vortices will grow and shed at nearly identical positions, meaning that the total α from all vortices should be similar between the two propulsion mechanisms. The drift in y can be shown to be small as vortex 2 and vortices 2A and 2B tend to primarily translate in x, noticeable by examining their positions at $t^* = 0.75$ and 0.975 in figure 2.4. A similar behavior can be expected after many cycles.

The effect of flexibility

The effect of flexibility is investigated using polycarbonate plates of different thicknesses on a subset of the kinematic combinations. The 1.016 mm polycarbonate plates are tested with a variety of kinematic combinations and included for com-

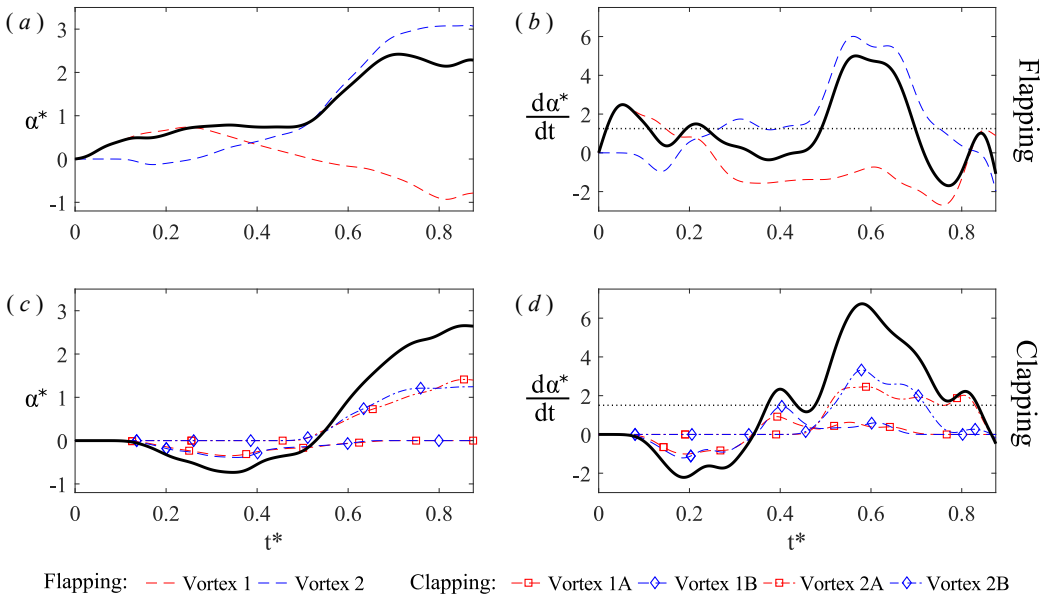

Figure 2.5: Vortex moment statistics for each vortex tracked in time from flapping (a,b) and clapping propulsions (c,d) for a 60° sweep angle and a 2 s sweep time. The non-dimensional first moment of vorticity α^* is shown in (a,c) and the non-dimensional time derivative of α, $\frac{d\alpha^*}{dt}$ used as a predictor for C_T, is shown in (b,d). Vortices shed during the first half of the cycle are labeled '1' while vortices shed during the second half of the cycle are labeled '2'; if two vortices are shed during a cycle, the positive and negative vortices are labeled A and B, respectively. The solid black line corresponds to the sum of the contribution from all vortices while the dashed black line, shown only for $\frac{d\alpha^*}{dt}$, corresponds to the mean value over the interval shown.

pleteness. The minimum K value for these plates is 12.72, meaning that the plates are reasonably rigid with respect to the flow for all kinematic sets. The $\overline{C}_T$ and $\overline{C}_{po}$ for the 1.016 mm plates are shown in figures 2.6(a) and 2.6(b) and provide further evidence that when using rigid plates with the same overall kinematics, $\overline{C}_T$ is similar between the two propulsion modes. The 0.508 mm and 0.381 mm polycarbonate plates are tested with 40°, 60°, and 80° sweep angles, each with a 2 s sweep time. The maximum K values for these plates are 6.549 and 2.763 respectively, meaning that large deformation occurs for all kinematic sets and three-dimensional effects are more prominent for the clapping motion. The $\overline{C}_T$ and $\overline{C}_{po}$ for the 0.508 mm plates are shown in figures 2.6(c) and 2.6(d), respectively, while those for the 0.381 mm plates are shown in figures 2.6(e) and 2.6(f), respectively. The $\overline{C}_T$ for the 0.508 mm plates is similar between the two propulsion modes despite the significant deformation throughout the cycle. (This suggests that three-dimensional effects did not

impact the overall comparison, considering the influence of three-dimensionality is significantly more prominent for clapping propulsion due to the induced chord-wise flow which occurs during the opening motion. A quantitative three-dimensional flow visualization technique is necessary to provide a definitive answer regarding the influence of the induced chord-wise flow.) The $\overline{C}_{po}$ for the 0.508 mm plates shows a reduction on average in the required input power for clapping propulsion compared with that for the rigid plates; however, the input power required is on average 4.5 greater than that for flapping propulsion. For the 0.381 mm plates, a difference between flapping and clapping becomes noticeable when comparing $\overline{C}_T$. Here, flexibility has led to a deficit in thrust for clapping propulsion, as $\overline{C}_T$ for clapping is on average 0.6 times that for flapping, probably because the plates begin to follow the flow instead of driving the flow. It should be noted that the bending rigidity for flapping propulsion is twice that of clapping propulsion, which is a likely explanation for why no significant deficit in thrust is seen in flapping propulsion. Although $\overline{C}_{po}$ for the 0.381 mm plates in clapping propulsion shows a 40% decrease on average compared with that from the 0.508 mm plates, $\overline{C}_{po}$ is on average 2.81 times that for flapping propulsion. (The reduced $\overline{C}_{po}$ for clapping propulsion is likely influenced by three-dimensional effects which allow the clapping plates to separate near the pitching axis during the opening motion. By separating the plates near the pitching axis, the required torque is reduced because the length of the moment arm is reduced.)

The results for the 0.508 mm flexible plates suggest that an increase in flexibility will not significantly affect $\overline{C}_T$ but will significantly decrease $\overline{C}_{po}$ for clapping propulsion; the increase in flexibility provides a marginal decrease in $\overline{C}_{po}$ for flapping propulsion. A natural assumption would be that a further increase in flexibility would decrease $\overline{C}_{po}$ for clapping propulsion to the point where $\overline{C}_{po}$ would be similar between the two mechanisms but leave $\overline{C}_T$ unchanged; if this were the case, the effectivenesses of the two propulsion mechanisms would be comparable. Although the results from the 0.381 mm plates continue the trend that increasing flexibility significantly decreases $\overline{C}_{po}$ for clapping propulsion, they also show that decreasing $\overline{C}_{po}$ can decrease $\overline{C}_T$ as well which impacts clapping more than flapping. Therefore, a further increase in flexibility will probably not make clapping propulsion more effective than flapping propulsion.

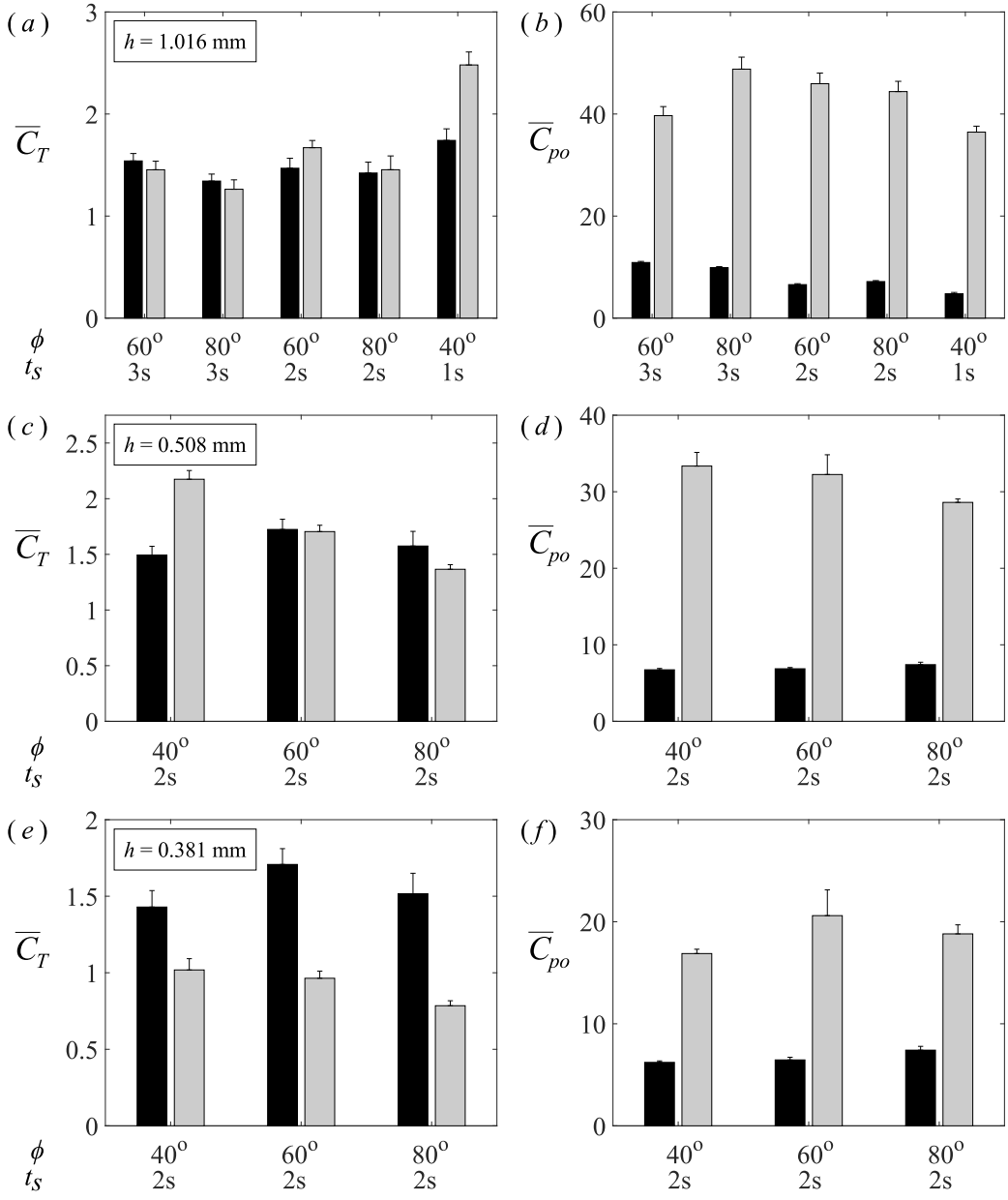

Figure 2.6: Average thrust coefficient $\overline{C}_T$ (a, c, e) and power coefficient $\overline{C}_{po}$ (b, d, f) for the flexible polycarbonate plates as a function of plate kinematics. Each row of graphs corresponds to the results for a different flexible plate; the graphs on the left contain the thickness h of the plates for that row in the upper left corner. Black bars denote the flapping configuration while gray bars denote the clapping configuration.

The effect of modifying the duty cycle

The effect of modifying the duty cycle is investigated on clapping propulsion only. In clapping propulsion, the opening phase generates a negative thrust and requires a large amount of power, while the closing phase generates a positive thrust but requires less power. By modifying the duty cycle to increase the time spent (i.e. decrease the angular velocity) in the opening phase and decrease the time spent (i.e. increase the angular velocity) in the closing phase, $\overline{C}_T$ should increase and $\overline{C}_{po}$ should decrease yielding an overall increase in effectiveness. It should be noted that modifying the duty cycle will change t_s during the opening and closing phases of a cycle but leave the total cycle time T_{cycle} unchanged. For consistency, the angular velocity in the coefficients $\overline{C}_T$ and $\overline{C}_{po}$ is defined as $\overline{\omega} = \phi/(T_{cycle}/2)$ to remain identical to that used in the previously discussed cases with the same overall kinematics. Modified duty cycles are investigated using 1.016 mm polycarbonate plates with 60° and 80° sweep angles and a 2 s sweep time. The minimum K for this plate is 12.72 at a 80° sweep angle and a 2 s sweep time, meaning that the plate is effectively rigid during all instances for the slower angular velocities. During the faster angular velocities, small deformation will occur typically at the beginning of the opening and closing phases of a cycle. Two modified duty cycles, where the opening phase took two and three times as long as the closing phase (2:1 and 3:1 duty cycles respectively), are compared with the results from an unmodified (1:1) duty cycle. The $\overline{C}_T$ and $\overline{C}_{po}$ for the 1.016 mm plates are shown in figures 2.7(a) and 2.7(b) respectively.

Modification of the duty cycle for the clapping 1.016 mm polycarbonate plates increases the $\overline{C}_T$ and decreases the $\overline{C}_{po}$ significantly. Compared with the $\overline{C}_T$ and $\overline{C}_{po}$ obtained from clapping with an unmodified duty cycle, use of a 3:1 duty cycle gives a 125% increase and a 45% decrease respectively. Compared with the $\overline{C}_T$ and $\overline{C}_{po}$ from flapping, the $\overline{C}_T$ and $\overline{C}_{po}$ from using a 3:1 duty cycle are on average 2.42 times and 3.58 times those for flapping respectively. A simple method of comparing the effectiveness between the two propulsion mechanisms is to use the force ratio, defined as $\eta \equiv \overline{F}/(\overline{T}/s)$, shown in figure 2.7(c). This result suggests that modification of the duty cycle for clapping propulsion causes the force ratio to approach that given by flapping propulsion. Additionally, this comparison is made with flapping propulsion without optimizing its motion; therefore, it is a reasonable assumption that the force ratio can be improved for flapping propulsion. This suggests that flapping propulsion is still the more effective mechanism, but clapping propulsion with a modified duty cycle can produce a greater thrust than

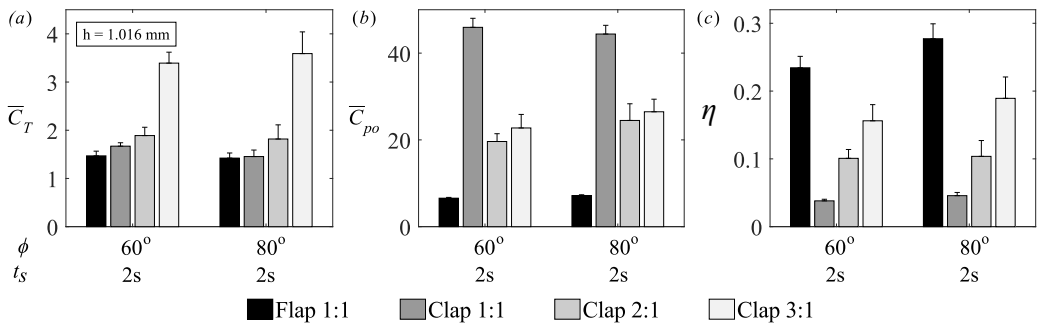

Figure 2.7: Average thrust coefficient $\overline{C}_T$ (a), power coefficient $\overline{C}_{po}$ (*b*), and force ratio η (c) for the 1.016 mm thick polycarbonate plate as a function of plate kinematics. Black bars denote the flapping configuration while the gray bars denote the clapping configuration with different duty cycles given as the ratio of the time spent in the opening phase to that spent in the closing phase.

flapping propulsion with an unmodified duty cycle.

For completeness, the $\overline{C}_T$ and $\overline{C}_{po}$ for the 0.508 mm plates with a modified duty cycle are included and shown in figures 2.8(a) and 2.8(b) respectively. Compared with the $\overline{C}_T$ obtained from clapping with an unmodified duty cycle, use of a 2:1 and 3:1 duty cycle gives a 45% increase and a 48% increase, respectively. The diminishing returns of moving from a 2:1 duty cycle to a 3:1 duty cycle are due to the high K value for these plates, causing the plates to be almost passive to the flow. This effect is apparent in the results for $\overline{C}_{po}$, which show a minimal decrease moving from a duty cycle of 1:1 to 2:1 and to 3:1. Because the plates deformed significantly when using a 1:1 duty cycle, increasing the angular velocity during the closing motion does not require much more power and decreasing the angular velocity during the opening motion does not save much more power. Comparing the best case scenario for clapping propulsion with the 3:1 duty cycle to flapping propulsion, the $\overline{C}_T$ of clapping is 1.76 times that for flapping but $\overline{C}_{po}$ is 2.32 times that for flapping. These results further illustrate the diminishing returns of using highly flexible plates and corroborate the conclusion that flapping propulsion is the more efficient mechanism. For these particular plates though, using clapping propulsion with a modified duty cycle only generates an increased thrust over flapping propulsion at the slower angular velocities when the fluid forces are not as large.

The effect of co-flow

Preliminary studies on the effect of co-flow are included for completeness, motivated by questions surrounding how the mechanisms would perform when the co-flow

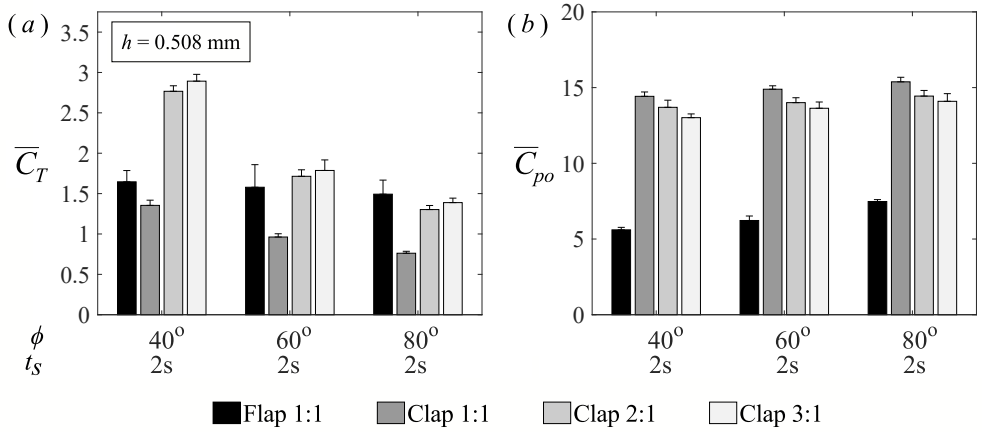

Figure 2.8: Average thrust coefficient $\overline{C}_T$ (a) and power coefficient $\overline{C}_{po}$ (b) for the 0.508 mm thick polycarbonate plate as a function of plate kinematics. Black bars denote the flapping configuration while the gray bars denote the clapping configuration with different duty cycles given as the ratio of the time spent in the opening phase to that spent in the closing phase.

velocity matches or exceeds the average velocity generated by the mechanisms. The two co-flow velocities tested are 0.122 m s^{-1} and 0.2035 m s^{-1} which are non-dimensionalized as $U^* = \overline{\omega} s / U_\infty$. The co-flow velocity that would match the average velocity generated is selected based on the DPIV results in a previous section to have $\overline{C}_T$ be as close to zero as possible. This is illustrated by the $\overline{C}_T$ of flapping and 1:1 clapping in figure 2.9(a). The co-flow velocity that would exceed the average velocity generated is selected arbitrarily. It should be noted that $\overline{C}_T$ and $\overline{C}_{po}$ are defined in the same manner as the previous sections for consistency, as opposed to using U_∞ as the characteristic velocity. The two sets of tests plates investigated are the 1.016 mm and the 0.381 mm thick polycarbonate plates. When considering the previously shown benefits of using a modified duty cycle with clapping propulsion, a 2:1 and a 3:1 duty cycle is also tested in the presence of the same co-flow velocities.

The $\overline{C}_T$ and the $\overline{C}_{po}$ for the plates in co-flow are shown in figures 2.9(a,c) and 2.9(b,d). It should be noted that in five of the six tested cases, the generated thrust is negative. This is reasonable for the cases in which the co-flow velocity exceeds the average velocity generated by the mechanism, because if the on-coming velocity is greater than the average velocity that the mechanism could generate, a negative thrust, or drag, would result. (This situation is analogous to a fish trying to swim upstream without the necessary strength to exceed the on-coming flow and getting swept downstream.) For these five cases, because the thrust is negative, the propulsion

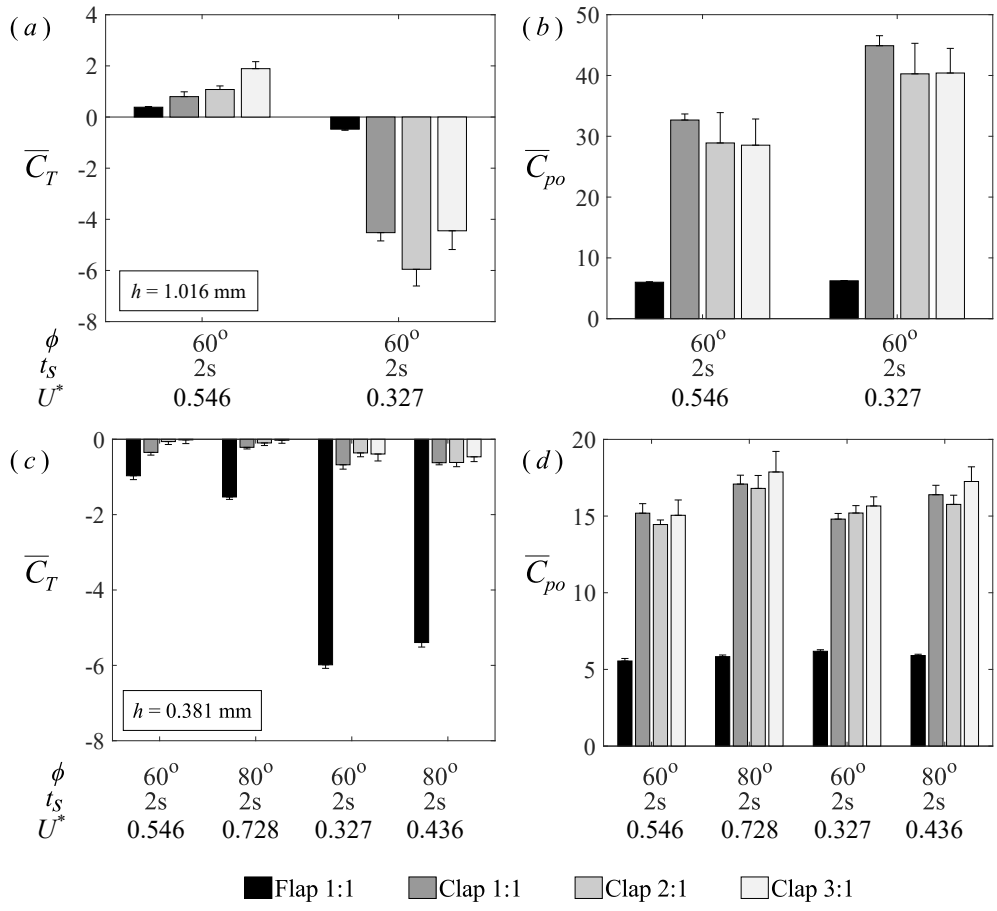

Figure 2.9: Average thrust coefficient $\overline{C}_T$ (a,c) and power coefficient $\overline{C}_{po}$ (b,d) for the 1.016 mm and 0.381 mm thick polycarbonate plates as a function of plate kinematics. Each row of graphs corresponds to the results for a different flexible plate; the graphs on the left contain the thickness h of the plates for that row in the upper left corner. Black bars denote the flapping configuration while the gray bars denote the clapping configuration with different duty cycles given as the ratio of the time spent in the opening phase to that spent in the closing phase.

mechanism that performs the best is simply that which minimizes drag. (It should be noted that for all of these circumstances, the best performance would actually be achieved by remaining aligned with the direction of the flow and not actuating. In this case, the only force would be skin friction, which would be significantly less than the pressure drag obtained by actuating, and the power required would be zero.) For the 1.016 mm plates, because they are rigid and because clapping propulsion uses two fins, the drag is significantly greater for clapping propulsion compared with flapping propulsion. This problem is compounded by moving from a 1:1 to a 2:1 duty cycle, during which the opening motion lasts longer, meaning the large planform area is exposed for longer. For the 0.381 mm plates, because of their flexibility and because clapping propulsion uses two fins, meaning the effective plate thickness is half that of flapping propulsion, the plates bend into a more streamlined shape which significantly reduces the resulting drag. The trends in $\overline{C}_{po}$ mimic those from the previously shown cases that flapping consistently requires less power.

The trends in $\overline{C}_T$ and $\overline{C}_{po}$ for the single case where a positive thrust is generated mimics those from the previously shown studies that moving from a 1:1 duty cycle to a 3:1 duty cycle increases $\overline{C}_T$ and decreases $\overline{C}_{po}$. It should be noted that the decrease in $\overline{C}_{po}$ is not as significant as that when co-flow is not present. This is probably because there are two competing factors. By opening slowly, the fluid does not have to be accelerated as much, which reduces the input power required, but a large planform area is presented for a longer duration compared with the 1:1 case, which increases the input power required. Interestingly, an efficiency comparison of flapping propulsion to clapping propulsion with a 3:1 duty cycle for this case reveals a small advantage in efficiency for clapping propulsion. $\overline{C}_T$ for clapping propulsion with a 3:1 duty cycle is 4.92 times that for flapping propulsion while $\overline{C}_{po}$ is only 4.72 times that for flapping propulsion. This shows promise that clapping propulsion with a modified duty cycle may have a superior efficiency to flapping propulsion in the presence of co-flow.

2.4 Closing remarks

A comparison has been made between flapping and clapping propulsions to determine which mechanism a hypothetical animal with two appendages should use. Overall, the results suggest that between *Re* of 1880 and 11 260, flapping is the more effective propulsion mechanism but a greater thrust can be generated using clapping propulsion with a modified duty cycle compared with flapping propulsion with an unmodified duty cycle. Between the two mechanisms, the difference in

the average thrust generated per cycle using the rigid aluminum plates was small compared with the difference in the average power required, for which flapping required significantly less power compared with clapping. Increase of the flexibility led to a decrease in the input power required, more so for clapping than for flapping, but did not decrease the power required enough for the effectiveness of clapping propulsion to be comparable to that from flapping propulsion. Modification of the duty cycle for rigid clapping plates led to a significant increase in the average thrust generated per cycle, which surpassed that produced during flapping propulsion, and to a significant decrease in the required power, causing the effectiveness of clapping propulsion to approach that of the unoptimized flapping propulsion. Therefore, the results suggest that if the hypothetical animal wants to use the most effective mechanism, the animal should put its two fins together and utilize a flapping motion.

Chapter 3

INVESTIGATING THE IMPACT OF CHORD-WISE CURVATURE ON FLAPPING PROPULSION

Martin, N. K. and Gharib, M. (2018). "On the role of tip curvature on flapping plates". In: *Bioinspiration and Biomimetics* 13.
DOI: 10.1088/1748-3190/aaa1c0.

3.1 Opening remarks

The antero-posterior bending of the fish's caudal fin during locomotion has been well studied and replicated in modern AUVs [8]. By contrast, the dorso-ventral bending of the caudal fin, documented by Bainbridge [72], remains largely unexplored to the best of the authors' knowledge. In his study, dorso-ventral bending (referred to as chord-wise bending herein), where the two tips of the caudal fin bend towards each other on a dace (*Leuciscus leuciscus*) was proposed to help smooth out the intermittent thrust generated by the tail and assist in braking; a concave caudal fin geometry was presented towards the incoming fluid when attempting a quick-stop maneuver. The maximum tip radius of curvature achieved by the dace was approximately 55 mm with a tip curvature aspect ratio $\beta = h/c'$ of approximately 0.22; here, h and c' are the height and width of the curved geometry (figure 3.1(c)). Studies of bluegill sunfish (*Lepomis macrochirus*) [73], which predominately maneuver using their pectoral fins, documented a cupping motion of the pectoral fins when swimming, creating a bent geometry similar to the dorso-ventral bending of the dace's caudal fin. This motion was recreated using actuated fin rays, which behave similarly to a bimetallic strip, and was shown to significantly reduce drag [74].

The purpose of this study is to investigate the effects of chord-wise tip curvature on the forces and torques generated by flapping plates as a simplified model of the dorso-ventral bending of a fish's caudal fin during locomotion. Here, the flapping motion of a fish's caudal fin during locomotion is approximated by the pitching motion of plates. This motion is used to emulate thunniform swimming where the caudal fin is the primary source of thrust and lateral motion [11]. The plates are compared at different stroke angles ϕ and stroke times t_s (figure 3.1(b)) to assess their performance using the experimental setup described in section 3.2. First, the concept

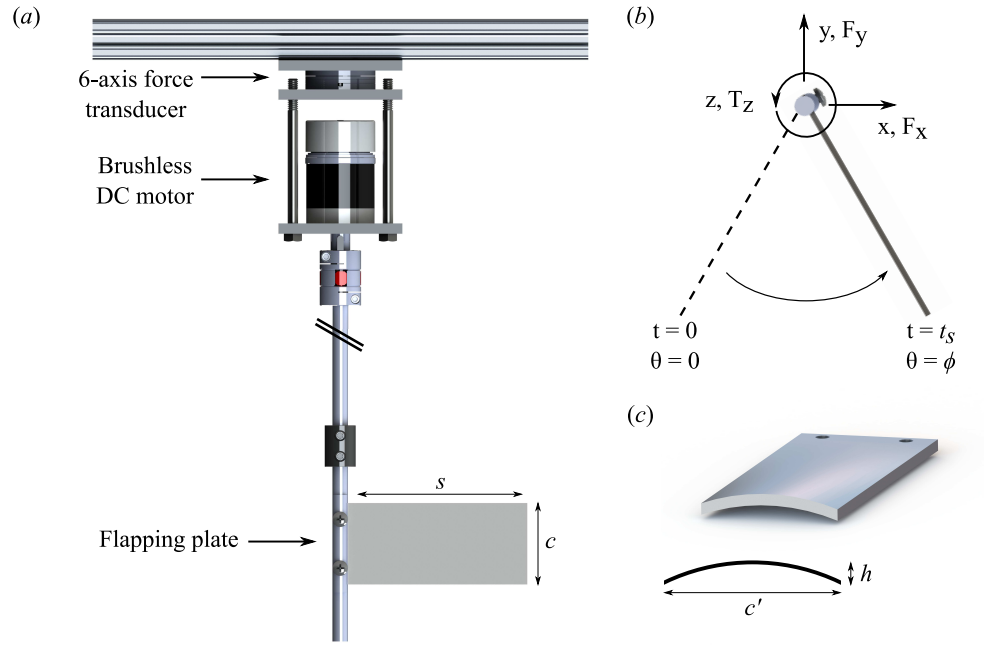

Figure 3.1: (a) Side view of the experimental setup and the definition of the span s and the chord c. (b) Definition of the stroke angle ϕ, the stroke time t_s, and the positive direction of the x, y, and z axes, the forces F_x and F_y, and the torque T_z. The dashed line denotes the original position of the plate at the beginning of the first half of the cycle. The curved arrow denotes the direction of motion during the first half of the cycle; during the second half of the cycle, the motion is reversed. (c) Definition of the height h and the width c' measured at the tip of the test plates.

of emulating active chord-wise bending, similar to the dorso-ventral bending seen in the caudal fin, is explored. A baseline is established by comparing a rigid flat plate with rigid curved plates. This is followed by the implementation of a dynamically-actuated design. Second, the impact of curvature is isolated using plates with the same planform area. This is in contrast to the previous cases which emulate physically curving the plates which reduces the plate's planform area. Similar to the previous case, a baseline is established using rigid curved plates, followed by a brief discussion on the impact of the planform area and the implementation of a passively-actuated plate. Finally, the generated wake behind select test plates are investigated to explain their performance. All tests begin from quiescent flow and continue without an imposed co-flow to investigate the infinite-Strouhal-number limit.

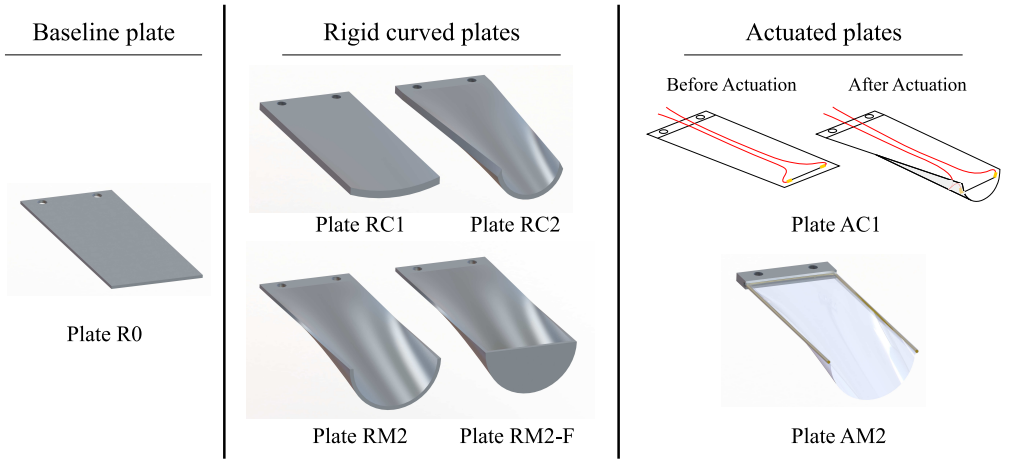

Figure 3.2: Render of the test plates used. 'R' denotes a rigid static plate, 'A' denotes an actuated plate, 'C' denotes a plate emulating physically curving the two free corners towards each other reducing the planform area, 'M' denotes a plate with a matched planform area to that of the baseline flat plate, and '-F' indicates that a fence is added to the tip of the plate . The numbers '0', '1', and '2' qualitatively distinguish between no, small, and large tip curvatures.

3.2 Experimental setup

The setup shown in figure 3.1(a) pitches the test plates, shown with their acronyms, in figure 3.2. The first letter of 'R' or 'A' denotes a rigid (R) static plate or an actuated (A) plate, respectively. The second letter of 'C' corresponds to plates which emulate physically curving (C) the two free corners of a plate towards each other and therefore have a reduced planform area. The second letter of 'M' corresponds to plates used to isolate the impact of tip curvature and therefore have the same chord, the same span, and a matched (M) planform area, 5470 mm^2, as those of the baseline rigid flat plate. The numbers '0', '1', and '2' are used to qualitatively distinguish between no, small, and large tip curvature. The addition of '-F' to the acronym indicates that a fence (F) is added to the tip of the plate.

A full cycle consists of two strokes. The forward and the backward strokes are defined as the first and the second stroke in a cycle, respectively. It should be noted that the rigid curved plates present a concave geometry towards the incoming flow during the forward stroke and a convex geometry towards the incoming flow during the backward stroke. All of the test plates are compared with the baseline aluminum rigid flat plate R0 with a span $s = 110.5$ mm, a chord length $c = 50$ mm, a thickness $t = 1.65$ mm, a planform area $A = 5520\,mm^2$, and an aspect ratio $s/c = 2.21$; all

other plates have the same span and chord unless specified otherwise.

Plates RC1 and RC2 are rapidly-prototyped 4 mm thick plastic plates with a tip chord-wise radius of curvature of 72.0 mm and 15.9 mm, tip curvature aspect ratio $\beta = h/c'$ of 0.0878 and 0.5 (figure 3.1(c)), and a planform area of 5410 mm^2 and 4700 mm^2, respectively. The chords of plates RC1 and RC2 decrease linearly from 50 mm at the root to 49 mm and 31.8 mm, respectively, at the tip of the plate. Plate AC1 is a dynamically-actuated plate with a controllable tip curvature realized by attaching a 35 mm long 0.254 mm diameter Dynalloy, Inc. Flexinol actuator wire made of Nitinol, a shape memory alloy that contracts when heated to 70 °C by an electric current, to the tip of a 0.381 mm and a 0.508 mm thick polycarbonate plate. Stronger material or thicker polycarbonate plates exceed the actuation capability of the Nitinol wire. These plates have a reduced stiffness $K = EI/\rho U^2 s^3 c$ of 1.094 and 1.459, respectively. The 0.381 mm thick plate is tested at $\phi = 90°$ in $t_s = 2$ s while the 0.508 mm thick plate is tested at $\phi = 60°$ in $t_s = 1$ s (figure 3.1(b)). For $K = O(1)$, the bending moment applied by the fluid is comparable to the material's resistance to bending, meaning that the plate significantly deforms throughout the cycle. This definition of K is similar to that used by Dai et al. [23], except here, $U = s\phi/t_s$ is the average speed of the trailing edge. The Nitinol wire, selected due to its large deflection and actuation force compared with other mechanisms [46], has a maximum strain rate and pulling force of 4.5% and 8.74 N, respectively. Actuation occurs through a BOP 50-4M controllable power supply, with a voltage range of ±50 V and a current range of ±4 A, using signals from a National Instruments USB-6211 DAQ. When actuated in 20 °C water using a 0-4 A square wave, the tip obtains a maximum radius of curvature of 43 mm and a $\beta = 0.13$ in 0.05 s. The relaxation time of the wire is approximately 0.5 s; however, during the pitching motion, the relaxation time decreases due to convection cooling.

Plates RM2 and RM2-F are rapidly-prototyped, 2 mm thick plastic plates with a tip chord-wise radius of curvature of 23 mm and a $\beta = 0.5$. The plates are identical except that plate RM2-F has a 2 mm thick fence attached to the tip. Plate AM2 is a passively-actuated plate that snap-buckles into an inextensible curved geometry similar to that of plate RM2 following a change in direction. This is accomplished by attaching a 0.02 mm thick polycarbonate sheet, with a pre-curved 23 mm tip radius of curvature to a 1.59 mm diameter brass wire frame. (A trial-and-error process is used to select a thickness for the polycarbonate sheet that would snap-buckle immediately following a change in direction for various kinematics.) The radius

of curvature is identical to that of plates RM2 and RM2-F. It should be noted that plate AM2 presents a concave geometry into the flow during both the forward and the backward strokes and that polycarbonate is effectively inextensible under the tested flow conditions, meaning the material does not stretch during the motion. A summary of the test plates and their acronyms is shown table 3.1.

Plate	Type	$A(\text{mm}^2)$	β(-)	Note
R0	Rigid	5520	0	-
RC1	Rigid	5410	0.0878	-
RC2	Rigid	4700	0.5	-
RM2	Rigid	5470	0.5	-
RM2-F	Rigid	5470	0.5	Fence
AC1	Actuated	5520	0.13	Nitinol
AM2	Actuated	5520	0.5	Snap-buckle

Table 3.1: Abbreviations and characteristics of the plates.

The plates are pitched by a Maxon EC 45 flat DC brushless motor, to which a 4.3:1 reduction gearhead and a 2048 counts per turn encoder are attached. The motor is controlled using an EPOS2 24/5 digital position controller and driven with a sinusoidal velocity profile generated from a National Instruments USB-6211 DAQ board. The stroke angles ϕ studied are 45°, 60°, 75°, and 90°, while the stroke times t_s studied are 2, 1, 0.75, and 0.5 s for a single stroke (figure 3.1(b)). These kinematics give a range of Reynolds numbers $Re = Us/\nu$, used to characterize the flow conditions from a ratio of inertial to viscous forces, between 7920 and 19 000 based on the average tip velocity of the plate $U = \overline{\omega}s$, the average angular velocity of the plate $\overline{\omega} = \phi/t_s$, the span of the plate s, and the kinematic viscosity of the fluid ν. It should be noted that the rigid plates do not exhibit any significant deformation during any of the trials. The performance of the plates is evaluated by investigating the instantaneous and the average forces and torques generated per cycle after reaching steady state; the average values per cycle are typically calculated from five trials, with at least eight cycles per trial. The forces and torques used to assess the performance of each plate are measured using an ATI Nano 43 sampled at 4 kHz, a 6-axis force and torque transducer, with a maximum capacity of 18 N and 250 N mm and a resolution of 0.0039 N and 0.050 N mm. The average side-force,

thrust, and torque coefficients are written as:

$$\overline{C}_S = \frac{\overline{|F_x|}}{\frac{1}{2}\rho U^2 A} \tag{3.1a}$$

$$\overline{C}_T = \frac{\overline{F}_y}{\frac{1}{2}\rho U^2 A} \tag{3.1b}$$

$$\overline{C}_\tau = \frac{\overline{|T_z|}}{\frac{1}{2}\rho U^2 A s} \tag{3.1c}$$

The instantaneous versions of these coefficients are identical but do not use averaged quantities denoted by an overline. The signs and directions of the forces and torques are consistent with the coordinate system illustrated in figure 3.1(b). The efficiency is defined in two ways:

$$\eta_1 = \frac{\overline{F}_y}{\overline{|F_x|}} \tag{3.2a}$$

$$\eta_2 = \frac{\overline{F}_y}{\overline{|T_z/s|}} \tag{3.2b}$$

Here, η_1 compares the thrust to the side-force, typically used in biology, while η_2 compares the thrust generated to the required torque, similar to a mechanical efficiency. It should be noted that T_z can be interpreted as an alternative description for side-force, as T_z is related to the force normal to the plate at all times throughout the motion. The error bars shown for $\overline{C}_S$, $\overline{C}_T$, η_1, and η_2 in section 3.3 are computed from the standard deviation of the mean C_S, C_T, and C_τ per cycle and although they are only plotted in one direction, they are symmetric. The minimum value for the number of points averaged per cycle is 8000. The uncertainty of $\overline{|F_x|}$, $\overline{F_y}$, and $\overline{|T_z|}$, computed from (2.5c) and (2.6b), due to the resolution of the transducers are $O(10^{-5})$ N, $O(10^{-5})$ N, and $O(10^{-7})$ N m. This corresponds to an error in $\overline{C}_S$, $\overline{C}_T$, and $\overline{C}_\tau$ of $O(10^{-3})$, $O(10^{-3})$, and $O(10^{-4})$. These values are small compared to the standard deviation of the recorded forces and torques between trials in section 3.3 and are therefore not included in the error bars.

All experiments are conducted in a 0.762 m long, 0.305 m wide, and 0.483 m tall water tank starting from quiescent flow. As the tank is small compared with the size of the plates, only 10 cycles are recorded to minimize re-circulation effects. To minimize free surface effects, the plates are fully submerged.

The generated flow field is investigated qualitatively through dye visualization [20] during the first forward stroke and quantitatively through digital particle image

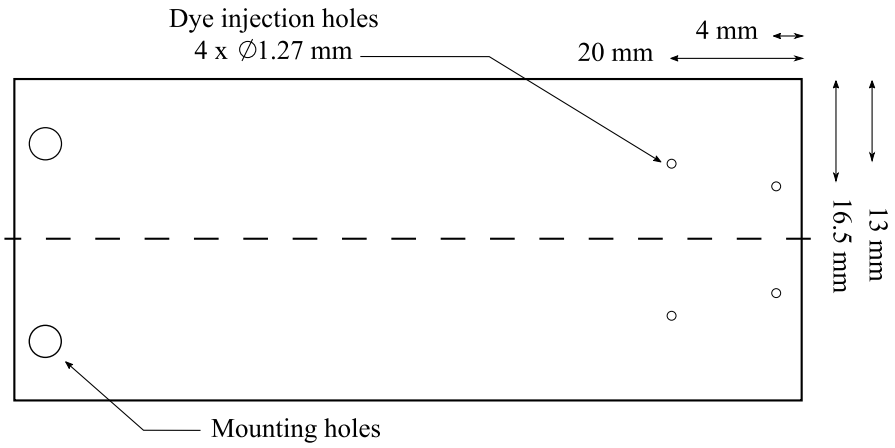

Figure 3.3: Location of the dye injection points relative to a corner of the tip. The dye injection points are identical for all of the dye injection plates. All dye injection holes have the same diameter. The mid-plane, or line of symmetry, for the plate is indicated by the dashed line.

velocimetry (DPIV) [70] once the flow has reached steady state. Dye visualization is conducted by injecting red food coloring at 500 µL/min from two Harvard Apparatus dual syringe pumps through four separate internal chambers in rapidly prototyped 3.81 mm thick PLA plastic versions of the test plates. The locations of the dye injection points are dimensioned in figure 3.3. These locations were selected through a trial-and-error processes to best visualize the flow and are identical for all of the dye injection test plates. Images of the generated flow field were captured in color using a Canon Vixia HF R700 camcorder at 60 frames per second angled normal to the initial position of the plate to provide a better view of the developing vortex structures. DPIV is realized by first seeding the flow with Potters Industries silver-coated hollow glass spheres (mean density 1.60 g cc^{-1} and diameter 13 µm). Then, illuminating the near wake using an Opto Engine LLC 3W continuous laser to create a laser sheet along the mid-plane of the pitching plates; the mid-plane is the same as the line of symmetry denoted by the dashed line in figure 3.3. Finally, recording the position of the illuminated particles, which follow the flow, with an IDT Motion Pro Y7 at 500 frames per second. By recording the position of the particles in time at a known frame rate, quantitative information about the flow field can be obtained.

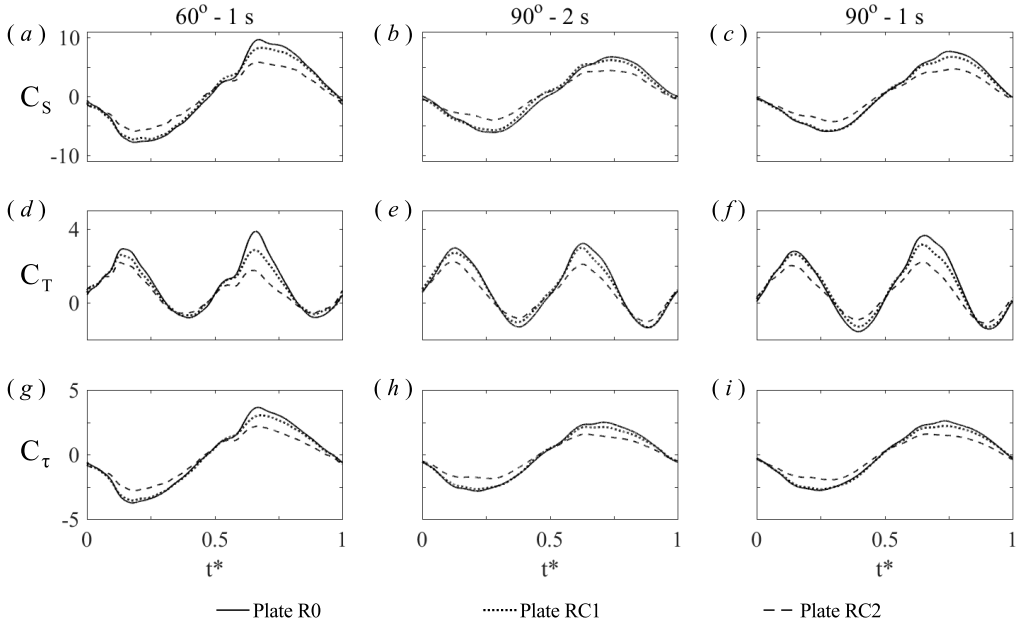

Figure 3.4: Typical instantaneous C_S (a-c), C_T (d-f), and C_τ (g-i) as functions of t^* over one full cycle after reaching steady state for plates R0, RC1, and RC2. Panels (a,d,g), (b,e,h), and (c,f,i) have the same kinematics given in the form $\phi - t_s$. The first half of all of the plots, $0 < t^* < 0.5$, corresponds to the forward stroke, when the rigid curved plates are concave to the incoming flow, while the second half of all of the plots, $0.5 < t^* < 1$, corresponds to the backward stroke, when the rigid curved plates are convex to the flow.

3.3 Results and discussion

Rigid curved plates as a baseline

The two rigid curved plates with a small and a large tip radius of curvature, plates RC1 and RC2, respectively, are compared with a rigid flat plate, plate R0. This comparison is made to establish a baseline regarding the effect of curvature on the generated forces and torques if a rigid flat plate could be actuated into a similar curved geometry. The curvature of plate RC1 is selected to be similar to the maximum achievable curvature through dynamic actuation with plate AC1, while the curvature of plate RC2 is selected as a semicircle to investigate the impact of curvatures larger than plate AC1 can realize. The instantaneous C_S, C_T, and C_τ as functions of the non-dimensional time $t^* = t/(2t_s)$ are shown in figure 3.4 for a typical cycle and the $\overline{C}_S$, $\overline{C}_T$, η_1, and η_2 per cycle are shown in figure 3.5 for plates R0, RC1, and RC2. The forward stroke, when a concave geometry is presented by the rigid curved plates towards the incoming flow, corresponds to $0 < t^* < 0.5$ while the backward stroke, when a convex geometry is presented towards the incoming

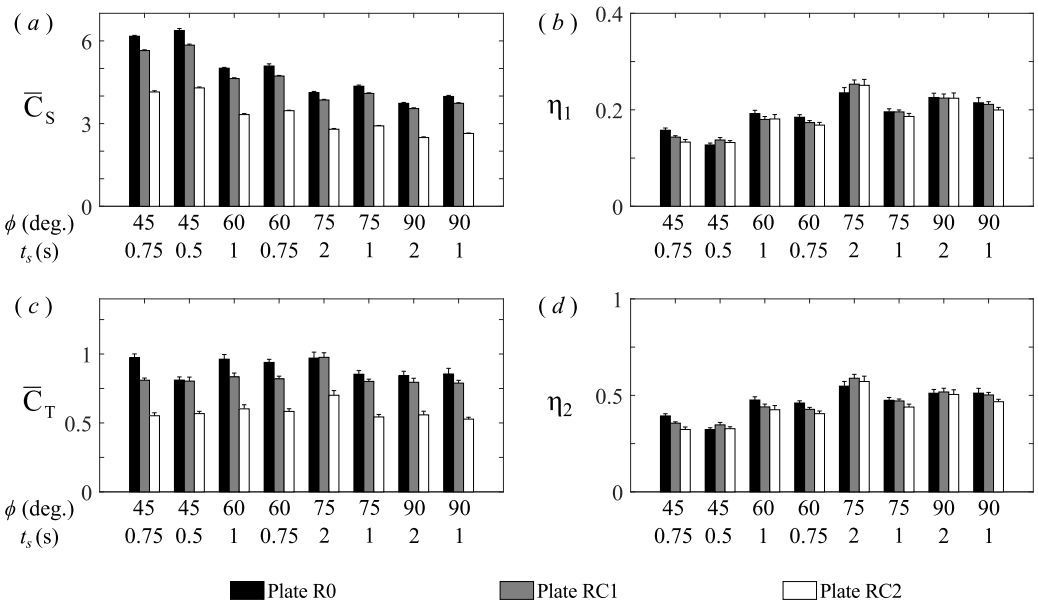

Figure 3.5: Average side-force coefficient $\overline{C}_S$ (a), average thrust coefficient $\overline{C}_T$ (c), and two definitions of efficiency, η_1 (b) and η_2 (d), over a cycle as functions of the plate kinematics for plates R0, RC1, and RC2. The x-axis indicates the stroke angle ϕ on the top row and the stroke time t_s on the bottom row.

flow, corresponds to $0.5 < t^* < 1$.

Comparison of the instantaneous C_S in figures 3.4(a-c) between the three plates for all sets of kinematics shows that increasing the curvature decreases the peak side-force generated, even when accounting for the difference in the planform area with the denominator of C_S. From the data shown in figure 3.4, plates RC1 and RC2 decrease the peak side-force by 5.3% and 30.8% on average during the forward stroke, respectively, and by 10.8% and 38.3% on average during the backward stroke, respectively, when compared with plate R0. The results from the instantaneous C_τ in figures 3.4(g-i) corroborate the results from C_S. Comparison of the instantaneous C_T in figures 3.4(d-f) between the three plates for all sets of kinematics shows a decrease in the peak thrust generated by plates RC1 and RC2 compared with R0. The data shown in figure 3.4 indicates that plates RC1 and RC2 decrease the peak thrust by 9.8% and 25.9% on average during the forward stroke, respectively, and by 15.2% and 43.3% on average during the backward stroke, respectively, when compared with plate R0. These results can be attributed to the reduced planform area of plates RC1 and RC2 creating a more streamlined geometry further discussed in a later section. A more streamlined body opposes the flow less, decreasing the side-force, and pushes less fluid in the thrust direction, decreasing the generated thrust.

Regarding the difference between the forward and the backward strokes, the greater decrease in side-force is due to the lower drag coefficient of a convex geometry compared with a concave geometry [75], while the greater decrease in thrust is due to a convex geometry creating a significant amount of suction, highlighted by the DPIV results in a later section.

Comparison of $\overline{C}_S$ and $\overline{C}_T$ between the three plates in figures 3.5(a,c), respectively, corroborates the previous conclusion from the instantaneous C_S and C_T that an increased curvature decreases all of the generated forces. It should be noted that because plates RC1 and RC2 present a different geometry towards the incoming flow during the forward and the backward strokes, a net side-force is generated. The net side-force is computed as $\overline{F}_x$ in contrast to the average side-force computed as $\overline{|F_x|}$ in $\overline{C}_S$. The net side-forces generated by plates RC1 and RC2 are 4.0% and 7.3% of the average side-force generated by plate R0, respectively, in the direction opposite that of the forward stroke. This would cause an AUV to turn if a static geometry is used as a propulsor. A reduction in all of the forces could increase the efficiency if the side-force or the torque is reduced more than the thrust. However, as shown in figures 3.5(b,d), both measures of efficiency for plates RC1 and RC2 do not differ significantly from those for plate R0.

Dynamic chord-wise tip curvature actuation

The Nitinol-actuated plate AC1 is used to determine the impact of a dynamically-actuated curvature. The actuation profiles used to contract the Nitinol wire are created by modifying the duty cycles of square waves with an identical frequency to that of the motion. Actuation profiles 1, 2, and 3 have duty cycles (DC) of 12.5%, 25%, and 50%, respectively, with phase angles θ_F of 67.5°, 0°, and 0°, respectively, for actuation during the forward stroke and phase angles θ_B of 247.5°, 180°, and 180°, respectively, for actuation during the backward stroke. These actuation profiles cause the wire to actuate and remained contracted during the forward stroke from a t^* of 0.1875 to 0.3125, 0 to 0.25, and 0 to 0.5 respectively and during the backward stroke from a t^* of 0.6875 to 0.8125, 0.5 to 0.75, and 0.5 to 1 respectively. Characteristics of the actuation profiles and the t^* intervals when the plates are contracted are summarized in tables 3.2 and 3.3. The parameters were selected to cover a variety of possible profiles to assess whether the decrease in forces could be triggered and maintained effectively and arbitrarily. It should be noted that within a single trial, actuation only occurs during either the forward or the backward stroke.

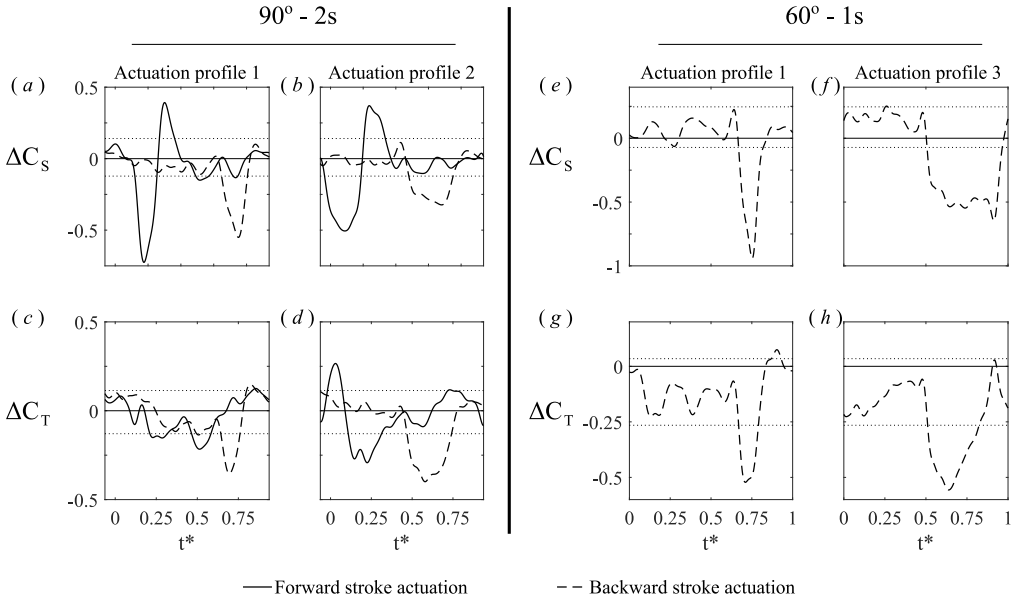

Figure 3.6: Typical instantaneous ΔC_S (a,b,e,f) and ΔC_T (c,d,g,h) as functions of t^* over one full cycle after reaching steady state for plate AC1. Panels (a-d) correspond to the 0.381 mm thick polycarbonate plate with a 90° stroke angle and a 2 s stroke time, while panels (e-h) correspond to the 0.508 mm thick polycarbonate plate with a 60° stroke angle and a 1 s stroke time. Panels (a,c), (b,d), (e,g), and (f,h) use the actuation profiles indicated on the top of panels (a,b,e,f). The characteristics of the actuation profiles and the t^* intervals when the plates are contracted are summarized in tables 3.2 and 3.3.

Profile	DC (%)	θ_F (°)	θ_B (°)
1	12.5	67.5	247.5
2	25	0	180
3	50	0	180

Table 3.2: Characteristics of the actuation profiles.

	Contracted duration (t^*)	
Profile	During forward stroke	During backward stroke
1	0.1875 - 0.3125	0.6875 - 0.8125
2	0 - 0.25	0.5 - 0.75
3	0 - 0.5	0.5 - 1.0

Table 3.3: Contraction timings of the actuation profiles.

The impact of actuation is assessed by evaluating the difference in the generated forces between actuated and unactuated cases. These instantaneous differences in

C_S and C_T are denoted ΔC_S and ΔC_T, respectively, in figure 3.6 for a typical cycle. The dotted horizontal lines in figures 3.6(a,b,e,f) and 3.6(c,d,g,h) correspond to the noise level of the transducer during the motion, computed from the maximum ΔC_S and ΔC_T, respectively, between trials with identical kinematics when no actuation occurs. The solid line corresponds to actuation during the forward stroke, while the dashed line corresponds to actuation during the backward stroke. For a 60° stroke angle and a 1 s stroke time, convection cooling during the forward stroke, when the incoming water flows directly over the wire, prevents actuation. It should be noted that the solid horizontal line at zero is only meant to highlight the zero-line and does not correspond to any data. The results for the 0.381 mm thick polycarbonate plate with a 90° stroke angle and a 2 s stroke time using actuation profiles 1 and 2 are shown in figures 3.6(a-d), while the results for the 0.508 mm thick polycarbonate plate with a 60° stroke angle and a 1 s stroke time using actuation profiles 1 and 3 are shown in figures 3.6(e-h).

Comparison of ΔC_S or ΔC_T in figure 3.6 across all actuation profiles shows that the forces are decreased whenever the plate is actuated, which corroborates the previous conclusion regarding the impact of curvature, with the added benefit that the reduction in forces can be triggered and maintained arbitrarily. This can be seen by comparing the duration of the decrease in forces between actuation profiles 1 and 3 in figures 3.6(e,g) and 3.6(f,h), respectively. Using actuation profile 1, the largest impact is achieved; the maximum reduction in C_S is by 12.8% and 9.0% while that in C_T is by 8.8% and 12.3% at a 90° stroke angle with a 2 s stroke time and a 60° stroke angle with a 1 s stroke time, respectively, when compared with the case without actuation. It should be noted that characterization of the Nitinol wire by actuating the wire on a motionless plate in quiescent fluid generates forces below the noise threshold. This implies that the decrease in forces is primarily due to a static change in curvature rather than a dynamic bending motion. These results show that dynamic chord-wise curvature control through Nitinol wire actuation can be triggered and maintained effectively to reduce the generated forces by approximately 10%. Furthermore, this decrease in the forces is comparable to the decrease in the peak amplitude of C_S and C_T from plate RC1, which had a similar chord-wise tip radius of curvature and β as plate AC1, meaning that if greater curvatures could be realized, the forces could potentially be decreased by approximately 31%, as seen with plate RC2. Characterization of the influence of flexibility will require future studies.

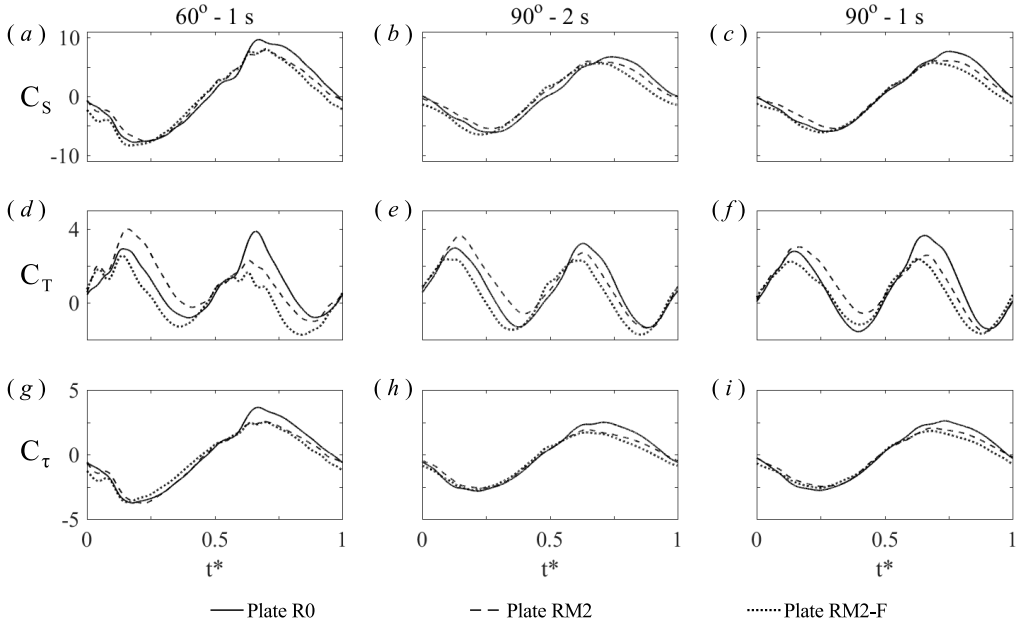

Figure 3.7: Typical instantaneous C_S (a-c), C_T (d-f), and C_τ (g-i) as functions of t^* over one full cycle after reaching steady state for plates R0, RM2, and RM2-F. Panels (a,d,g), (b,e,h), and (c,f,i) have the same kinematics given in the form $\phi - t_s$. The first half of all of the plots, $0 < t^* < 0.5$, corresponds to the forward stroke, when the rigid curved plates are concave to the incoming flow, while the second half of all of the plots, $0.5 < t^* < 1$, corresponds to the backward stroke, when the rigid curved plates are convex to the incoming flow.

Isolating the effect of curvature with rigid baselines

Plate RM2 is used to isolate the effect of curvature as the only difference between plates RM2 and R0 is that plate RM2 has a tip radius of curvature of 23 mm and a β of 0.5. Plate RM2-F is used to study the impact of spanwise flow, which has been shown to significantly affect the generation of tip vortices and thrust [21]. By attaching a fence to the tip of plate RM2 to create plate RM2-F, flow in the spanwise direction near the tip of the plate is impaired, because here, during the forward stroke, the flow is redirected normal to the plate. The instantaneous C_S, C_T, and C_τ as functions of t^* are shown in figure 3.7 for a typical cycle and the $\overline{C}_S$, $\overline{C}_T$, η_1, and η_2 per cycle are shown in figure 3.8 for plates R0, RM2, and RM2-F.

Comparison of the instantaneous C_S in figures 3.7(a-c) between plates R0 and RM2 shows that curvature decreases the peak side-force generated, similar to the conclusion from the results of the rigid curved plates with a smaller planform area. However, adding a fence with plate RM2-F causes the side-force generated during the accelerating portion of the forward stroke to approach that generated by the baseline

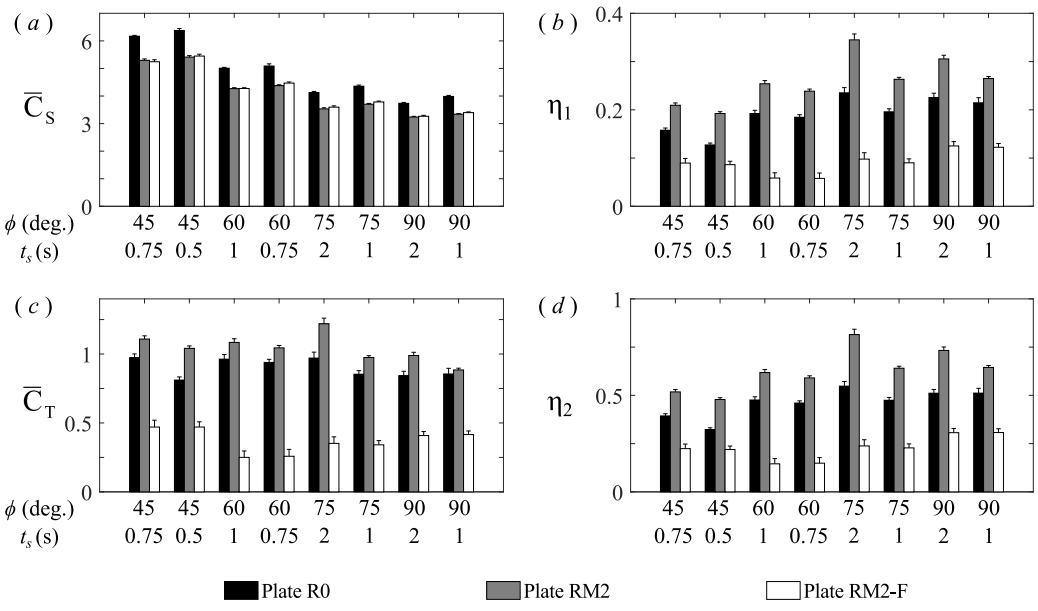

Figure 3.8: Average side-force coefficient $\overline{C}_S$ (a), average thrust coefficient $\overline{C}_T$ (c), and two definitions of efficiency, η_1 (b) and η_2 (d), over a cycle as functions of the plate kinematics for plates R0, RM2, and RM2-F. The x-axis indicates the stroke angle ϕ on the top row and the stroke time t_s on the bottom row.

flat plate. The results from the instantaneous C_τ in figures 3.7(g-i) corroborate the results from C_S. Comparison of the instantaneous C_T in figures 3.7(d-f) between the plates R0 and RM2 shows that curvature significantly decreases the thrust generated during the backward stroke, similar to the previous conclusion from the results of the rigid curved plates with a smaller planform area, but, interestingly, increases the thrust generated during the forward stroke; using the data in figure 3.7, plate RM2 increases the peak thrust generated by 22.4% on average during the forward stroke but decreases the peak thrust by 26.4% on average during the backward stroke compared with plate R0. However, the addition of a fence with plate RM2-F negates the benefit of presenting a concave geometry into the flow, causing the thrust during the forward stroke to decrease even below that of the rigid flat plate.

Comparison of the overall forces generated and the efficiency per cycle in figure 3.8 corroborate the previous result that plate RM2 decreases the side-force generated and increases the thrust generated, which may not be evident as plate RM2 increases the thrust during the forward stroke but decreases the thrust during the backward stroke. Furthermore, the addition of a fence decreases the performance of plate RM2. As expected, because plate RM2 decreases the side-force and increases the thrust, the efficiencies η_1 and η_2 are increased by 34.3% and 36.4%, respectively.

Additionally, the net side-force generated is only 3.3% of the average side-force of the baseline flat plate, meaning that replacing a flat plate propulsor with a curved plate of an identical planform area may be viable.

Brief discussion of planform area

The impact of the planform area can be isolated by comparing the results from plates RC2 and RM2 because they have an identical β but different planform areas. Comparison of the instantaneous C_S between the two plates in figures 3.4(a-c) and figures 3.7(a-c), respectively, shows that curvature alone (comparing plate RM2 to R0) has a minimal effect during the forward stroke and a small effect during the backward stroke. Therefore, the result that plate RC2 decreases the peak C_S and the overall $\overline{C}_S$ per cycle more than RM2 decreases those when both are compared against plate R0 must be accounted for by plate RC2's reduced planform area (due to its smaller chord near the tip of the plate). This provides further evidence that decreasing the planform area creates a more streamlined geometry which reduces the side-force, previously suggested.

Comparison of the instantaneous C_T between plates RC2 and RM2 in figures 3.4(d-f) and figures 3.7(d-f), respectively, shows that the benefit of presenting a concave geometry towards the incoming flow is negated if the planform area is reduced. These results show that modifying the planform area by changing the chord near the tip of the plate can either significantly increase or decrease the generated thrust during the forward stroke. Furthermore, this highlights the required interaction between the planform area and the curvature to increase the thrust generated during the forward stroke which is illustrated in the DPIV results in a later section.

Passive chord-wise tip curvature actuation

Motivated by the results from plate RM2, plate AM2 is designed to passively snap-buckle and present a concave geometry into the flow during both the forward and the backward strokes. The instantaneous C_S, C_T, and C_τ as functions of t^* are shown in figure 3.9 for a typical cycle and the $\overline{C}_S$, $\overline{C}_T$, η_1, and η_2 per cycle are shown in figure 3.10 for plates R0, RM2, and AM2. Plate AM2 is tested on a smaller subset of the kinematics as only large angular velocities induce snap-buckling.

From figures 3.9(d-f), the significant increase in thrust during both strokes is apparent as plate AM2 increases the peak thrust by 121% on average compared with plate R0. It should be noted that the flat region immediately preceding the peak in C_T corresponds to the period of time when snap-buckling occurs; during this transition

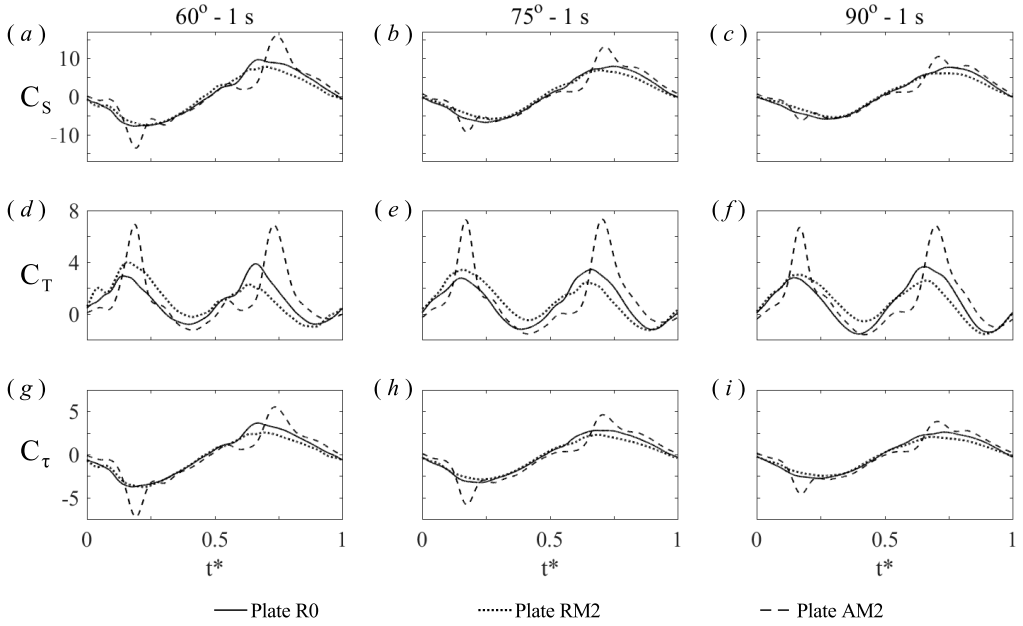

Figure 3.9: Typical instantaneous C_S (a-c), C_T (d-f), and C_τ (g-i) as functions of t^* over one full cycle after reaching steady state for plates R0, RM2, and AM2. Panels (a,d,g), (b,e,h), and (c,f,i) have the same kinematics given in the form $\phi - t_s$. The first half of all of the plots, $0 < t^* < 0.5$, corresponds to the forward stroke, when the rigid curved plates are concave to the incoming flow, while the second half of all of the plots, $0.5 < t^* < 1$, corresponds to the backward stroke, when the rigid curved plates are convex to the incoming flow.

from one curved geometry to another, the thin polycarbonate sheet is completely passive to the flow, so no additional force is generated. However, snap-buckling is an abrupt process causing the peaks in C_S shown in figures 3.9(a-c). Plate AM2 increases the peak side-force by 47.6% on average compared with plate R0. The results from the instantaneous C_τ in figures 3.9(g-i) corroborate the results from C_S. Overall, plate AM2 increases $\overline{C}_T$ per cycle by 34.8% but causes $\overline{C}_S$ to approach that generated by the baseline flat plate, which increases η_1 and η_2 by 30.1% and 23.6%, respectively, compared with plate R0. These results show that using a snap-buckling design can successfully take advantage of an increased thrust during both the forward and the backward strokes with the added benefit, compared with a rigid curved design, that no net side-force should be generated as the geometry presented into the flow is identical during both strokes.

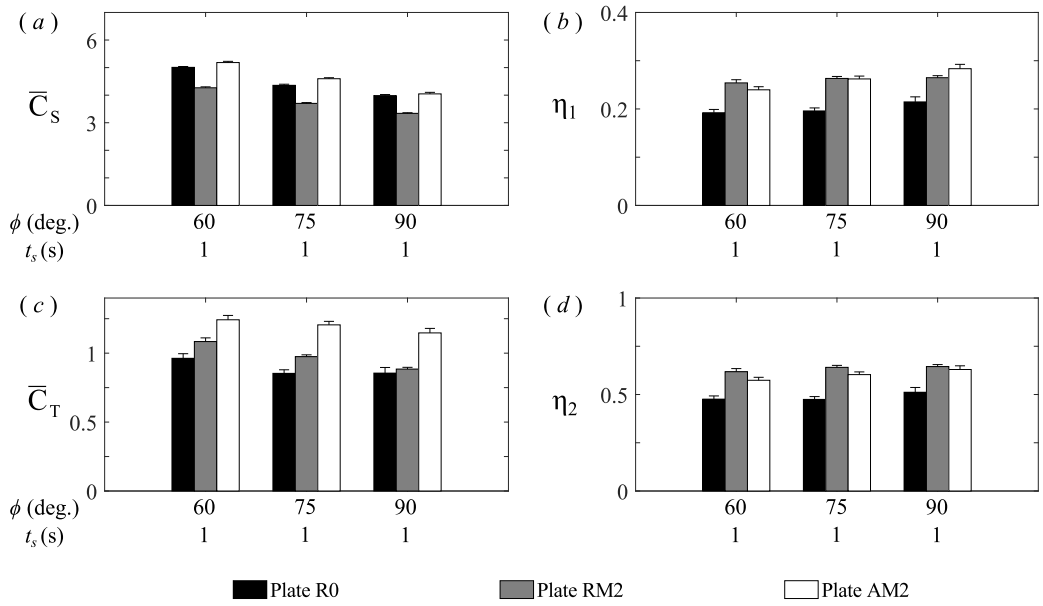

Figure 3.10: Average side-force coefficient $\overline{C}_S$ (a), average thrust coefficient $\overline{C}_T$ (c), and two definitions of efficiency, η_1 (b) and η_2 (d), over a cycle as functions of the plate kinematics for plates R0, RM2, and AM2. The x-axis indicates the stroke angle ϕ on the top row and the stroke time t_s on the bottom row.

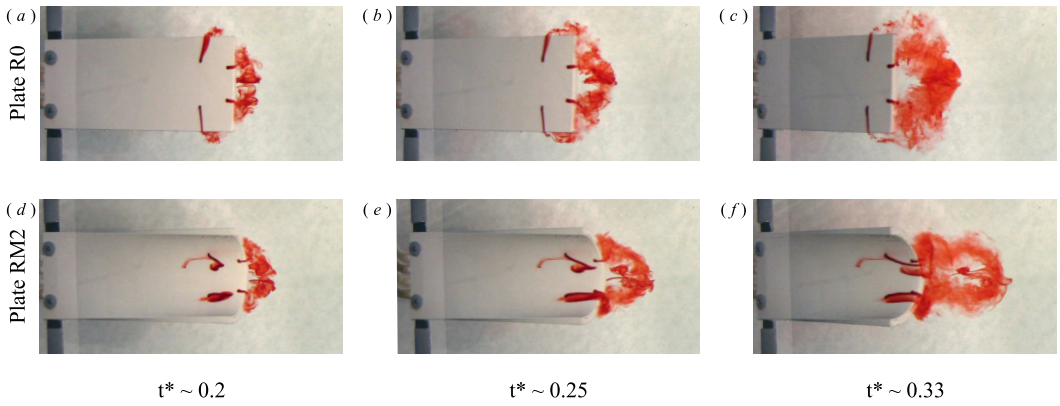

Figure 3.11: Dye visualization of the flow near the tip of plates R0 (a-c) and RM2 (d-f) from four injection points during the first forward stroke. Snapshots are taken at a t^* of approximately 0.2 (a,d), 0.25 (b,e), and 0.33 (c,f). The plates move out of the page with $\phi = 60°$ at $t_s = 1$ s and are filmed from a location normal to the initial position of the plates to provide a better view of the vortex structures generated behind the plates.

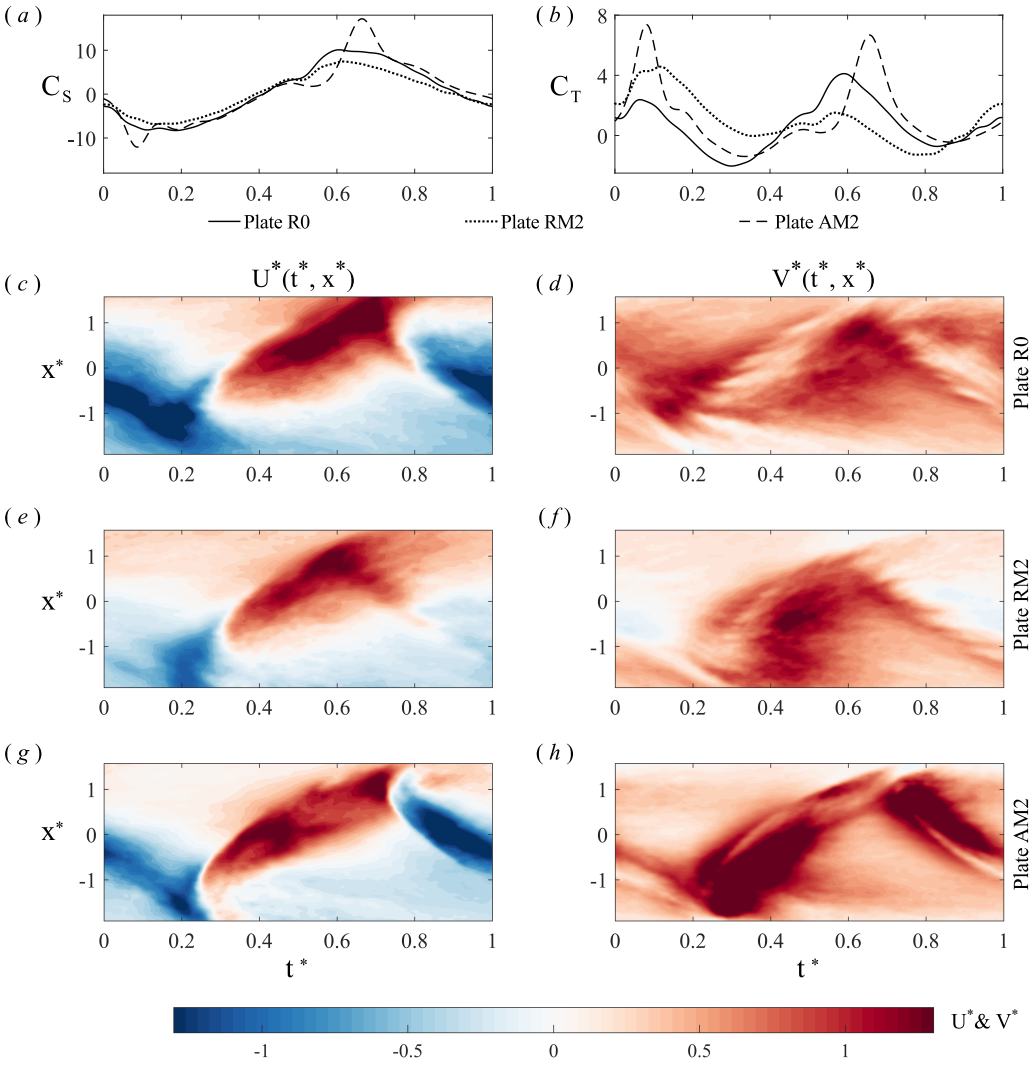

Figure 3.12: Phase averaged C_S (a) and C_T (b) with their corresponding phase averaged flow fields, U^* (c,e,g) and V^* (d,f,h), respectively, from a 60° stroke angle and a 1 s stroke time after reaching steady state as functions of x^* and t^*. Visualization of the flow field is created by plotting the velocity profiles in time along a selected line in the x-direction at a fixed y-location from the near wake of the pitching plates. The orientation of the pitching motion is identical to that shown in figure 3.1(b). Relative to the orientation in figure 3.1(b), flow in the positive x-direction corresponds to a positive U^*, while flow in the negative y-direction corresponds to a positive V^*. Panels (c,d), (e,f), and (g,h) correspond to the flow field generated by plates R0, RM2, and AM2, respectively, as indicated on the right of panels (d,f,g), respectively.

Dye visualization and DPIV

Dye visualization is used to provide qualitative insight into the flow structures generated by plates R0 and RM2 to investigate possible sources for plate RM2's significantly increased thrust and efficiency compared with that of plate R0. Plate AM2 is effectively rigid during each stroke and therefore no dye visualization is provided for the first forward stroke as the generated flow field would be nearly identical to that of plate RM2. The first forward stroke is investigated to highlight the effect of the plate's geometry without the influence of a previously generated flow field. The locations of the dye injection points are concentrated near the tip of the plates because the flow is similar on the pressure side of the two plates at locations closer to the pitching axis. Although not visualized, flow at locations closer to the pitching axis simply move in the chord-wise direction away from the centerline towards the edge of the plate. This flow rolls up into an edge vortex that tends to follow the trajectory of the pitching plate as expected from DDPIV studies of a flat plate by Kim and Gharib [21]. This behavior is also exhibited by plate RM2 because the curvature at locations closer to the pitching axis is small compared with that near the tip of the plate.

Representative snapshots of the generated three-dimensional flow field near the tip of plates R0 and RM2 pitching with a 60° stroke angle and a 1 s stroke time are shown in figure 3.11. The flow behaves in a similar manner as that from other kinematic sets. From the dye visualization of plate R0 in figures 3.11(a-c), the dye originating from the two injection points closest to the tip shows a developing tip vortex which tends to follow the trajectory of the pitching plate with minimal outwards motion. The dye originating from the other two injection points shows a chord-wise flow away from the centerline, taking the most direct path towards the edge of the plate, as expected from studies by Kim and Gharib [21]. From the dye visualization of plate RM2 in figures 3.11(d-f), the dye originating from the two injection points closest to the tip shows a smaller developing tip vortex which almost immediately sheds by $t^* \sim 0.25$ and appears to transition into a shape similar to a vortex ring by $t^* \sim 0.33$. The dye originating from the other two injection points shows a flow moving towards the tip of the plate instead of the edge of the plate as seen with plate R0. Additionally, the influence of the geometry moves this flow towards the centerline of the plate to eventually supplement the development of the tip vortex. Compared with plate R0, the geometry of plate RM2 appears to cause the tip vortex to shed earlier and travel further downstream. Furthermore, this geometry appears to 'channel' the flow near the tip of the plate, causing the dye to move towards the

tip rather than the edge of the plate. The early separation of the tip vortex of plate RM2 may have been influenced by the increased spanwise flow near the tip, due to the geometry of the plate, or the induced velocity of the edge vortices which attach at an angle on the suction side of the plate.

DPIV is used to provide quantitative preliminary insight into the mechanism that increases the thrust and the efficiency of plates RM2 and AM2 compared with those from plate R0 at $\phi = 60°$ and $t_s = 1\,\text{s}$. The flow behaves in a similar manner as that from other kinematic sets. This two-dimensional visualization technique involves high speed imaging of the illuminated particles following the flow. The laser sheet is illuminated along the mid-plane of the plate, indicated by the dashed line in figure 3.3, where three-dimensional effects are minimal. Evolution of the wake in time is illustrated in figure 3.12 by first phase averaging the flow field based on the pitching frequency of the plate after reaching steady state, then selecting a single line along the x-direction at a fixed y-location, and finally plotting the velocity field along this line at every instance in time. The line in the x-direction at a fixed y-location is taken at a distance of 1.17 times the span from the pitching location of the plate. The orientation of the pitching motion in figure 3.12 is identical to that shown in figure 3.1(b) and, relative to this orientation, flow in the positive x-direction corresponds to a positive U^*, while flow in the negative y-direction corresponds to a positive V^*. The corresponding phase averaged force data for the generated flow field is shown in figures 3.12(a,b); the positive direction of the forces is denoted by the axes in figure 3.1(b). The non-dimensional component of velocity in the direction of C_S and C_T, $U^* = U/U_{tip}$ and $V^* = V/U_{tip}$, respectively, along a line as functions of t^* and $x^* = x/L$, where $L = s(\sin 30^o)$ is the excursion amplitude of the plate's tip, are shown in figures 3.12(c,e,g) and figures 3.12(d,f,g), respectively. From figure 3.12, the U^* velocity field generated by all of the plates appears similar, which is reasonable, as C_S is similar between all three plates. Additionally, no obvious event in the flow history is linked with the peak in C_S for plate AM2, which implies that these peaks are primarily due to an abrupt snap-buckling motion rather than a flow phenomenon.

Comparison of the V^* velocity field between the three plates illustrates a possible cause of the improved thrust performance of plate AM2. Compared with plate R0, plate AM2 generates a V^* velocity field of a significantly greater magnitude. From a simple momentum argument, the greater the momentum imparted to the flow, the greater the thrust generated. The large thrust peaks of plate AM2 are a

result of the dark red regions in figure 3.12(h). Within these regions, the flow is almost impulsively 'channeled' outwards from the plate in the spanwise direction immediately following snap-buckling, illustrated by the abrupt change in color around a t^* of 0.2 and 0.7; the peak in C_T appears in the force measurements before the corresponding event in the flow because the recently-imparted momentum into the flow has to convect to the line where the velocity field is sampled.

A similar 'channeling' effect is present during the forward stroke of plate RM2 in figure 3.12(f). Immediately following a change in direction, when a concave geometry is presented into the flow around $t^* = 0.2$, a red concentrated region appears, but with a smaller magnitude than that from plate AM2 because no abrupt snap-buckling occurs. However, when a convex geometry is presented into the flow during the backward stroke, the V^* velocity approaches and even decreases below zero, which explains the poor thrust performance of the rigid curved geometries during the backward stroke, as described in previous sections. It should be noted that the velocity field interestingly resembles a pulsing flow, as most of the thrust is generated during the forward stroke followed by a 'recovery' phase during the backward stroke. Overall, these results suggest that the peak in C_S for plate AM2 is caused by the abrupt snap-buckling motion and that the increase in thrust, during the forward stroke of plate RM2 and both strokes of plate AM2, may have been caused by a 'channeling' effect, where the incoming flow is redirected outwards from the plate in the spanwise direction. A definitive answer regarding the underlying mechanisms requires future studies with a quantitative three-dimensional flow visualization technique.

3.4 Closing remarks

The effect of chord-wise tip curvature on the hydrodynamic forces was tested with flapping plates of different geometries. The first case study involved the impact of physically bending the two corners of a plate towards each other. From the baseline study using rigid curved geometries, the results suggested that increasing the curvature decreases the hydrodynamic forces and torques with a minimal loss in efficiency. This concept was explored using a plate with a dynamically-actuated chord-wise tip curvature using a Nitinol wire, which corroborated the result from the baseline study with the added benefit that the amplitude and the duration of the decrease in forces could be arbitrarily modulated.

The second case study involved isolating the impact of chord-wise tip curvature by

using plates with a similar planform area to that of the baseline flat plate. Similar to the previous case study, increasing the curvature decreased the generated forces and torques, with the exception that the thrust generated during the forward stroke increased. This benefit was leveraged using a snap-buckling plate to present a concave geometry into the flow during both the forward and the backward strokes, which significantly increased the overall thrust generated per cycle. Investigation through dye visualization and DPIV suggested that this increase in thrust may have been due to a 'channeling' effect, where the incoming fluid is redirected outwards from the tip of the plate rather than moving around it as a result of the geometry of the plate, imparting more momentum to the flow in the thrust direction. Future studies using a quantitative three-dimensional flow visualization technique will be necessary to provide a more definitive answer regarding the underlying mechanisms.

These results suggest that two new mechanisms could potentially be used to increase the maneuverability or the efficiency of AUVs. If the goal is improved maneuverability, implementing actuated chord-wise tip curvature shows promise to assist in braking and turning without needing to modify the trajectory. If the goal is improved efficiency, replacing a rigid flat plate propulsor with a snap-buckling plate of a similar planform area shows promise to achieve this goal, provided the angular velocity of the plate is sufficient to snap-buckle the material.

Chapter 4

TRAJECTORY OPTIMIZATION

4.1 Opening remarks

The purpose of this study is to demonstrate the potential of experimentally optimizing trajectories for generating propulsion and to compare different methods of propulsion. Trajectories optimized for generating side-force, similar to how a pectoral fin would generate propulsion for a fish, are compared between cases when a fully three-dimensional trajectory is allowed, to cases when a trajectory is constrained to a straight line in the x-y plane. (The orientation of the x-y axes is shown in figure 4.1.) These trajectories are then compared with trajectories optimized for generating thrust, similar to how a caudal fin would generate propulsion for a fish, to determine which is more efficient. The objective of the optimization is defined based on the application that a specific force in a specific direction would need to be generated with maximum efficiency; therefore the fitness function is weighted based on both the error between the experimentally obtained force and the force set-point, as well as the efficiency of the maneuver. The trajectories are executed using a SPM, due to its capability to actuate arbitrary paths in three-dimensions with high torques, and optimized using CMA-ES, due to its deterministic nature and fast convergence properties. The generated trajectories are inspired by the motion of a bird's wing and a fish's pectoral and caudal fins. Both animals use a flapping motion to generate propulsion, albeit the mechanisms used and the direction in which the forces are generated vary; therefore, because trajectories could be implemented on a vehicle in a manner similar to how they are implemented in nature, parameters important to flapping propulsion in birds and fish are considered simultaneously. The motion of a bird's wing during forward flight could be implemented by aligning the net force vector with the desired direction of motion for an underwater vehicle; the motion of a fish's pectoral fin during locomotion could be implemented if two propulsors, one on each side, are used; the motion of a fish's caudal fin during locomotion could be implemented as a rear propulsor. To the best of the author's knowledge, an experimental optimization where a multitude of parameters are simultaneously optimized has not been conducted. The advantage of conducting the optimization experimentally comes from the speed at which data sets, which preserve the complex flow physics, can be obtained. The advantage of simultaneously optimizing

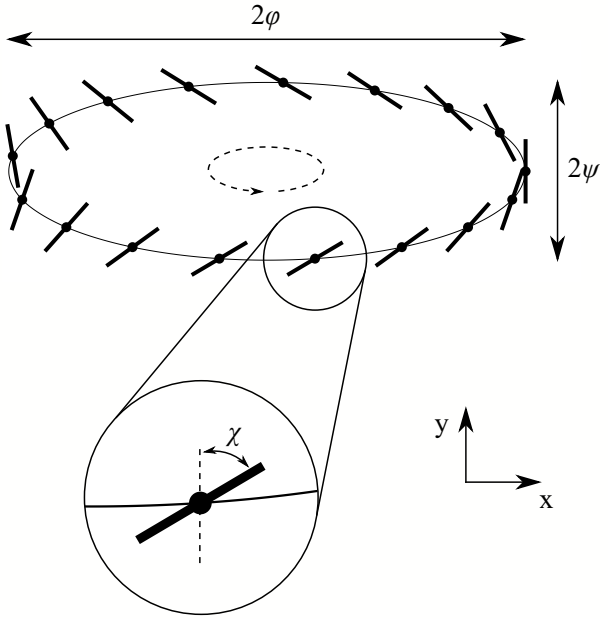

Figure 4.1: Definition of ϕ, ψ, and χ illustrated along a typical trajectory path. The direction of motion is indicated by the dashed arc in the middle of the trajectory. The flat angled lines along the path indicate the angle of attack and the location of the fin at different points in time. The x and y-axes indicate the positive direction of the forces in the x and y-directions. The z-axis points out of the page.

the parameters comes from fully exploring the parameter space and preserving the nuances between parameter interactions. All tests begin from quiescent flow and continue without an imposed co-flow to investigate the infinite Strouhal number limit.

4.2 Experimental setup

Trajectory Generation

The parameters used to generate the trajectory are inspired by fin and wingtip trajectories of fish and birds used for locomotion and maneuverability. Studies of fish swimming and drag-based locomotion have highlighted the importance of the stroke angle ϕ and the frequency f for thrust generation and efficiency. Studies of bird flight have highlighted the importance of the amplitude of rotation χ, (this angle is relative to 90° as shown in figure 4.1), the phase offset of the rotation timing β, and the non-sinusoidal rotational acceleration profiles governed by an adjustable parameter K_v. Furthermore, an overview of general wingtip trajectories found that

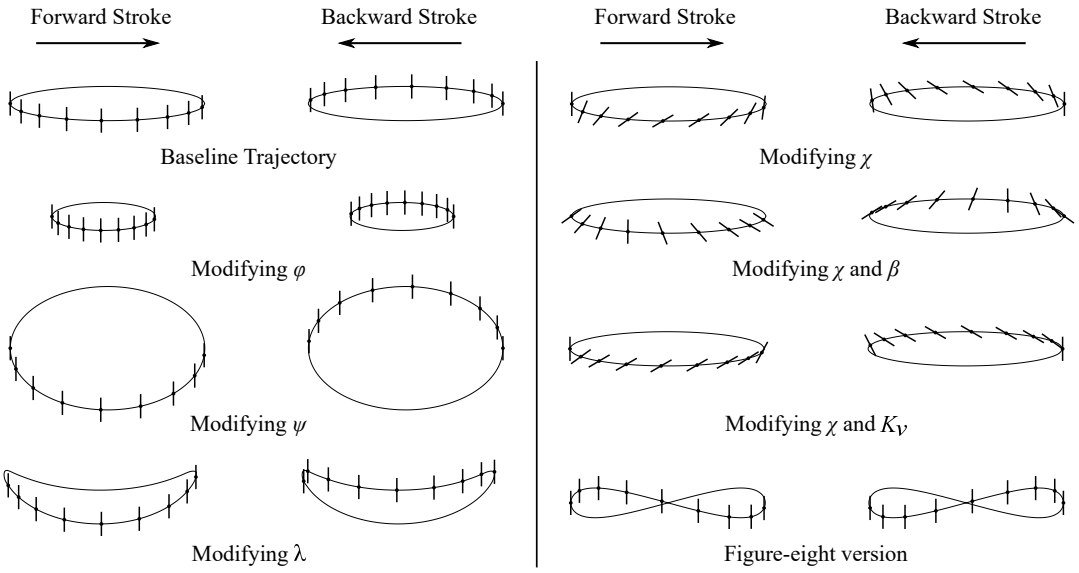

Figure 4.2: How modifying the parameters of interest, individually or in pairs, can change a baseline trajectory. The enclosed path corresponds to the trajectory traced by the center of the fin's tip during a single cycle. The short lines correspond to the fin's angle of attack along the trajectory from an axis-angle representation while the dots correspond to the axis of rotation and location of the center of the fin's tip. The forward stroke, where the fin moves from left to right, and the backward stroke, where the fin moves from right to left, are illustrated separately.

birds move their wings in a figure-eight or an elliptical shape, many of which have an overall camber, accounted for with an adjustable parameter λ. The angle of the stroke deviation from a horizontal line is parameterized with ψ. The definitions of ϕ, ψ, and χ on the trajectory are shown in figure 4.1. An illustration of how each variable can modify a baseline trajectory is shown in figure 4.2 and an amalgam of example trajectories are shown in figure 4.3 to demonstrate the breadth of possible trajectories. In general, increasing ϕ makes the trajectory longer, increasing ψ makes the trajectory wider, increasing λ increases the overall camber, increasing χ increases the amplitude of $\alpha(t)$, changing β modifies where along the trajectory $\alpha(t) = 90°$, and increasing K_v causes $\alpha(t)$ to approach a square wave.

Studies of fish maneuverability have detailed a c-start motion where the caudal fin is rapidly pitched in a certain direction. This rapid acceleration inspired the implementation of a speed up parameter γ, which dictates the relative speed of specific defined 'zones' of the trajectory, governed by a categorization parameter S. The trajectory is split into two equal length halves. The parameter γ dictates the

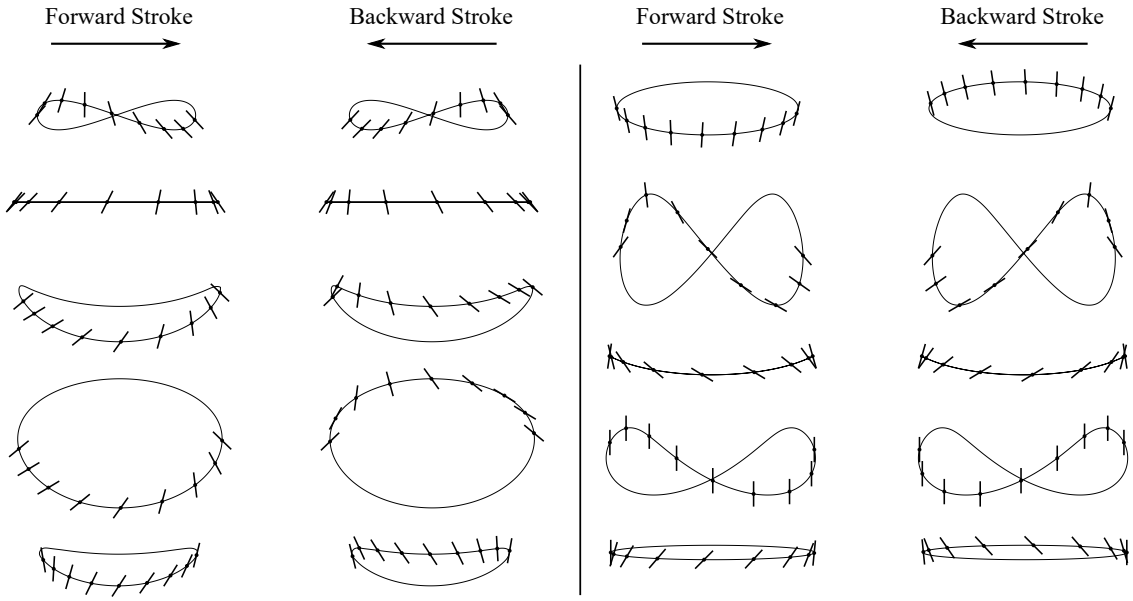

Figure 4.3: Variety of trajectory shapes and rotation timings. The enclosed path corresponds to the trajectory traced by the center of the fin's tip during a single cycle. The short lines correspond to the fin's angle of attack along the trajectory from an axis-angle representation while the dots correspond to the axis of rotation and location of the center of the fin's tip. The forward stroke, where the fin moves from left to right, and the backward stroke, where the fin moves from right to left, are illustrated separately.

relative speed-up of one half of the trajectory compared with the other half. (For example, if $\gamma = 1.2$, this would imply that one half of the trajectory occurs 20% faster than the other half of the trajectory. A value of 1 corresponds to no relative speed up.) For this study, the points along the trajectory that define the start and end points of each half are fixed. There are four possible 'split' points. Considering an origin at the centroid of the trajectory, an x-axis along the direction of the stroke angle, and a y-axis perpendicular to the x-axis, the 4 points are designated as follows: two points are located along the x-axis at the minimum and maximum x-locations of the trajectory's path while the other two points are located along the y-axis at the minimum and maximum y-locations of the trajectory's path. These points are labeled 'E', 'F', 'G', and 'H' moving in a clockwise manner starting from the 9 O'clock position as shown in figure 4.4. The parameter S dictates which arcs spanning half of the trajectory are sped up. The values of 1, 2, 3, and 4 correspond to a speed-up of arcs $\widehat{GE}$, $\widehat{HF}$, $\widehat{EG}$, and $\widehat{FH}$, respectively. A value of 0 indicates no relative speed-up occurs.

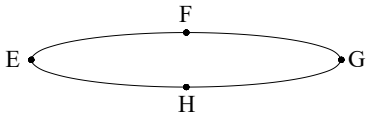

Figure 4.4: The location of points E, F, G, and H along a typical trajectory.

Parameter	Symbol	Min. Value	Max. Value
Stroke angle	ϕ	10°	40°
Deviation angle	ψ	0°	20°
Rotation angle	χ	−70°	70°
Rotation phase	β	0	2π
Speed code	S	0	4
Speed up value	γ	1	1.3
Rotation acceleration	K_v	0	1
Stroke deviation	λ	0	1
Frequency	f	0.15 Hz	0.2 Hz

Table 4.1: Range of parameters.

The 9 variables listed in table 4.1 with their allowed minimum and maximum values fully define either a figure-eight or an elliptical trajectory. The maximum values are set primarily based on mechanical and safety restrictions. Throughout this section, a variable with a numerical subscript indicates a temporary variable. The 32 unique points of the trajectory are generated as follows. First, a 2D figure-eight or ellipse is created using parametric equations. For a circle,

$$x_1 = A\cos(t_1), \qquad y_1 = B\sin(t_1) \tag{4.1}$$

is used, while for a figure-eight,

$$x_1 = A\cos(t_1), \qquad y_1 = B\sin(2t_1) \tag{4.2}$$

is used, where $0 \leq t_1 \leq 2\pi$, $A = \sin(\phi)$, and $B = \sin(\psi)$.

Second, if $\lambda > 0$, the trajectory is deformed around an arc with a constant radius. The value of λ governs the deviation angle between points E and G on the original trajectory and points E′ and G′ on the deformed trajectory. The deviation angle is limited to $A/3$ so that the trajectories do not become too distorted. The deviation takes the form of $\lambda A/3$ where $0 \leq \lambda \leq 1$. The radius of the arc is solved for with three points, one at the un-deformed trajectory's centroid and two at points E′ and G′, the desired locations points E and G are deformed to. The radius of the arc that

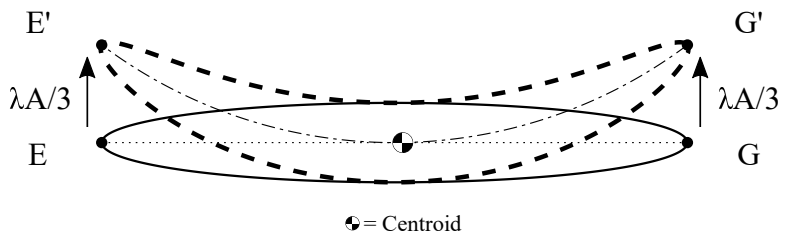

Figure 4.5: Demonstration of how a trajectory is deformed onto an arc of constant radius. The solid line denotes the original trajectory. The dotted line denotes the camber line of the original trajectory. The dash-dot line denotes the constant radius arc, or camber line, the trajectory is deformed about. The dashed line denotes the deformed trajectory. The parameter λ is used to denote the amount points E and G, on the original trajectory, are shifted to points E′ and G′, on the deformed trajectory.

pass through these three points is

$$R_1 = \frac{A^2 + (\lambda A/3)^2}{2\lambda A/3}, \tag{4.3}$$

illustrated in figure 4.5. (It should be noted that to keep the trajectory centered, the centroid of the deformed trajectory is calculated and shifted accordingly.)

With this radius, a 'camber' line is generated of the form:

$$x_2 = R_1 \cos(t_2), \qquad y_2 = R_1 \sin(t_2) \tag{4.4}$$

$$3\pi/2 - \arcsin(A/R_1) \leq t_2 \leq 3\pi/2 + \arcsin(A/R_1)$$

To deform the original trajectory around this camber line, the slope is first calculated

$$S_1 = (dy_2/dt)/(dx_2/dt) \tag{4.5a}$$

$$= -\cos(t_2)/\sin(t_2) \tag{4.5b}$$

and then inverted, $S_2 = -1/S_1$, to find the perpendicular slope at all points. Next, a new distorted trajectory is generated by placing points normal to the camber line at a distance equal to the original y_1 location of that point. The displacements from the camber line, dx_2 and dy_2, are calculated as follows:

$$dx_2^2 + dy_2^2 = y_1^2 \tag{4.6a}$$

$$dy_2 = S_2 dx_2 \tag{4.6b}$$

$$dx_2^2 + S_2^2 dx_2^2 = y_1^2 \tag{4.6c}$$

$$dx_2^2(1 + S_2^2) = y_1^2 \tag{4.6d}$$

$$dx_2 = \sqrt{y_1^2/(1 + S_2^2)} \tag{4.6e}$$

The displacements are then added to the values along the camber line to get the distorted trajectory.

$$x_3 = x_2 + dx_2 \tag{4.7a}$$

$$y_3 = y_2 + dy_2 \tag{4.7b}$$

If $\lambda = 0$, no trajectory distortion occurs and the values of x_1 and y_1 are relabeled as x_3 and y_3.

Third, the 2D trajectory is converted into spherical coordinates:

$$R_2 = \sqrt{x_3^2 + y_3^2} \tag{4.8a}$$

$$\theta_1 = \arctan[R_2/\cos(\phi)] \tag{4.8b}$$

$$\theta_2 = \arctan(y_3/x_3) \tag{4.8c}$$

and projected onto a sphere with a radius of 1:

$$x_4 = \sin(\theta_1)\cos(\theta_2) \tag{4.9a}$$

$$y_4 = \sin(\theta_1)\sin(\theta_2) \tag{4.9b}$$

$$z_4 = \cos(\theta_1) \tag{4.9c}$$

Fourth, the velocity profiles are created. When creating the time vector for the velocity profiles, the objective was to have a constant velocity throughout the entire cycle for simplicity; however, the impulsive change in direction for trajectories with a small ψ would damage the transducer. Therefore an offset transitions from a sinusoidal velocity profile at a small ψ to a constant velocity profile at a large ψ. The offset used is

$$V_2 = \frac{5L_1\, V_1}{8(1-\gamma)} \tag{4.10}$$

where

$$V_1 = \text{erf}(138B^2/A - 0.8)/3.2 + 0.232$$

and L_1 is the arc length computed via

$$L_1 = \sum_{i=2}^{N} \sqrt{(x_4^i - x_4^{i-1})^2 + (y_4^i - y_4^{i-1})^2 + (z_4^i - z_4^{i-1})^2}$$

Next, the average velocity during both halves of the trajectory are computed by taking the distance (arc length divided by two) and dividing this by the time needed

to traverse this distance, which is a function of γ.

$$A_1 = \frac{L_1/2 - V_2(1-\gamma)}{1-\gamma} \tag{4.11a}$$

$$A_2 = L_1/(2\gamma) - V_2 \tag{4.11b}$$

Then, the initial sinusoidal velocity profiles are created:

$$V_3(t_3) = A_1 \sin\left(\frac{4\pi t_3}{2(1-\gamma)} + \theta_3 - \pi/2\right) + A_1 + V_2 \tag{4.12a}$$

$$V_4(t_4) = A_2 \sin\left(\frac{4\pi t_4}{2\gamma} + \theta_3 - \pi/2\right) + A_2 + V_2 \tag{4.12b}$$

$$0 \le t_3 \le 1-\gamma, \qquad 0 \le t_4 \le \gamma$$

These two velocity profiles are then appended and shifted circularly based on the value of S, dictating which parts of the trajectory are sped up; however, appending the two trajectories introduces a discontinuity, often in slope. To address this, a bezier curve fit is used to smooth the discontinuity. Then, the amplitude of the velocity profiles are iterated until the velocity profile is smooth and integrates to the correct distance. From the final velocity profile and the known arc length of the trajectory, a list of the x-y-z locations on a sphere of radius 1 with a constant time step are computed by integrating the velocity profile and progressively tracing along the trajectory's arc length.

Fifth, after the x-y-z locations are computed at equally spaced locations in time, the angle of attack at these locations is computed for each half of the trajectory.

$$\theta_5(t_5) = \begin{cases} -\chi \tanh[K_v \sin(\pi t_5(1+\gamma) + \beta + \xi_1)]/\tanh(K_v) & \text{if } K_v > 0 \\ -\chi \sin[\pi t_5(1+\gamma) + \beta + \xi_1] & \text{if } K_v = 0 \end{cases} \tag{4.13}$$

$$\theta_6(t_6) = \begin{cases} \chi \tanh[K_v \sin(\pi t_6(1+\gamma)/\gamma + \beta + \xi_2)]/\tanh(K_v) & \text{if } K_v > 0 \\ \chi \sin[\pi t_6(1+\gamma)/\gamma + \beta + \xi_2] & \text{if } K_v = 0 \end{cases} \tag{4.14}$$

Here, $0 \le t_5 \le \gamma/(1+\gamma)$, the phase shift $\xi_1 = \pi/2$ if $S = 2$ or 4, otherwise $\xi_1 = 0$, $0 \le t_6 \le 1/(1+\gamma)$, and the phase shift ξ_2 for θ_6 is calculated based on the final value of θ_5 so that θ_5 and θ_6 are easily appended. Next, $\theta_5(t)$ and $\theta_6(t)$ are appended and smoothed using a bezier curve fit to obtain the angle of attack $\alpha(t)$. Afterwards 90° is added to $\alpha(t)$ so that the fin will oscillate between 90° ± χ (It should be noted that in the current SPM system, the fin is mounted at a 30° angle so this is subtracted from $\alpha(t)$ to obtain the correct motion.)

Sixth, with $x_4(t)$, $y_4(t)$, $z_4(t)$, and $\alpha(t)$ computed, the rotation matrix relative to a stationary frame for every point in time is calculated using the x, y, and z axes of the fin in the rotated frame. The z-axis is a vector from the origin to the x-y-z position along the trajectory and is expressed as

$$\overline{\mathbf{Z}}(t) = \begin{bmatrix} x_4(t) \\ y_4(t) \\ z_4(t) \end{bmatrix} \tag{4.15}$$

The x-axis points along the flat surface of the fin and is computed using:

$$\overline{\mathbf{X}}(t) = \overline{\mathbf{Z}}(t) \times \left(\overline{\mathbf{Z}}(t) \times \begin{bmatrix} \cos(\alpha(t)) \\ \sin(\alpha(t)) \\ 0 \end{bmatrix} \right) \tag{4.16}$$

With $\overline{\mathbf{X}}(t)$ and $\overline{\mathbf{Z}}(t)$, the y-axis is computed using

$$\overline{\mathbf{Y}}(t) = \overline{\mathbf{Z}}(t) \times \overline{\mathbf{X}}(t), \tag{4.17}$$

at which point the rotation matrix, $\mathfrak{R}$, is assembled.

$$\mathfrak{R} = \begin{bmatrix} | & | & | \\ \overline{\mathbf{X}} & \overline{\mathbf{Y}} & \overline{\mathbf{Z}} \\ | & | & | \end{bmatrix} = \begin{bmatrix} \mathfrak{R}_{11} & \mathfrak{R}_{12} & \mathfrak{R}_{13} \\ \mathfrak{R}_{21} & \mathfrak{R}_{22} & \mathfrak{R}_{23} \\ \mathfrak{R}_{31} & \mathfrak{R}_{32} & \mathfrak{R}_{33} \end{bmatrix} \tag{4.18}$$

Finally, these rotation matrices are converted into tait-bryan angles (Z-Y-X fixed angles) using:

$$\beta_1 = \arctan \left[\frac{\mathfrak{R}_{13}}{\sqrt{\mathfrak{R}_{11}^2 + \mathfrak{R}_{12}^2}} \right], \tag{4.19a}$$

$$\alpha_1 = \arctan[-\mathfrak{R}_{12}/\mathfrak{R}_{11}], \tag{4.19b}$$

$$\gamma_1 = \arctan[-\mathfrak{R}_{23}/\mathfrak{R}_{33}], \tag{4.19c}$$

which are interpreted and executed by the SPM. The time vector spans from 0 to 1 with a constant Δt. The list of tait-bryan angles and the non-dimensional time vector are scaled based on the frequency input into the SPM control software.

Trajectory Execution

The three-dimensional trajectories are executed using a SPM from hepia [49, 50], shown in figure 4.6, provided with an executable control interface and software

Figure 4.6: Image of the SPM used to execute the generated trajectories with an example wing mounted. The SPM is inverted and suspended over an oil tunnel during data acquisition.

[76, 77], which can actuate an arbitrary motion in a ± 50° cone accurate to within 1°. (It should be noted that a bird flaps its wings within a much larger cone; therefore some trajectories found in nature cannot be mimicked by the SPM which restricts the allowed optimum. Furthermore, the accuracy of the motor is reported as the maximum error between the desired and the observed tait-bryan angles.) The SPM is driven by three Kollmorgen AKD series ethercat drives, model number P01207, and can run certain trajectories at up to 4 Hz. The robot is programmed to read a list of tait-bryan angles for a single cycle with a non-dimensional time vector that starts at zero and ends at one. The tait-bryan angles are converted inside the software into quaternions and a spherical spline quaternion interpolation, commonly known as *squad*, generates the path to traverse. With the trajectory for a single period generated, the robot can loop through this trajectory periodically ad-infinitum. While traversing through the periodic trajectory, the path between the current and the sequential set-point is updated every 4 ms.

The fin is a rapidly prototyped 3 mm thick rigid flat plate with a tapered edge, dimensioned in figure 4.7. The rectangular portion of the flat plate has an aspect ratio of 1 while the taper is designed to converge to the thinnest point after a distance equal to one half of the height of the fin. The thickness of the arm is selected for structural stability and the length of the arm is selected to keep the flat portion of

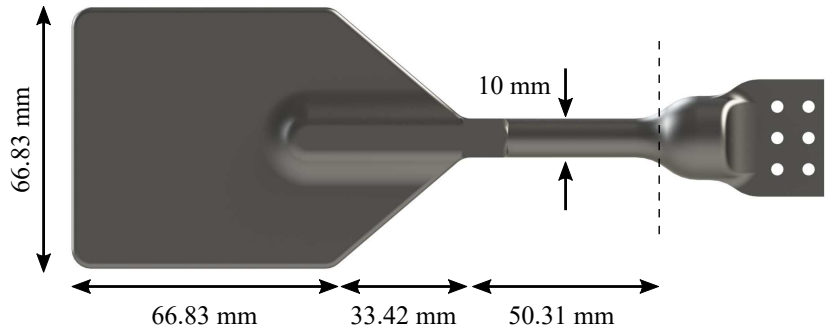

Figure 4.7: Dimensioned Solidworks render of the aspect ratio 1 test plate. The dashed line indicates the location where the plate is submerged when mounted vertically.

the fin far from the free surface, indicated by the dashed line in figure 4.7, but not so far as to generate moments that would damage the transducer. When mounted to the SPM, the tip of the fin is 0.212 m from the center of rotation and is submerged 0.151 m into the working fluid. The length of the fin that is submerged into the fluid when completely vertical, L_{fin}, is used as the characteristic length scale. When submerged, the fin has a planform area, A_{fin}, of $6.25 \times 10^{-3}\,\mathrm{m}^2$. The trajectories are executed in an oil tunnel with a test section that is 50 cm x 50 cm x 150 cm, although no co-flow is used in this study. Considering the size of the test section area, the SPM only executes about 10 trajectories to avoid recirculation effects. The tank is filled with approximately $1.2\,\mathrm{m}^3$ of Chevron Superla White Oil #5 which has a density, ρ, of $835\,\mathrm{kg\,m}^3$ and a kinematic viscosity, ν, of $1.6 \times 10^{-5}\,\mathrm{m}^2\,\mathrm{s}^{-1}$. Oil is used as the working fluid for this study to increase the magnitude of the generated forces so that they are more easily measurable compared with those in water or air. Images of the SPM mounted over the oil tunnel are shown in figure 4.8

Optimizaiton Loop and Data Acquisition

The optimization algorithm used is the CMA-ES coded in Matlab and implemented as follows. First, a set of trajectories for a single generation are created based on the 9 parameters listed in table 4.1 and converted into a list of sequential tait-bryan angles dictating the path of the fin to be executed by the SPM. Next, the trajectories are executed by the SPM, during which the forces and the torques on the fin and the position of the fin are recorded. The forces and torques are acquired with an ATI Nano 17 sampled at 250 Hz and recorded with a National Instruments USB 6211 DAQ board. The ATI Nano 17 has a maximum capacity of 25 N in the x

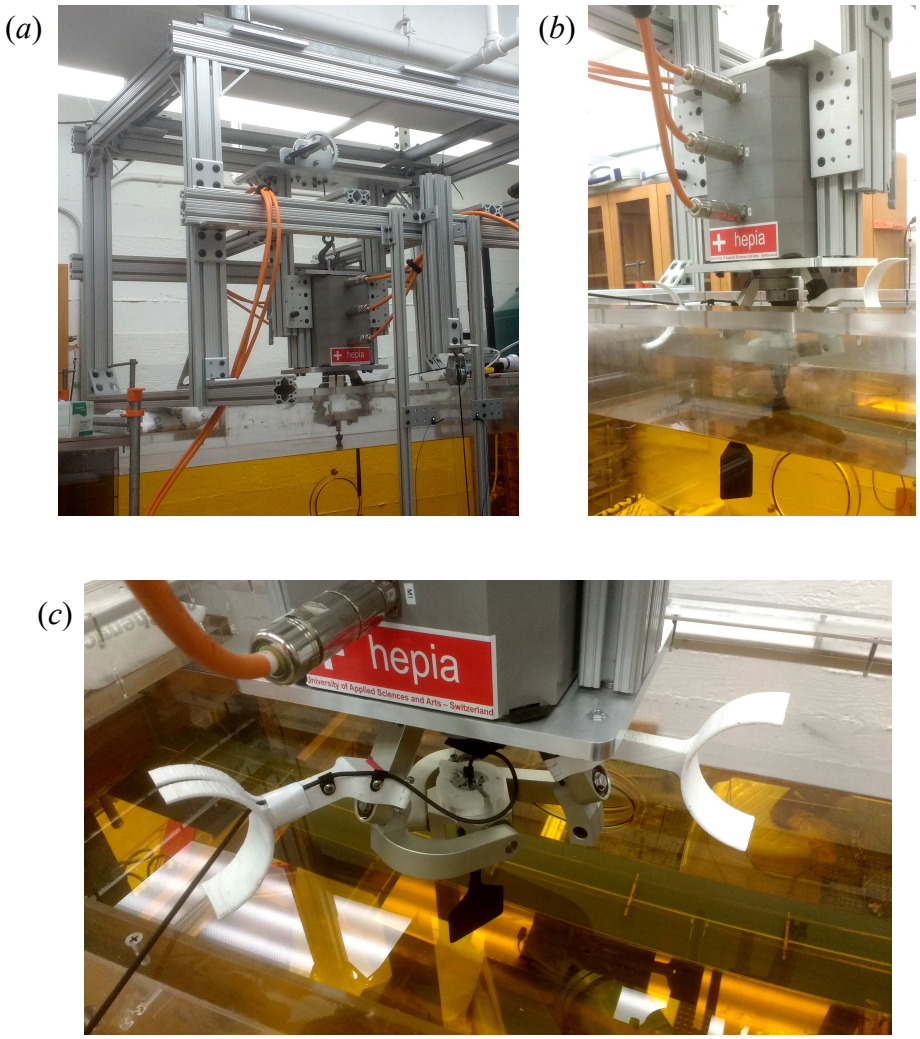

Figure 4.8: Images of the SPM mounted over the oil tunnel during data acquisition. The crank shaft at the top of (a) is used to adjust the submerged depth of the fin. The white arms attached to the SPM in (c) keep the wire of the transducer from getting tangled during trajectory execution.

and y-directions, 35 N in the z-direction, and 250 N mm in all directions. The ATI Nano 17 has a resolution of 6.25 mN and 31.25 mN mm and is mounted at the fixed point of rotation. The weight of the fin, taking into account buoyancy, is subtracted off during post-processing. The position of the fin is sampled at 250 Hz from Kollmorgen Workbench interfaced with LabView. Three trials are conducted for each trajectory and the resulting forces and torques per cycle are then phase averaged and ensemble averaged. Afterwards, an average force per cycle in the x, y, z, and normal directions ($\overline{F}_x$, $\overline{F}_y$, $\overline{F}_z$, and $\overline{|F_n|}$, respectively) are computed. The instantaneous forces are denoted without an overline. These overall values are then given a score based upon the following fitness function:

$$fit = w\ F_r + (1 - w)\ \eta_r \tag{4.20}$$

Here, the force ratio, $F_r = |F_{target} - F_{exp}|/F_{target}$, and the efficiency ratio, $\eta_r = |\eta_{target} - \eta_{exp}|/\eta_{target}$, are the primary criterion for success, where the subscripts 'target' and 'exp' denote the target set-point and the experimentally obtained average value per cycle. For all searches, η_{target} is set to 1, F_{target} is allowed to vary depending on the goal of the particular test, and the relative weighting value, w, is set to 0.8 unless stated otherwise.

After all trajectories for a single generation are given a fitness value, the CMA-ES generates a new set of trajectories to be tested. This cycle continues until the optimization algorithm converges, defined as when the range of each parameter falls below that defined in table 4.2. The interfacing between Matlab, LabView, and the SPM control software occurs through a custom Sikuli script, which automates keyboard and mouse inputs, allowing the optimization to run continuously without human intervention. Within this chapter, the optimal trajectory is defined as the best trajectory during the final generation when the optimization converges. The best case across all of the generations is not defined as the optimal trajectory because this case is sensitive to noise.

4.3 Results and discussion

Optimized side-force

The search is first run to determine the optimal set of parameters to generate a side-force for use similar to that of a fish's pectoral fin for MPF locomotion. The side-force is defined as $F_{exp} \equiv \overline{F}_m = (\overline{F}_x^2 + \overline{F}_y^2)^{1/2}$ and points in the direction $\theta_m = \arctan(\overline{F}_y/\overline{F}_x)$. The efficiency is then defined as $\eta_{exp} \equiv \eta = \overline{F}_m/\overline{|F_n|}$. The direction is allowed to be arbitrary as the trajectory can be rotated such that the

Parameter	Symbol	Min. Range
Stroke angle	ϕ	3°
Deviation angle	ψ	3°
Rotation angle	χ	3°
Rotation phase	β	0.4
Speed code	S	1
Speed up value	γ	0.1
Rotation acceleration	K_v	0.2
Stroke deviation	λ	0.2
Frequency	f	0.01 Hz

Table 4.2: Convergence criteria for trajectory parameters.

side-force is aligned with the desired direction of motion if implemented. For this optimization, all parameters are simultaneously adjusted within the bounds shown in table 4.1 using the fit function:

$$fit = \begin{cases} 0.75\ F_r + 1 & \text{if } F_r > 0.15 \\ 0.75\ F_r + 0.25\ \eta_r & \text{if } F_r \leq 0.15 \end{cases} \tag{4.21}$$

This variation on the fit function is used to ensure that the optimal trajectory matches the desired side-force set-point within 15% by heavily penalizing any trajectory that generates a side-force outside of this band. Although unlikely, there is a possibility that the optimization could disregard F_r and only minimize η_r if this would provide a lower overall fit value. In later optimization searches, this is found to be unnecessary as weighting F_r and η_r is sufficient to ensure that minimizing F_r is a greater priority. The side-force set-point used is 17 mN, arbitrarily selected after confirming that a typical trajectory with parameters near the middle of the variable space could generate this amount of side-force. By selecting a set-point in this manner, the search can match the set-point exactly and has the flexibility to modify the parameters for maximum efficiency.

The optimization converges after 104 generations, although after generation 80, the span of the fitness values decreases significantly. The fit value of every trajectory tested across all of the generations is shown in figure 4.9. It should be noted that the significant gap in fitness values is from imposing that F_r be less than 0.15 and heavily penalized otherwise. Although this requirement is strict, trajectories at later generations meet this requirement, illustrating good convergence behavior. The convergence behavior of the parameters are shown in figures 4.10(a-i). The

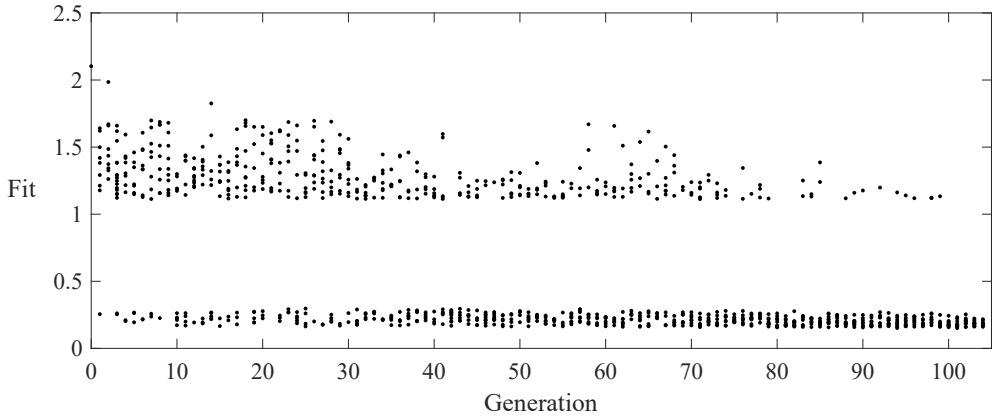

Figure 4.9: Fitness values for all of the trajectories for every generation, illustrating convergence towards an optimal trajectory for generating side-forces. It should be noted that the few values over 2.5 are not shown. These outliers are caused by noise which did not affect the overall convergence behavior.

parameters are non-dimensionalized as:

$$\zeta^* = \frac{\zeta - \min \zeta}{\max \zeta - \min \zeta} \tag{4.22}$$

where ζ represents a generic parameter. Throughout this chapter an asterisk $\{^*\}$ denotes a non-dimensional value. The convergence behavior of the experimentally obtained forces and efficiencies are shown in figures 4.10(j-l). These values are non-dimensionalized by a single arbitrary value to illustrate the convergence behavior of the dimensioned value and for ease of plotting. A non-dimensionalization of this form is indicated by two asterisks $\{^{**}\}$. It should be noted that the dashed line in figure 4.10(j) illustrates the side-force set-point that the optimization is given to match; however, the optimization converges to the set-point so quickly, making this line difficult to discern. Figure 4.10 demonstrates good convergence behavior of all parameters and forces because the dotted lines, corresponding to the minimum and maximum values during a single generation, narrow as the generations progress and because the optimal parameters avoid the allowed maximum value of the parameter space once the search has converged.

By observing the trends in the parameters across the generations, insight into how each parameter impacts the overall result can be obtained. Parameters λ, K_v, S, and γ are quickly determined to be of minimal importance as many of these values tend towards the minimum allowed value within approximately 25 generates and some almost immediately. It is worth noting that although a figure-eight trajectory

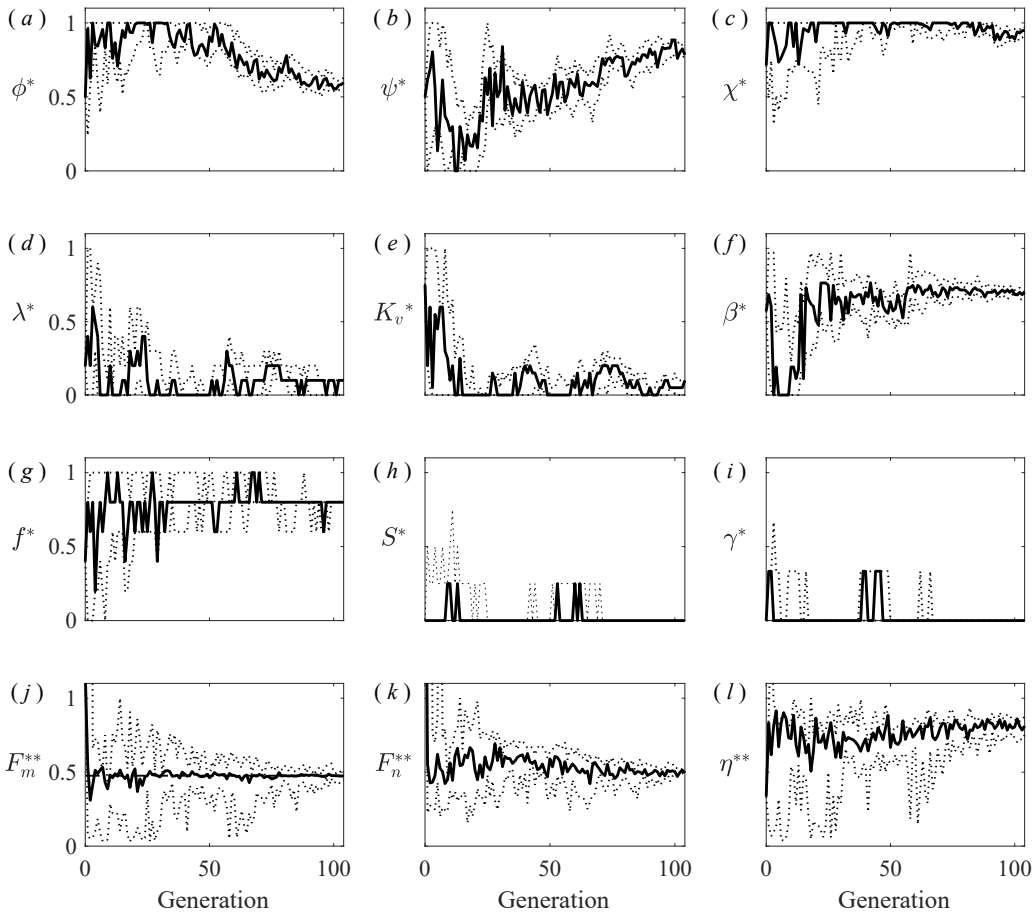

Figure 4.10: Convergence of the non-dimensional parameters (a-i), forces (j,k) and efficiencies (l) across all generations for generating side-force. The solid line corresponds to the value of the parameter which produces the best fit value while the dotted lines correspond to the minimum and maximum values of the parameter during that generation.

is allowed, the optimization did not select them after a few generations. The best trajectory of each generation converges to the side-force set-point almost immediately. The parameter adjustments during the following generations primarily modify the normal force and by relation the efficiency. Parameters ϕ and ψ, dictating the overall shape of the trajectory, are adjusted most frequently throughout the search, illustrating their impact. The overall trajectory started off with a large ϕ and a small ψ, which corresponds to a long thin ellipse, but slowly expands into a short wide ellipse as the generations pass. The rotation angle χ is identified immediately as important and remains near the maximum allowed value for almost all of the generations. It should be noted that these results suggest that a diverse family of trajectories exist which could be considered optimal. This is because during almost all of the generations, trajectories are found which match the side-force set-point with comparable efficiencies. Another criterion, in addition to a force set-point and a maximum efficiency, would be necessary to distinguish between this family of trajectories.

Highlights of the progression of the overall trajectory with their corresponding $F_x^{*\prime}$ and $F_y^{*\prime}$ as a function of the non-dimensional time $t^* = ft$ over many generations is shown in figure 4.11. The forces are non-dimensionalized as:

$$\{F_x^{*\prime}, F_x^{*\prime}\} = \frac{\{F_x', F_y'\}}{1/2\ \rho U_{tip}^2 A_{fin}} \tag{4.23}$$

where U_{tip} is the average velocity of the tip of the fin, calculated from the arc length traversed by the tip and the frequency of the cycle. The trajectory and the forces are rotated such that the vector sum of the average forces per cycle in the x and y-directions aligns with the positive y-direction relative to the orientation in figure 4.1. The variables F_x' and F_y' correspond to the instantaneous forces in the x and y-directions after this rotation. For the remainder of this chapter, a prime symbol, $\{'\}$, corresponds to forces that have been rotated. Even as early as generation 5, the optimization had already found a trajectory which reasonably matches the desired side-force set-point. As the generations pass, the overall trajectory changes significantly. At first, the trajectory is flat in generation 5, and although the trajectory in generation 6 qualitatively resembles that in generation 79, the rotation timing is different. It should be noted that the fin is almost normal to the path of motion in generation 79 during the downward stroke compared with the fin in generation 6, which is angled relative to the path of motion. Nearly flat symmetric trajectories are explored as well, exhibited by the optimal trajectory for generation 16; however,

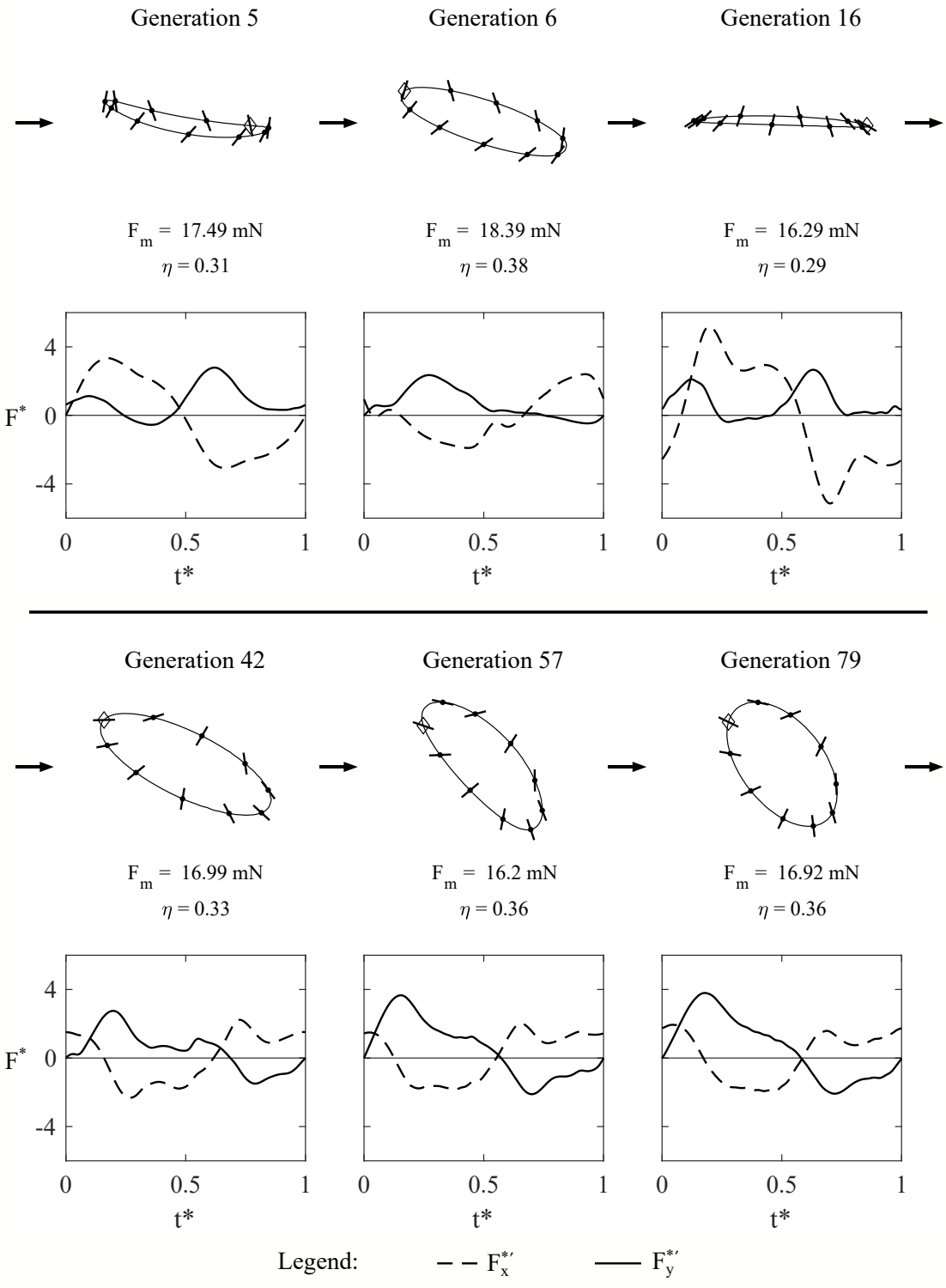

Figure 4.11: Optimal trajectories for generating side-force with the corresponding F_m, η, $F_x^{*\prime}$ and $F_y^{*\prime}$ below each trajectory for select generations, illustrating the qualitative trajectory evolution as generations pass.

this trajectory results in a lower efficiency compared with that of the previous generations. After generation 42, the trajectories are qualitatively similar. The only difference between the optimal trajectory of generation 42 and those afterwards is the overall angle of the trajectory and subtle changes to the overall shape and the rotation timing. These changes provide small improvements to either better match the side-force set-point or to improve the efficiency. By generation 79, the optimization had found a trajectory which shows good agreement with the side-force set-point and with good efficiency. After generation 79, only subtle modifications are made to the parameters as the trajectory progresses towards the optimal trajectory.

Parameter	Symbol	Optimal Value
Stroke angle	ϕ	27.9°
Deviation angle	ψ	15.7°
Rotation angle	χ	63°
Rotation phase	β	4.4
Speed code	S	0
Speed up value	γ	1
Rotation acceleration	K_v	0.2
Stroke deviation	λ	0.1
Frequency	f	0.19 Hz
Force magnitude	F_m	16.95 mN
Efficiency	η	0.364
fit	-	0.161

Table 4.3: Optimal parameters for generating side-force.

The rotated optimal trajectory for generating side-forces is shown in figures 4.12(a,b) and the corresponding non-dimensional forces as a function of t^* are shown in figure 4.12(c). The optimal set of variables is given in table 4.3. From the overall path and the rotation timing of the fin, the optimized trajectory exhibits a 'rowing' behavior. During the half of the stroke shown in figure 4.12(a), the fin is nearly normal to the path of motion, which exhibits qualities similar to a power stroke in drag-based propulsion, while during the half of the stroke shown in figure 4.12(b), the fin attempts to be nearly aligned with the path of motion, which exhibits qualities similar to a recovery stroke. Analysis of $F_y^{*\prime}$ illustrates this behavior as well since 61% of the cycle generates a large positive force compared with the remaining 39% of the cycle which generates a smaller negative force. The normal force makes up

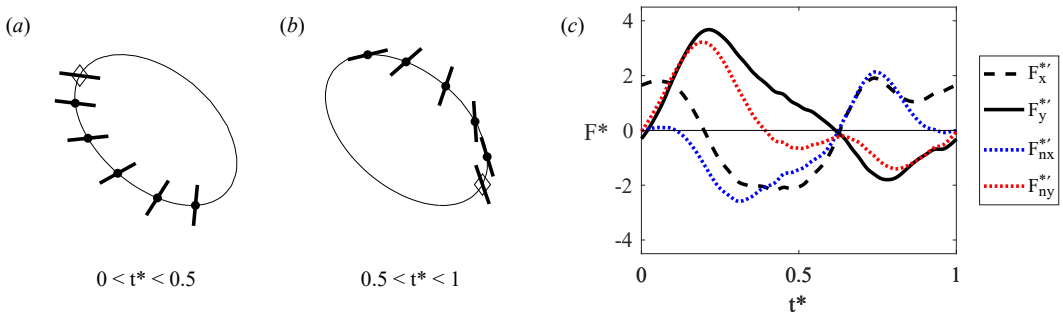

Figure 4.12: The forward stroke (a) and the backward stroke (b) of the rotated optimal trajectory for generating side-force. The trajectory is rotated such that the vector sum of the forces in the x and y-directions aligns with the positive y-direction relative to the orientation in figure 4.1. The corresponding $F_x^{*\prime}$, $F_y^{*\prime}$, $F_{nx}^{*\prime}$, and $F_{ny}^{*\prime}$ (c) show the instantaneous phase averaged forces over a single cycle as a function of t^*.

47.8% of $F_x^{*\prime}$ and 56.0% of $F_y^{*\prime}$, computed from:

$$\Delta_{nx} \equiv 1 - \frac{\int_0^1 |F_{nx}^{*\prime} - F_x^{*\prime}|\, dt^*}{\int_0^1 |F_x^{*\prime}|\, dt^*}, \tag{4.24}$$

$$\Delta_{ny} \equiv 1 - \frac{\int_0^1 |F_{ny}^{*\prime} - F_y^{*\prime}|\, dt^*}{\int_0^1 |F_y^{*\prime}|\, dt^*}. \tag{4.25}$$

Here, $F_{nx}^{*\prime}$ and $F_{ny}^{*\prime}$ are the components of the normal force in the rotated x and y-directions. This suggests that the majority of the sides forces can be attributed to the normal force and probably accounts for the trajectory's efficiency of 0.36. Qualitatively, the reason that the efficiency is not larger, considering how well correlated $F_y^{*\prime}$ and $F_{ny}^{*\prime}$ are in figure 4.12(c), can be understood by considering the downward stroke and the upward stroke independently. During the downward stroke, useful force is generated, and because this force primarily comes from F_n^*, η for this portion of the cycle is large; however, during the upward stroke, although $F_y^{*\prime}$ is still nearly aligned with $F_{ny}^{*\prime}$, $F_y^{*\prime}$ is negative and therefore does not contribute useful forces. This means that F_n^* is not taken advantage of in a useful way. The alignment of $F_y^{*\prime}$ and $F_{ny}^{*\prime}$ in the selected optimal trajectory is reasonable because of the nature of the given fitness function. The criterion for success is having a large η, which is defined as the ratio of F_y' to F_n; therefore, it is reasonable that an optimal trajectory would try to align the two components. The Reynolds number, $Re = U_{tip}L_{fin}/\nu$, for the optimal trajectory is 901.5.

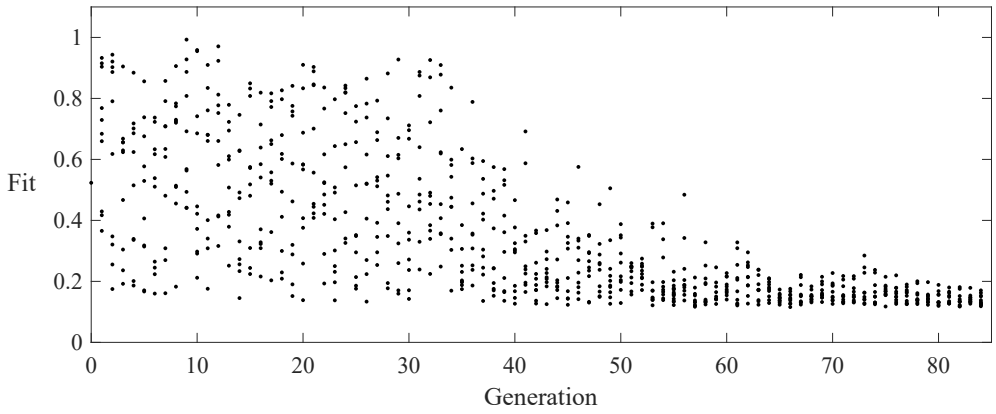

Figure 4.13: Fitness values for all of the trajectories for every generation, illustrating convergence towards an optimal trajectory for generating side-forces when the trajectory is constrained to a line.

Optimized side-force limited to a line

The results of the first optimization suggested that a family of trajectories exist which could match the side-force set-point and have comparable efficiences to the selected optimal trajectory. Due to the simplicity of implementing a two-dimensional trajectory on an AUV compared with a three-dimensional trajectory, the effect of three-dimensionality is explored. Furthermore, previous studies had shown that stroke deviation tends to primarily decrease efficiency [52]. For the second optimization, the same side-force set-point of 17 mN is used, but for this optimization, the trajectory is limited to a straight line within the x-y plane. To implement this modification, ψ and λ are set to zero for every trajectory.

The second optimization converges after 84 generations and shows a significant decrease in the range of the fitness values after generation 64. The fitness value of every trajectory is shown in figure 4.13. The convergence behavior of the parameters are shown in figures 4.14(a-i). The convergence behavior of the experimentally obtained forces and efficiencies are shown in figures 4.14(j-l). Figure 4.14 also demonstrates good convergence behavior of all parameters because the range of the variables narrows as the generations progress and because the optimal parameters avoid the allowed maximum value of the parameter space. Although the range of the forces and efficiencies start out large, the range narrows significantly in the last 20 generations. Regarding the general behavior of the parameters, K_v is quickly set to the minimum allowed value. Before approximately generation 40, there is a significant variation in ψ, χ, β, S, γ, and f, but afterwards only small adjustments

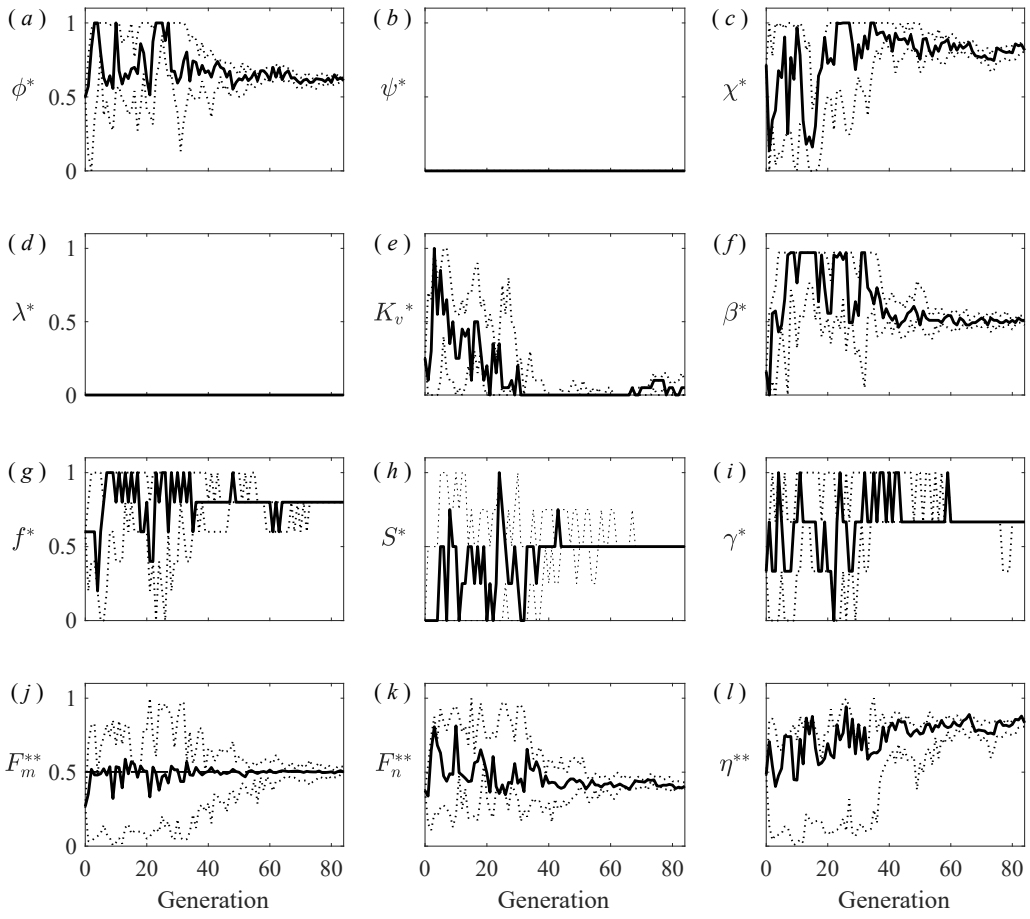

Figure 4.14: Convergence of the non-dimensional parameters (a-i), forces (j,k) and efficiencies (l) across all generations for generating side-force when the trajectory is constrained to a line. The solid line corresponds to the value of the parameter which produces the best fit value while the dotted lines correspond to the minimum and maximum values of the parameter during that generation.

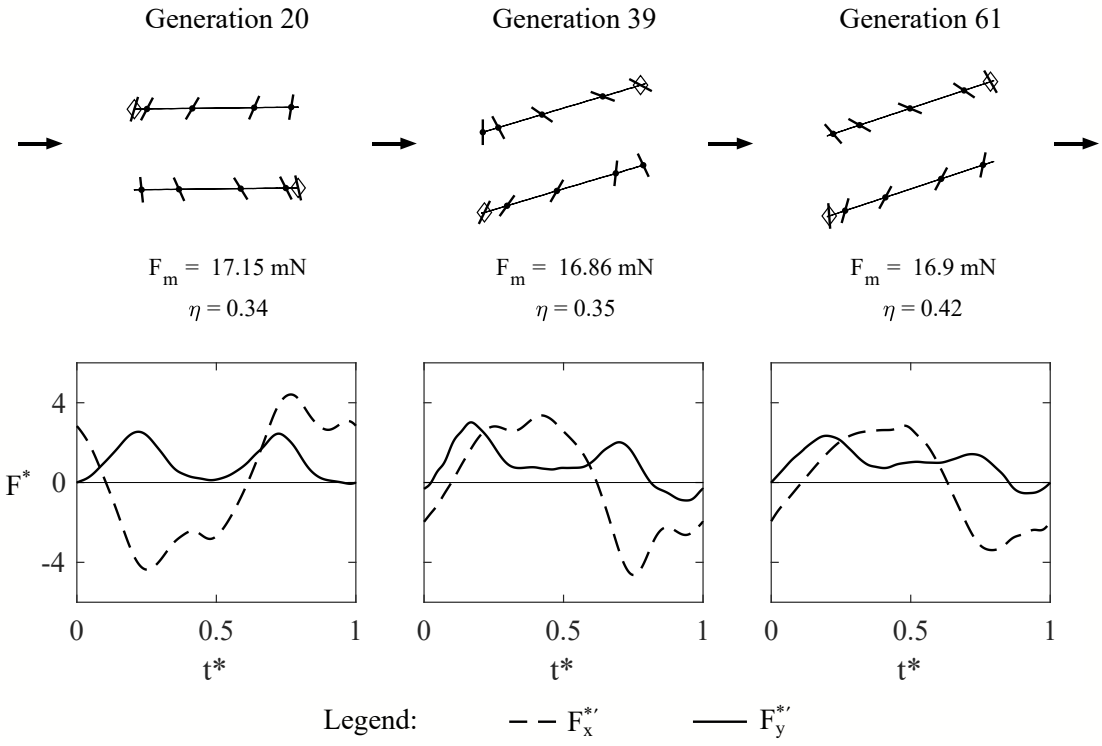

Figure 4.15: Optimal trajectories for generating side-force when the trajectory is constrained to a line with the corresponding F_m, η, $F_x^{*\prime}$ and $F_y^{*\prime}$ below each trajectory for select generations, illustrating the qualitative trajectory evolution as generations pass.

are made. Also, χ tends to remain close to the minimum or maximum allowed value of $\pm 70^\circ$ illustrating its importance. Again, the optimization finds trajectories which match the side-force set-point almost immediately and most of the adjustments at later generations are made to minimize F_n and by relation maximize η.

Highlights of the progression of the overall trajectories limited to a line with their corresponding $F_x^{*\prime}$ and $F_y^{*\prime}$ as a function of t^* over many generations is shown in figure 4.15. The trajectories explored during the earlier generations are largely symmetric, illustrated by the optimal trajectory for generation 20, and generate a net force nearly perpendicular to the path of motion. This type of trajectory is similar to that typically used by birds during hovering. The symmetry of the motion is mimicked by a similar symmetry in $F_y^{*\prime}$ during both halves of the cycle; however, as generations pass, the parameters are changed to angle the net force relative to the path of motion. This is illustrated by the optimal trajectories of generations 39 and 61. Although there are two distinct peaks in $F_y^{*\prime}$ for the trajectory in generation 39,

the peaks are more spread out than those in generation 20. By generation 61, the peaks are almost completely spread out, meaning that a positive $F_y^{*\prime}$ is generated for a greater portion of the cycle. After generation 61, only subtle modifications are made to the parameters as the trajectory progresses towards the optimal trajectory.

Parameter	Symbol	Optimal Value
Stroke angle	ϕ	28.3°
Deviation angle	ψ	0°
Rotation angle	χ	44.1°
Rotation phase	β	3.2
Speed code	S	2
Speed up value	γ	1.2
Rotation acceleration	K_v	0.1
Stroke deviation	λ	0
Frequency	f	0.19 Hz
Force magnitude	F_m	16.97 mN
Efficiency	η	0.413
fit	-	0.119

Table 4.4: Optimal parameters for generating side-force when the trajectory is constrained to a line.

The rotated optimal trajectory limited to a line for generating side-forces is shown in figures 4.16(a,b) and the corresponding non-dimensional forces as a function of t^* are shown in figure 4.16(c). It should be noted that an optimal value of $S = 2$ and $\gamma = 1.2$ means that one half of the cycle is sped up by 20%. The portion of the cycle that is sped up is composed of the second half of the trajectory in figure 4.16(a) and the first half of that in figure 4.16(b) which corresponds approximately to $0.27 < t^* < 0.73$. The optimal trajectory when the trajectory is limited to a line exhibits a different behavior compared with that when the trajectory is allowed to have a non-zero ψ. Here, there is no well defined 'power stroke' or 'recovery stroke' because the trajectory generates a positive $F_y^{*\prime}$ for 82% of the cycle. Compared with the previous optimal trajectory, $F_y^{*\prime}$ has a lower max amplitude but is significantly more spread out. Furthermore, for the optimal trajectory limited to a line, F_n^* tends to align better with $F_x^{*\prime}$ than $F_y^{*\prime}$. For this case, the normal force makes up 78.5% of $F_x^{*\prime}$ and 59.3% of $F_y^{*\prime}$, computed from (4.24) and (4.25). The efficiency of this optimal trajectory is 0.41, a little greater than that for the previous optimization, which may be related to the result that the normal force makes up more of $F_y^{*\prime}$ than in the previous optimization. It should be noted that during stroke reversal around $t^* = 0.5$, a positive $F_y^{*\prime}$ is generated. For this portion of the trajectory,

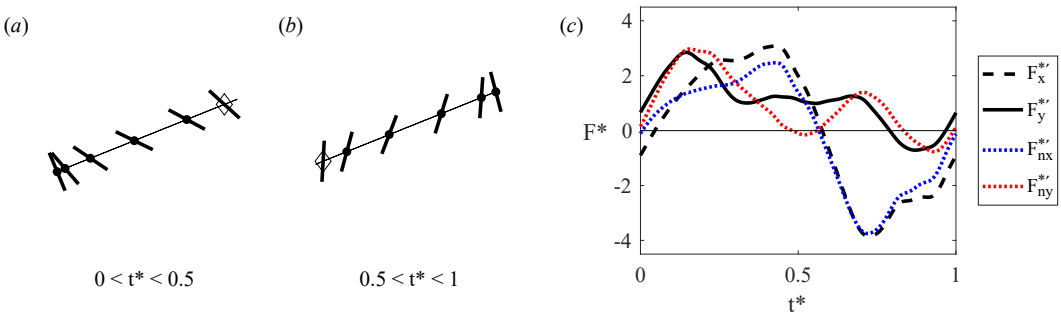

Figure 4.16: The forward stroke (a) and the backward stroke (b) of the rotated optimal trajectory for generating side-force when the trajectory is limited to a line. The trajectory is rotated such that the vector sum of the forces in the x and y-directions aligns with the positive y-direction relative to the orientation in figure 4.1. The corresponding $F_x^{*\prime}$, $F_y^{*\prime}$, $F_{nx}^{*\prime}$, and $F_{ny}^{*\prime}$ (c) show the instantaneous phase averaged forces over a single cycle as a function of t^*.

$F_y^{*\prime}$ does not originate from the normal force, which suggests that other unsteady mechanisms, potentially wake capture, are utilized. The wake capture argument is made by considering that the t^* when the trajectory is sped up corresponds to a near flat line of $F_y^{*\prime}$. A possible explanation for this behavior is that the increased velocity and acceleration of the fin during the latter half of the downward stroke generates a greater positive $F_y^{*\prime}$ and a greater flow velocity which the upward stroke moves into and redirects downwards, creating a positive $F_y^{*\prime}$; however, additional flow visualization is necessary to provide a more definitive answer. It should be noted that the optimal trajectory may be an artifact of the imposed constraints. Due to the limits to χ of $\pm 70°$, the fin is never able to align itself to the path of motion to minimize the normal force to have an 'optimal recovery stroke.' Due to fin being angled towards the incoming flow throughout the cycle, which would redirect flow downwards, the fact that the fin maintains a positive $F_y^{*\prime}$ for the majority of the cycle, even during the second half of the cycle when the fin moves upwards, is reasonable. The selected optimal trajectory reveals an adaption to the imposed constraints at a Re of 742.4 and provides a small improvement over the efficiency of the optimal trajectory found in the previous search. This shows the potential viability in simplifying the trajectory to a line which is easier to implement.

Optimized thrust

Besides potential applications of the SPM as a pectoral fin, the SPM can also be used similar to that of a fish's caudal fin for BCF locomotion; therefore an optimization is conducted with the same set-point of 17 mN but applied to thrust. For this case,

$F_{exp} \equiv \overline{F}_z$ and $\eta_{exp} \equiv \eta = \overline{F}_z/\overline{|F_n|}$. To implement this modification, all parameters are set to zero for every trajectory except for ϕ and f which are allowed to vary. It should be noted that for this optimization, the maximum allowed value for f is changed to 0.4 Hz because preliminary testing showed that trajectories below 0.2 Hz are incapable of generating positive thrust. Due to the limited number of variables for this optimization, allowing for significantly faster convergence times, a study regarding the sensitivity of the optimal trajectory to the relative weighting parameter, w, in the fitness function is conducted. The optimization is conducted using a w of 0.6, 0.7, and 0.8. It should be noted that because the z-axis points out of the page in figure 4.1, a useful thrust would correspond to a negative F_z; therefore, F_z is non-dimensionalized as:

$$F_z^* = \frac{-F_z}{1/2\ \rho U_{tip}^2 A_{fin}}. \tag{4.26}$$

Due to the minimal number of parameters used, all of the optimization searches converge within 15 generations. The fitness values of every trajectory to optimize thrust are shown in figures 4.17(a-c). Figures 4.17(d-i), (j-l), and (m-o) illustrate good convergence behavior of the parameters, forces, and efficiencies, respectively, for different w. The optimal set of parameters found during each search is given in table 4.5. These parameters agree well across the three searches as the range is below that required for convergence (table 4.2). This shows that small changes in w will not significantly impact the overall trajectory. It should be noted though, that from the results in previous sections, there are many trajectories which could be considered better optimal solutions depending on how much priority is given to matching the force set-point. For example, although not shown, generation 49, during the optimization search when the trajectory is allowed to be arbitrary in three-dimensions, generates 17.36 mN of side-force with an efficiency of 0.41; however, this trajectory has a fitness score of 0.164, which is greater than the optimal trajectory which has a fitness score of 0.161, because of the difference between F_{target} and F_{exp}. If the application does not require the set-point to be met so accurately, the relative weighting between F_r and η_r should be adjusted so that this trajectory would receive a better fitness value.

As a reference, the F_z^* and the $|F_n^*|$ over a single cycle as a function of t^* for the three optimization searches are shown in figure 4.18. The behavior of the forces is as expected because as the fin begins its stroke, the fin generates positive thrust. This value then decreases near the end of each stroke as the fin decelerates and

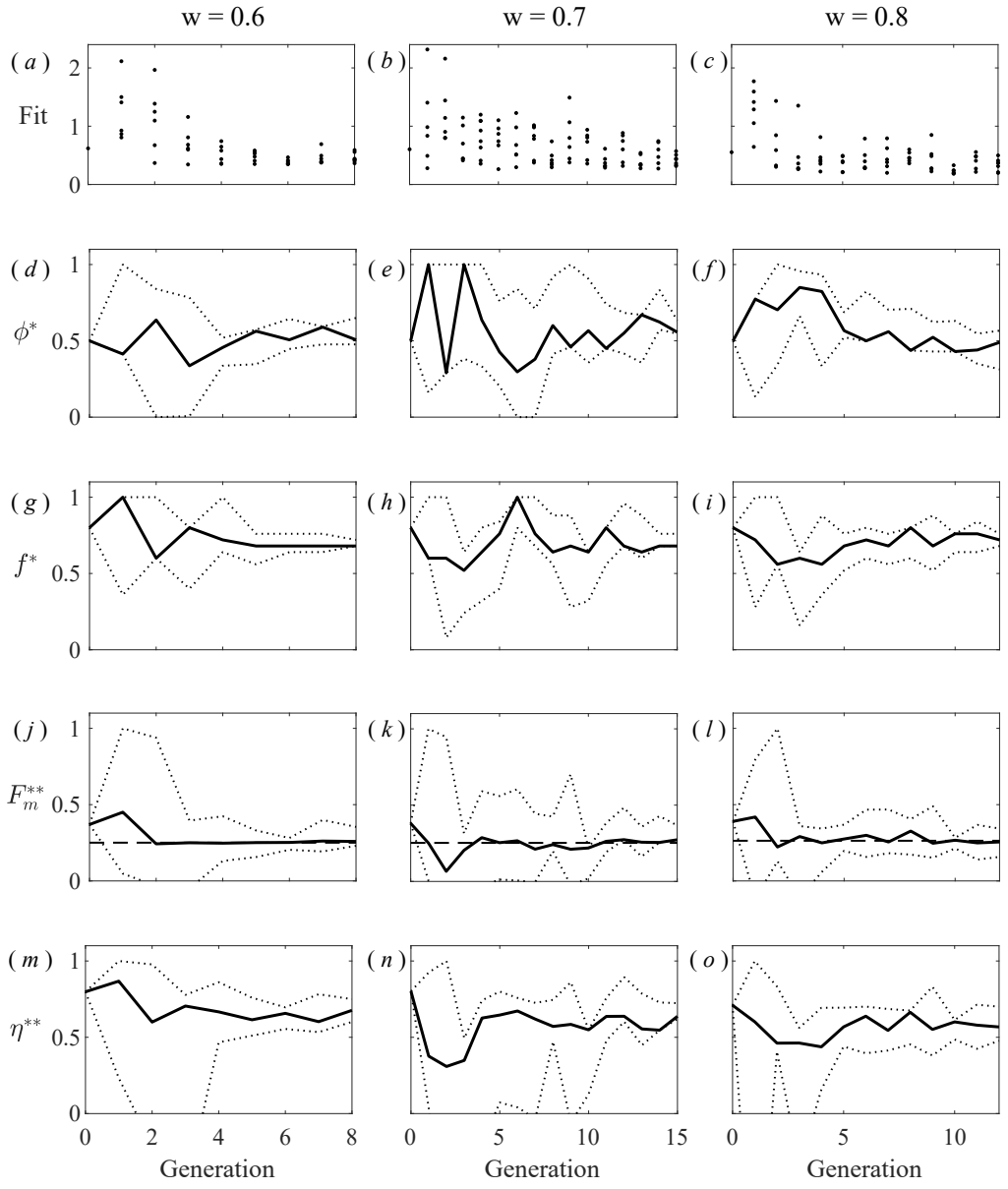

Figure 4.17: Fitness values (a-c) and convergence behavior of the non-dimensional parameters (d-i), forces (j-l) and efficiencies (m-o) across all generations for different w. Each column of plots corresponds to the results using the relative weighting listed on top of (a,b,c), respectively. The solid line corresponds to the value of the parameter which produces the best fit value while the dotted lines correspond to the minimum and maximum values of the parameter during that generation.

Parameter	Trial 1	Trial 2	Trial 3
w	0.6	0.7	0.8
ϕ	25.2°	26.7°	24.7°
f	0.32 Hz	0.32 Hz	0.33 Hz
F_m	17.55 mN	18.38 mN	16.49 mN
η	0.139	0.135	0.129

Table 4.5: Optimal parameters for generating thrust.

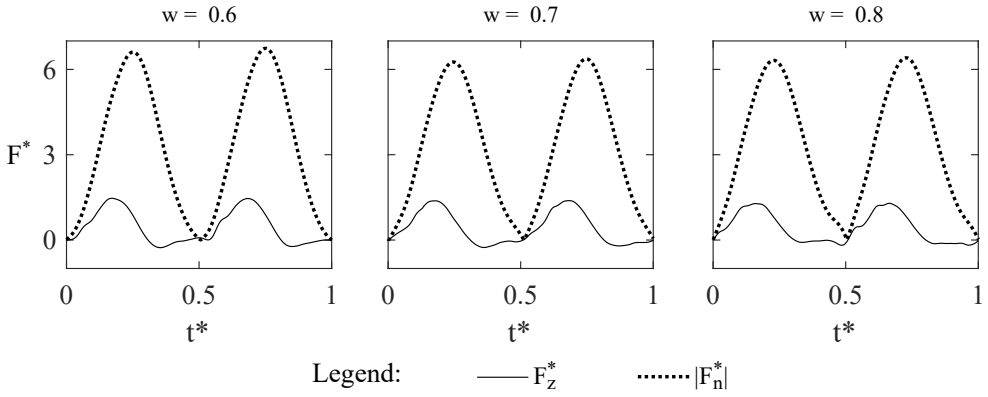

Figure 4.18: Instantaneous phase averaged forces F_z^* and $|F_n^*|$ as a function of t^* for a single cycle. At approximately $t^* = 0$, the fin is starting a stroke. The relative weighting, w, used to find each optimal trajectory is listed above each plot.

pushes fluid in the direction opposite that necessary to generate positive thrust. When comparing F_z^* to $|F_n^*|$ for the optimally selected trajectories, the amplitude of F_z^* is small compared with that of $|F_n^*|$ which accounts for their consistently low efficiency. The Re for the three trials are 1124, 1184, and 1125, respectively, which is low for efficient vortex-based propulsion, the mechanism used by fish that swim using BCF locomotion; therefore, the greater efficiency of the trajectories for generating side-force compared with those for generating thrust, even though they both have the same set-point, is reasonable because MPF locomotion typically has a greater effieincy than BCF locomotion at lower speeds [12].

4.4 Closing remarks

The potential of experimentally optimizing trajectories was demonstrated in multiple scenarios. For a variety of force set-points and constraints, trajectory optimization through CMA-ES was correctly able to determine trajectories that matched the desired set-point with good efficiency, despite the amount of complexity and non-linearity involved with the flow dynamics. All optimization trials followed the

general trend that the force set-point was matched within the first few generations and all following generations were used to modify the efficiency. Across the generations and in different optimization trials, the stroke angle and the deviation angle were modified the most, the rotation angle consistently approached the maximum or minimum allowed value, and most other parameters approached a steady value without much deviation. Although the general trajectory was shown to be relatively insensitive to small changes in the relative weighting of the force ratio and the efficiency ratio in the fitness function, more significant tuning can be implemented based on user needs. For example, if a degree of error in the force set-point is acceptable and an estimate of the optimal efficiency is known, the relative weighting can be adjusted to favor efficient trajectories with a greater error. Furthermore, the most complex optimization that involved 10 parameters was completed within 104 generations which is approximately 7 days of run time if the optimization is allowed to run without interruption. This convergence speed allows for a short turn around time for finding optimal trajectories and allows for the opportunity to compare different optimal trajectories.

The first two optimization searches involved optimizing side-force, similar to the method a fish's pectoral fin or a bird's wing would be used for propulsion. One of the trajectories was allowed to be arbitrary in three-dimensional space while the other was constrained to a line in the x-y plane. Interestingly, the two optimal trajectories appeared to utilize different strategies. The trajectory allowed to be arbitrary in three-dimensions generated most of its useful force during one half of the cycle while the trajectory constrained to a line generated an almost consistently positive useful force throughout the cycle. (Future studies through quantitative flow visualization are necessary to provide more definitive answers regarding the nature of the underlying propulsion mechanisms.) Furthermore, the trajectory constrained to a line performed comparably to the trajectory allowed to be arbitrary in three-dimensions, which shows viability in reducing the complexity of the trajectory if implemented on an underwater vehicle.

The final optimization searches involved optimizing thrust, similar to the method a fish's caudal fin would be used for propulsion. The optimal trajectory was found to have less efficiency than the optimal trajectories used to generate side-force at the same force set-point. This disparity in efficiency is likely due to MPF locomotion being more efficient than BCF locomotion at lower Reynolds numbers.

This optimization study shows promise for utilizing CMA-ES to experimentally

obtain optimal trajectories for implementation on an AUV. The convergence speed and the flexibility in the fitness function allows for a variety of 'optimal' trajectories to be defined based upon the desired application. After a library of trajectories is obtained for a variety of scenarios, these trajectories could have applications in vehicle control. Future studies involving how the working fluid, co-flow, flexibility, and axis of rotation affect the forces and efficiencies will help better map out the parameter space. Future studies involving quantitative three-dimensional flow visualization techniques will be necessary to provide a more definitive answer regarding the underlying optimal mechanisms used for propulsion.

Chapter 5

SUMMARY AND FUTURE WORK

The flapping motion is widely utilized in nature, from birds in the air to fish in the sea. Due to its prevalence and persistence over time, there is much to learn and many potential applications. Three specific studies surrounding flapping propulsion are conducted to provide insights into its underlying mechanisms and to develop potential applications to assist in the design and the development of underwater vehicles. All studies were primarily conducted in the absence of co-flow for simplicity and to investigate the infinite Strouhal number limit.

The first study involved a comparison between propulsion via flapping and via periodic contractions from fish and jellyfish, respectively. The two propulsion mechanisms were directly compared by simplifying the kinematics and manufacturing a mechanism that could operate in both modes of propulsion. The results showed that despite using rigid or flexible plates or modifying the duty cycle, flapping is the most efficient. Furthermore, modifying the duty cycle for clapping propulsion showed an improved thrust performance compared with flapping propulsion. Finally, the two propulsion mechanisms were shown to produce similar amounts of thrust per cycle when the kinematics are identical. This phenomenon was investigated through a vorticity analysis of the near wake during the first cycle. The analysis suggested that because the overall kinematics were the same, the vortices generated from both propulsion mechanisms were generated in similar locations, grew at similar rates, and moved in similar ways, which led to a similar thrust being generated. This study provides insights into the selection of a propulsion mechanism when designing an underwater vehicle. If a vehicle's objective is to operate with the greatest efficiency, the results suggest that flapping propulsion should be used. If a vehicle's objective is to operate with the greatest thrust, the results suggest that clapping propulsion should be used.

The first study raises many follow up questions and parameters to explore in the future. First, the impact of co-flow can be investigated more rigorously to determine how the thrust, efficiency, and vortex dynamics are modified for all of the test plates. This would provide greater insights into the underlying mechanisms and a more direct path to practical applications. Second, the results for clapping propulsion

demonstrated that its efficiency is significantly hindered by the opening motion. The primary reasoning for fully opening and closing the mechanism during the clapping motion was to keep the bounds of the motion the same. This need not be the case for practical applications if the goal is primarily to improve clapping propulsion. By exploring the closing distance, a significant improvement in clapping propulsion will likely be achieved. This is an optimization problem because not fully closing the plates will decrease the power needed during the opening motion at the cost of decreasing the thrust generated during the closing motion. Third, there were many distinct features in the instantaneous force data which could be directly correlated with changes in the vorticity field using higher resolution and higher fidelity DPIV. Fourth, computing the contribution of the added mass to both flapping and clapping propulsions would provide insights into how much the added mass terms contribute to the overall forces. Finally, all tests were conducted using plates which would generate approximately two-dimensional flow; however, all practical applications operate in highly three-dimensional flows. This can be investigated more rigorously by studying the impact of aspect ratio and plate geometry on the resulting thrust, efficiency, and vortex dynamics.

The second study involved the characterization of a novel geometry inspired by the chord-wise bending of a fish's caudal fin during locomotion. An experimental setup was designed to test the impact of chord-wise curvature on a variety of static and actuated plates. Testing using rigid curved plates with a smaller planform area than that of a baseline flat plate, used to emulate physically curving the free tips towards each other seen in fish, suggested that increasing the curvature decreases the side-force, thrust, and required torque with a minimal effect on efficiency. This result was utilized to develop an actuated plate using nitinol wire which could curve on-demand for any desired duration, which has applications to modulate the forward velocity or assist in turning maneuvers of an underwater vehicle. Testing using rigid curved plates with an identical planform area to that of a baseline flat plate showed that during the stroke when fluid flows into the concave geometry, the thrust generated increases. This result was utilized to develop a passive snap-buckling plate which would present a concave geometry into the flow throughout the cycle. The snap-buckling plate demonstrated superior thrust and efficiency compared with the baseline flat plate and has applications as an improvement compared with a rigid flat propulsor.

The second study raises follow up questions primarily regarding flexibility and the

influence of co-flow. First, flexibility is known to improve the efficiency of flapping propulsors. Although the snap-buckling plate showed an improved performance when compared with a rigid flat plate, a comparison to a flexible flat plate would provide insights into whether the increased design complexity of a snap-buckling plate provides a sufficient increase in thrust and efficiency. Second, the curved geometry is shown to 'channel' the flow in the thrust direction from 2D DPIV and dye visualization studies. The influence of co-flow would likely hamper this behavior, so understanding its influence would provide insights into the range of Reynolds numbers where curved designs would be applicable. Third, considering the highly three-dimensional nature of the flow, a quantitative 3D flow visualization technique would provide more insight into the underlying mechanisms utilized by the curved geometries. Finally, planform area was shown to significantly impact the generated thrust and efficiency. A more rigorous investigation of the planform area can be conducted and an actuated fin developed that could modify the overall planform area at-will to take advantage of planform area effects.

The third study involved the optimization of a trajectory in three-dimensional space for a flapping fin propulsor. The generated trajectories were inspired by the motion of a bird's wings and a fish's pectoral and caudal fins. The trajectory was parameterized by 10 variables, executed by a SPM, and optimized using the CMA-ES. The optimal trajectory was qualitatively defined as that which met the desired force set-point with the greatest efficiency. This definition was motivated by potential applications for vehicle control where a certain force is desired to travel at a specific velocity. The effectiveness and potential of experimentally finding optimal trajectories was demonstrated through a few optimization searches. The first two searches involved finding an optimal trajectory for generating a side-force, similar to how the pectoral fins of a fish are used. One search was allowed to investigate an arbitrary trajectory in three-dimensional space while the other was constrained to only investigate trajectories that moved in a line. The third case involved finding an optimal trajectory for generating thrust, similar to how the caudal fin of a fish is used. Within all three searches, the optimization found multiple trajectories within the first few generations that matched the desired force set-point. Many of the generations afterwards were spent modifying the efficiency. The first case, where the trajectory was allowed to be arbitrary in three-dimensional space to optimize side-force, converged to a wide ellipse in which most of the useful force was generated during one half of the cycle. The second case, where the trajectory was constrained to a line to optimize side-force, converged to a trajectory that predominately generated a consistently positive

useful force throughout the cycle. The third case to optimize thrust was primarily used as a sensitivity study and as a basis to compare vortex-based propulsion to the mechanisms of the first two searches. The results suggested that small changes to the fitness function would not significantly change the overall trajectory and that vortex-based propulsion is not as efficient as generating force in the manner used by the other two test cases. This is a reasonable result because vortex-based propulsion typically sees its greatest efficiency at higher Reynolds numbers. The speed at which the optimization converges, despite the inherit complexities of the flow physics and the parameter interactions, shows promise for future applications. By developing a library of optimal trajectories for different applications and flow regimes, and by understanding how small modifications to these trajectories will impact the resulting forces and efficiencies, a solid foundation for vehicle control will be obtained.

The potential of the third study is vast, with opportunities to study and expand the parameter space exponentially. Due to the speed at which the optimization converges, new parameters can be added such as fin flexibility, axis of rotation, co-flow, working fluid, etc... Furthermore, investigation and comparison of the obtained optimal trajectories using a quantitative three-dimensional flow visualization technique would provide an explanation for the performance of the optimal trajectories. Finally, the flexibility in the user-defined fitness function allows for tailoring of the obtained optimal value based upon the desired application.

Three studies regarding flapping propulsion have been conducted, each which have produced interesting results and many follow up questions. Hopefully these contributions have provided additional insights into the mechanics involved in flapping propulsion and evidence for many potential future applications.

BIBLIOGRAPHY

[1] L. L. Whitcomb. Underwater robotics: Out of the research laboratory and into the field. In *Robotics and Automation, 2000. Proceedings. ICRA'00. IEEE International Conference on*, volume 1, pages 709–716. IEEE, 2000.

[2] W. Kohnen. 2007 mts overview of manned underwater vehicle activity. *Mar. Technol. Soc. J.*, 42(1):26–37, 2008.

[3] J. W. Nicholson and A. J. Healey. The present state of autonomous underwater vehicle (auv) applications and technologies. *Mar. Technol. Soc. J.*, 42(1): 44–51, 2008.

[4] J. Yuh. Design and control of autonomous underwater robots: A survey. *Auton. Robot*, 8(1):7–24, 2000.

[5] J. L. Wham, L. A. Mackey, and F. R. Haselton. Propeller system with electronically controlled cyclic and collective blade pitch, March 10 1987. US Patent 4,648,345.

[6] P. Niyomka, N. Bose, J. Binns, and H. Nguyen. Experimental characterization of collective and cyclic pitch propulsion for underwater vehicle. In *The 3rd International Symposium on Marine Propulsors, Launceston, Tasmania*, 2013.

[7] H. D. Nguyen, P. Niyomka, J. R. Binns, N. Bose, and K. D. Le. Omnidirectional control of an underwater vehicle equipped with a collective and cyclic pitch propeller. In *The Second Vietnam Conference on Control and Automation*, pages 771–780, 2013.

[8] D. T. Roper, S. Sharma, R. Sutton, and P. Culverhouse. A review of developments towards biologically inspired propulsion systems for autonomous underwater vehicles. *P. I. Mech. Eng. M.-J. Eng.*, 225(2):77–96, 2011.

[9] F. E. Fish. Limits of nature and advances of technology: What does biomimetics have to offer to aquatic robots? *Appl. Bionics Biomech.*, 3(1):49–60, 2006.

[10] J. S. Palmisano, J. Geder, M. Pruessner, and R. Ramamurti. Power and thrust comparison of bio-mimetic pectoral fins with traditional propeller-based thrusters. In *18th International Symposium on Unmanned Untethered Submersible Technology*, 2013.

[11] M. Sfakiotakis, D. M. Lane, and J. B. C. Davies. Review of fish swimming modes for aquatic locomotion. *IEEE J. Oceanic Eng.*, 24(2):237–252, 1999.

[12] R. Blake. Fish functional design and swimming performance. *J. Fish Biol.*, 65(5):1193–1222, 2004.

[13] D. Weihs. A hydrodynamical analysis of fish turning manoeuvres. *P. Roy. Soc. B-Biol. Sci.*, 182(1066):59–72, 1972.

[14] M. M. Koochesfahani. Vortical patterns in the wake of an oscillating airfoil. *AIAA J.*, 27(9):1200–1205, 1989.

[15] J. C. S. Lai and M. F. Platzer. Jet characteristics of a plunging airfoil. *AIAA J.*, 37(12):1529–1537, 1999.

[16] M. S. Triantafyllou, G. S. Triantafyllou, and R. Gopalkrishnan. Wake mechanics for thrust generation in oscillating foils. *Phys. Fluids A-Fluid*, 3(12): 2835–2837, 1991.

[17] T. Schnipper, A. Andersen, and T. Bohr. Vortex wakes of a flapping foil. *J. Fluid Mech.*, 633:411–423, 2009.

[18] J. H. J. Buchholz and A. J. Smits. On the evolution of the wake structure produced by a low-aspect-ratio pitching panel. *J. Fluid Mech.*, 546:433–443, 2006.

[19] J. H. J. Buchholz and A. J. Smits. The wake structure and thrust performance of a rigid low-aspect-ratio pitching panel. *J. Fluid Mech.*, 603:331–365, 2008.

[20] W. Merzkirch. *Flow visualization*. Elsevier, 2012.

[21] D. Kim and M. Gharib. Characteristics of vortex formation and thrust performance in drag-based paddling propulsion. *J. Expl. Biol.*, 214(13):2283–2291, 2011.

[22] F. Pereira and M. Gharib. Defocusing digital particle image velocimetry and the three-dimensional characterization of two-phase flows. *Meas. Sci. Technol.*, 13(5):683, 2002.

[23] H. Dai, H. Luo, P. J. S. A. Ferreira de Sousa, and J. F. Doyle. Thrust performance of a flexible low-aspect-ratio pitching plate. *Phys. Fluids*, 24(10): 101903, 2012.

[24] P. D. Yeh and A. Alexeev. Effect of aspect ratio in free-swimming plunging flexible plates. *Comput. Fluids*, 124:220–225, 2016.

[25] K. Lu, Y. H. Xie, and D. Zhang. Numerical study of large amplitude, non-sinusoidal motion and camber effects on pitching airfoil propulsion. *J. Fluid Struct.*, 36:184–194, 2013.

[26] T. Wu. Fish swimming and bird/insect flight. *Annu. Rev. Fluid Mech.*, 43: 25–58, 2011.

[27] J. Wyneken. *Sea turtle locomotion: mechanisms, behavior, and energetics*, volume 1. Boca Raton, FL: CRC Press, 1997.

[28] B. D. Clark and W. Bemis. Kinematics of swimming of penguins at the detroit zoo. *J. Zool.*, 188(3):411–428, 1979.

[29] D. D. Chin and D. Lentink. Flapping wing aerodynamics: from insects to vertebrates. *J. Expt. Biol.*, 219(7):920–932, 2016.

[30] B. W. Tobalske, D. R. Warrick, C. J. Clark, D. R. Powers, T. L. Hedrick, G. A. Hyder, and A. A. Biewener. Three-dimensional kinematics of hummingbird flight. *J. Expl. Biol.*, 210(13):2368–2382, 2007.

[31] D. E. Alexander. *Nature's flyers: birds, insects, and the biomechanics of flight*. JHU Press, 2004.

[32] M. H. Dickinson, F. Lehmann, and S. P. Sane. Wing rotation and the aerodynamic basis of insect flight. *Science*, 284(5422):1954–1960, 1999.

[33] D. Lentink and M. H. Dickinson. Rotational accelerations stabilize leading edge vortices on revolving fly wings. *J. Expt. Biol.*, 212(16):2705–2719, 2009.

[34] R. Liebe. *Flow phenomena in nature: a challenge to engineering design*, volume 1. WIT Press, 2007.

[35] T. Weis-Fogh. Quick estimates of flight fitness in hovering animals, including novel mechanisms for lift production. *J. Expl. Biol.*, 59(1):169–230, 1973.

[36] M. J. Lighthill. On the weis-fogh mechanism of lift generation. *J. Fluid Mech.*, 60(01):1–17, 1973.

[37] G. R. Spedding and T. Maxworthy. The generation of circulation and lift in a rigid two-dimensional fling. *J. Fluid Mech.*, 165:247–272, 1986.

[38] C. P. Ellington, C. Van Den Berg, A. P. Willmott, and A. L. R. Thomas. Leading-edge vortices in insect flight. *Nature*, 1996.

[39] D. Kim, F. Hussain, and M. Gharib. Vortex dynamics of clapping plates. *J. Fluid Mech.*, 714:5–23, 2013.

[40] S. P. Sane. The aerodynamics of insect flight. *J. Expl. Biol.*, 206(23):4191–4208, 2003.

[41] G. Cai, J. Dias, and L. Seneviratne. A survey of small-scale unmanned aerial vehicles: Recent advances and future development trends. *Unmanned Systems*, 2(02):175–199, 2014.

[42] D. S. Barrett, M. S. Triantafyllou, D. K. P. Yue, M. A. Grosenbaugh, and M. J. Wolfgang. Drag reduction in fish-like locomotion. *J. Fluid Mech.*, 392: 183–212, 1999.

[43] L. Cen and A. Erturk. Bio-inspired aquatic robotics by untethered piezohydroelastic actuation. *Bioinspir. Biomim.*, 8(1):016006, 2013.

[44] V. Palmre, J. J. Hubbard, M. Fleming, D. Pugal, S. Kim, K. J. Kim, and K. K. Leang. An ipmc-enabled bio-inspired bending/twisting fin for underwater applications. *Smart Mater. Struct.*, 22(1):014003, 2012.

[45] Z. Wang, G. Hang, J. Li, Y. Wang, and K. Xiao. A micro-robot fish with embedded sma wire actuated flexible biomimetic fin. *Sensor Actuat. A-Phys.*, 144(2):354–360, 2008.

[46] M. Karpelson, G. Y. Wei, and R. J. Wood. A review of actuation and power electronics options for flapping-wing robotic insects. In *Robotics and Automation, 2008. ICRA 2008. IEEE International Conference on*, pages 779–786. IEEE, 2008.

[47] C. M. Gosselin and J. Angeles. The optimum kinematic design of a spherical three-degree-of-freedom parallel manipulator. *J. Mech. Transm.-T. ASME*, 111 (2):202–207, 1989.

[48] C. M. Gosselin, J. Sefrioui, and M. J. Richard. On the direct kinematics of spherical three-degree-of-freedom parallel manipulators of general architecture. *J. Mech. Design*, 116(2):594–598, 1994.

[49] E. Cavallo. *Parallel Robotic System Design for the Sterring and Guidance Mechanism of an Autonomous Underwater Vehicle*. PhD thesis, Università di Genova, April 2003.

[50] B. Sudki, M. Lauria, and F. Noca. Marine propulsor based on a three-degree-of-freedom actuated spherical joint. In *Proceedings of the 3rd International Symposium on Marine Propulsors*, pages 481–485, 2013.

[51] S. P. Sane and M. H. Dickinson. The control of flight force by a flapping wing: lift and drag production. *J. Expt. Biol.*, 204(15):2607–2626, 2001.

[52] G. J. Berman and Z. J. Wang. Energy-minimizing kinematics in hovering insect flight. *J. Fluid Mech.*, 582:153–168, 2007.

[53] S. Thomson, C. Mattson, M. Colton, S. Harston, D. Carlson, and M. Cutler. Experiment-based optimization of flapping wing kinematics. In *47th AIAA Aerospace Sciences Meeting including The New Horizons Forum and Aerospace Exposition*, page 874, 2009.

[54] T. Rakotomamonjy, M. Ouladsine, and T. L. Moing. Modelization and kinematics optimization for a flapping-wing microair vehicle. *J. Aircraft*, 44(1): 217–231, 2007.

[55] I. H. Tuncer and M. Kaya. Optimization of flapping airfoils for maximum thrust and propulsive efficiency. *AIAA J.*, 43(11):2329–2336, 2005.

[56] E. De Margerie, J. B. Mouret, S. Doncieux, and J. A. Meyer. Artificial evolution of the morphology and kinematics in a flapping-wing mini-uav. *Bioinspir. Biomim.*, 2(4):65, 2007.

[57] T. Bäck and H. P. Schwefel. An overview of evolutionary algorithms for parameter optimization. *Evol. Comput.*, 1(1):1–23, 1993.

[58] N. Hansen and A. Ostermeier. Completely derandomized self-adaptation in evolution strategies. *Evol. Comput.*, 9(2):159–195, 2001.

[59] N. Hansen, S. D. Müller, and P. Koumoutsakos. Reducing the time complexity of the derandomized evolution strategy with covariance matrix adaptation (cma-es). *Evol. Comput.*, 11(1):1–18, 2003.

[60] N. Hansen and S. Kern. Evaluating the cma evolution strategy on multimodal test functions. In *PPSN*, volume 8, pages 282–291. Springer, 2004.

[61] N. Hansen. Benchmarking a bi-population cma-es on the bbob-2009 function testbed. In *Proceedings of the 11th Annual Conference Companion on Genetic and Evolutionary Computation Conference: Late Breaking Papers*, pages 2389–2396. ACM, 2009.

[62] J. R. Hunter and J. R. Zweifel. Swimming speed, tail beat frequency, tail beat amplitude, and size in jack mackerel, trachurus-symmetricus, and other fishes. *Fish Bull*, 69(2):253, 1971.

[63] R. Bainbridge. The speed of swimming of fish as related to size and to the frequency and amplitude of the tail beat. *J. Expl. Biol.*, 35(1):109–133, 1958.

[64] V. C. Sambilay Jr. Interrelationships between swimming speed, caudal fin aspect ratio and body length of fishes. *Fishbyte*, 8(3):16–20, 1990.

[65] S. P. Colin, J. H. Costello, and H. Kordula. Upstream foraging by medusae. *Mar. Ecol.-Prog. Ser.*, 327:143–155, 2006.

[66] S. P. Colin, J. H. Costello, K. Katija, J. Seymour, and K. Kiefer. Propulsion in cubomedusae: mechanisms and utility. *PloS One*, 8(2):e56393, 2013.

[67] A. C. Morandini, F. L. Da Silveira, and G. Jarms. The life cycle of chrysaora lactea eschscholtz, 1829 (cnidaria, scyphozoa) with notes on the scyphistoma stage of three other species. *Hydrobiologia*, 530(1-3):347–354, 2004.

[68] W. M. Graham and R. M. Kroutil. Size-based prey selectivity and dietary shifts in the jellyfish, aurelia aurita. *J. Plankton Res.*, 23(1):67–74, 2001.

[69] L.-A. Gershwin and A. G. Collins. A preliminary phylogeny of pelagiidae (cnidaria, scyphozoa), with new observations of chrysaora colorata comb. nov. *J. Nat Hist*, 36(2):127–148, 2002.

[70] C. E. Willert and M. Gharib. Digital particle image velocimetry. *Exp. Fluids*, 10(4):181–193, 1991.

[71] J. C. Wu. Theory for aerodynamic force and moment in viscous flows. *AIAA. J.*, 19(4):432–441, 1981.

[72] R. Bainbridge. Caudal fin and body movement in the propulsion of some fish. *J. Exp. Biol*, 40(1):23–56, 1963.

[73] A. Gibb, B. Jayne, and G. Lauder. Kinematics of pectoral fin locomotion in the bluegill sunfish lepomis macrochirus. *J. Exp. Biol*, 189(1):133–161, 1994.

[74] J. L. Tangorra, S. N. Davidson, I. W. Hunter, P. G. A. Madden, G. V. Lauder, H. Dong, M. Bozkurttas, and R. Mittal. The development of a biologically inspired propulsor for unmanned underwater vehicles. *IEEE J. Oceanic Eng.*, 32(3):533–550, 2007.

[75] S. F. Hoerner. *Fluid-dynamic drag: practical information on aerodynamic drag and hydrodynamic resistance*. Hoerner Fluid Dynamics Midland Park, NJ, 1965.

[76] F. Steiner. Commande d'un robot rotule à 3 degrés liberté à très haute dynamique (hardware). Master's thesis, MSE HES-SO, Lausanne, 2016.

[77] W. Steiner. Commande d'un robot rotule à 3 degrés de liberté à très haute dynamique (modélisation et contrôle). Master's thesis, MSE HES-SO, Lausanne, 2016.